CARBOHYDRATE-SILICA NANOPARTICLES FOR SIRNA DELIVERY: SYNTHESIS, CHARACTERIZATION, AND GENE DELIVERY

By

Olivia Mariel Chesniak

A DISSERTATION

Submitted to
Michigan State University
in partial fulfillment of the requirements
for the degree of

Chemistry – Doctor of Philosophy

2019

ABSTRACT

CARBOHYDRATE-SILICA NANOPARTICLES FOR SIRNA DELIVERY: SYNTHESIS, CHARACTERIZATION, AND GENE DELIVERY

By

Olivia Mariel Chesniak

RNA interference (RNAi) has long been pursued for its therapeutic potential. Sequence-specific knockdown of gene expression requires that small interfering RNA (siRNA) gain access to cellular cytoplasm, presenting difficulties for both the transport of nucleic acids to cells and their voyage across cellular membranes. Numerous materials are under development as siRNA delivery vehicles to address this need. The carbohydrate dextran has been incorporated into amine-functionalized silica nanoparticles (Dex-SiO_2-NPs), enhancing their biocompatibility and success as siRNA delivery vehicles. Inspired by the work of Stöber and others, reagent concentrations in the synthesis of Dex-SiO_2-NPs have been adjusted to tune nanoparticle diameter. The size, shape, and morphology of Dex-SiO_2-NPs have been characterized using transmission electron microscopy (TEM) and energy dispersive x-ray spectroscopy (EDS). These methods have revealed that Dex-SiO_2-NPs decrease in silicon density toward their centers, when compared with SiO_2-NPs. Thermal and porosity analysis were used to profile Dex-SiO_2-NPs both containing dextran and after its removal by calcination. Having measured an increase in mesopores and decrease in micropores with calcination, it has been concluded that dextran serves as a porogen in Dex-SiO_2-NP synthesis. Not only does dextran imbue these materials with unique morphology, it also enhances their function as delivery vehicles. Dex-SiO_2-NPs improve enhanced green fluorescent protein (EGFP) supression compared to silica nanoparticles synthesized in the absence of dextran in human lung and kidney cells *in vitro*.

“As she waits for the future
she leans into the present,
for there are truly
beautiful things to
be gathered here."
Morgan Harper Nichols

This dissertation is the culmination of many years of work as both a scientist and a person.
I am honored to have grown through it.

ACKNOWLEDGEMENTS

This work would not have been possible without the time and talents of numerous individuals. I did not spend much time with my first advisor, Dr. Gregory Baker, but will always remember him describing the microscopy images displayed outside his research laboratory as both science and art; I knew immediately that I had to work with him. Unfortunate circumstances led me to Dr. Milton R. Smith, III's research group. He graciously joined a collaboration that neither of us were very familiar with, and we learned many things about RNAi and silica together. Dr. Cristina Chan and Dr. S. Patrick Walton have provided invaluable guidance in my research and, along with Daniel Vocelle, have been skilled collaborators who have challenged me to become a truly interdisciplinary scientist. I am also grateful to Dr. Xuefei Huang and Dr. John Frost, for serving on my committee.

Many have been incredibly generous with their time and equipment. I'm incredibly grateful to Dr. T.J. Pinnavaia for his willingness to discuss my results and hypotheses with me, Dr. Xudong Fan and Dr. Alicia Withrow for microscopy training, Dr. Daniel Holmes for assistance with solid state NMR experiments, Dr. Kathy Severin for use of IR and UV-Vis instrumentation, Dr. Xuefei Huang and his research group, Dr. Thomas Hamann and his research group for use of their furnace, Dr. Gary Blanchard and his research group for use of their TGA, Dr. Michael Rich and the Composite Materials and Structures Center for training and assistance with surface area and porosity analysis, and Dr. Scott Calabrese Barton and his research group, particularly Yuanchao Liu, Alex Mirabal, and Dr. Jim Woodward, for use of their surface area and porosity analysis equipment.

The Smith research group has been a wonderful environment to learn in, and for that I thank past and present group members: Dr. Behnaz Ghaffari, Dr. Yu-Ling Lien, Dr. Kristin Shannon, Dr. Tim Shannon, Dr. Susanne Miller, Dr. Shawn Preshlock, Dr. Dmitry Shabasov, Dr. Buddhadeb Chattopadhyay, Po-Jen Hsiao, Reza Ghazfar, Mona Maleka Ashtiani, Alex O'Connell, Seokjoo Li, and Ryan Fornwald. I also want to thank Aaliyah Jeter for her excellent work and enthusiasm as a summer undergraduate researcher.

I am continually grateful for my friends who have grown with me and shared their invaluable

wisdom both personally and professionally. Dr. Georgina Comiskey, Dr. Nicole Hough, Dr. Shannon Kraemer, and Dr. Monica Carey are the fiercest women I know and have been incredibly generous with their time and talents. Many others have also made an impact on me in my time at MSU.

My family has provided immense support and made significant sacrifices throughout my education, and I can't express my appreciation enough. I'm especially grateful for my father's many phone calls and jokes, chocolate and kabanos from my grandma, care packages from my brother, sister-in-law, and nieces, and to the women of my family who inspired and encouraged me most in pursuing my education: my mother Joyce Chesniak, my sister Deanna Chesniak, and my cousin Dr. Laura Chesniak-Phipps. Lastly, I thank my husband, Dr. David Olson, for continually supporting me, believing in my ability to accomplish my goals, and for helping make Lansing, Michigan home.

TABLE OF CONTENTS

LIST OF TABLES

LIST OF FIGURES

LIST OF SCHEMES

KEY TO ABBREVIATIONS

°C Degree Celsius

α-CD alpha-Cyclodextrin

APTES 3-aminopropyl triethoxy silane

BET Brunauer, Emmet, and Teller

BJH Barrett, Joyner, and Halenda

CP-MAS Cross-polarization magic angle spinning

β-CD beta-Cyclodextrin

D_2O Deuterium dioxide

d^6-DMSO Deuterated dimethylsulfoxide

Da Dalton

Dex-SiO_2-NP Dextran containing SiO_2 nanoparticle

DFT Dynamic functional theory

DLS Dynamic light scattering

DNA Deoxyribonucleic acid

dsRNA Double stranded RNA

EDS Energy dispersive X-ray spectroscopy

eV Electron volts

FT Fourier transform

g Gram

EGFP Enhanced green fluorescent protein

h Hour

IR Infrared

L Liter

LF2K Lipofectamine 2000

Hz Hertz

mol Mole

MWCO Molecular weight cutoff

NMR Nuclear magnetic resonance

NP Nanoparticle

psi Pounds per square inch

$\mathbf{R_H}$ Hydrodynamic radius

RNA Ribonucleic acid

RNAi RNA interference

RISC RNA-induced silencing complex

rt Room temperature

S-TEM Scanning transmission electron microscopy

siRNA Small interfering RNA

TEM Transmission electron microscopy

TEOS Tetraethyl ortho silicate

TGA Thermogravimetric analysis

UV-Vis Ultraviolet visible

CHAPTER 1

INTRODUCTION

1.1 RNA Interference and the Delivery Debacle

RNA interference (RNAi) is an endogenous pathway of gene suppression which can be exogenously activated, giving rise to immense therapeutic potential. Fire and Mello first described RNAi in *C. elegans* in 1998.[1] Soon after, Elbashir and co-workers established siRNA-mediated gene silencing in mammalian cells.[2] Small interfering RNA (siRNA) are 21-23 nucleotides long and initiate RNAi upon detection by proteins within the cellular cytoplasm. An assembly of proteins known as the RNA-induced silencing complex (RISC) is activated by binding the guide strand of siRNA. mRNA containing a sequence complimentary to the siRNA are targeted by RISC, which are then degraded by the Argonaute RNase, leading to suppression of the target protein (Figure 1.1).[3] In this way, an RNAi therapeutic addresses the origin of a protein-based disease.

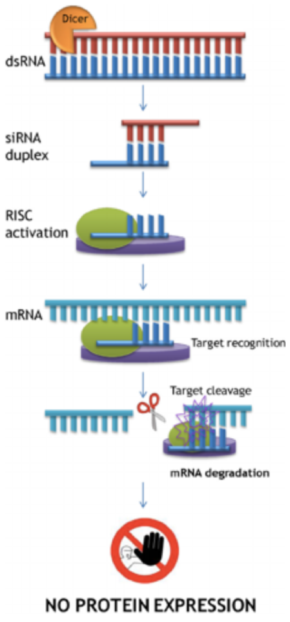

Figure 1.1: *Diagram of RNA interference Process.* Image ©2017 Elsevier[3]

Nevertheless, the potential to exogenously activate RNAi using a tailored sequence of siRNA brings with it several challenges. Nucleases in the blood can degrade siRNA, leading to low *in vivo* half lives and poor drug performance. Additionally, the negative charge of siRNA limit their ability to traverse cell membranes. These challenges have been addressed through the use of delivery vehicles, which protect siRNA and assist in delivering it into cellular cytoplasm.[4–6]

When designing vehicles for siRNA delivery, size, surface functionalization, and mode of siRNA binding are at the forefront of design considerations. Size and shape of nanoparticles (NPs) play a role in determining their recognition by phagocytes and trafficking through endocytotic pathways. NP surface functionality also plays a role in determining the toxicity of the delivery vehicle, phagocytic recognition, and provides a convenient platform upon which to include moieties to target specific tissues or cells. Further, the presence of different components on NP surfaces will in turn impact surface charge, which plays a role in the complex's biodistribution and ability to cross cellular membranes. The binding and protection of siRNA can be accomplished via surface attachment (electrostatic or covalent) or encapsulation within hollow NP pores or centers.[7] Each of these design considerations may be applied to different types of non-viral delivery vehicles, whether polymeric, lipid-based, or solid. While lipid-based delivery vehicles can cross the membrane, others gain access to the cellular cytoplasm via endocytosis. While the majority of clinical trials in RNAi therapeutics have employed naked siRNA, lipid nanoparticles follow by only 10% (Figure 1.2). Polymer delivery vehicles and N-galactosamine (GalNAc)-siRNA conjugates have also been investigated, each was represented in 6.6% of clinical trials as of 2016.[8]

The first drug candidate using RNAi recently obtained FDA approval to treat a hereditary peripheral nerve disease, hereditary transthyretin-mediated amyloidosis (hATTR). Resulting from build up of amyloid protein fibers in organs and tissues, treatment of hATTR by RNAi reduces the production of the proteins which cause the disease. Onpattro (patisiran), developed by Alnylam Pharmaceuticals, Inc., is a lipid nanoparticle which encapsulates siRNA and is intravenously administered directly to the liver.[9] Though the first of its kind, it will likely not be the last. There are currently 16 active clinical trials for siRNA-based drugs.[10]

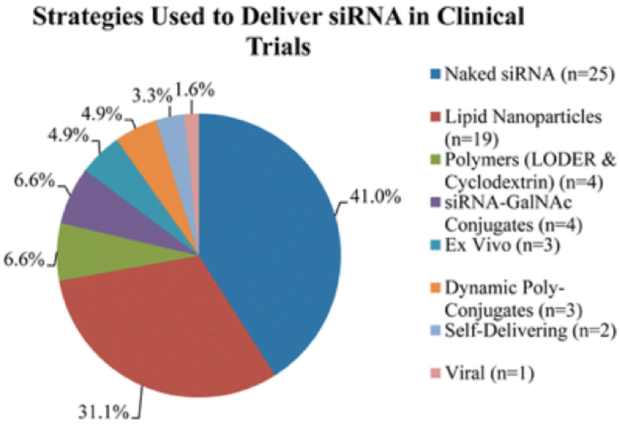

Figure 1.2: *Types of siRNA Delivery Vehicles in Clinical Trials.* Image ©2016 American Chemical Society[8]

The breadth of siRNA delivery vehicles offers incredible opportunity, but also many questions regarding the role of delivery vehicle characteristics within the RNAi pathway. This work extends the understanding of the role of dextran in siRNA delivery vehicles by investigating its role in silica nanoparticle synthesis.[11,12] By extension, dextran's location within delivery vehicles and its interaction with biological environments may be further understood. Controlling size, shape, and surface functionalization using silica nanoparticles, Comiskey found that dextran-infused silica delivery vehicles elicited greater silencing of EGFP than non-dextran containing silica.[11]

1.2 Silica Nanoparticle Synthesis

Precise size control and straightforward one-pot conditions contribute to the widespread use of sol-gel techniques for the synthesis of silica nanoparticles. Aqueous acid- or base-catalyzed hydrolysis and condensation of alkoxysilanes produce monodispersed nanoparticles of specific diameters.[13–16] These methods were first reported by Kolbe and further developed by Stöber, Fink, and Bohn in 1968, with the synthesis of uniform silica particles ranging from 0.2 to 2.0 μm in diameter (Figure 1.3).[17,18] The cornerstone of the so-called Stöber method is the ease with which nanoparticle diameters are controlled via ammonium hydroxide concentration. Silica nanoparticles ranging in size from 10 nm to 800 nm have been prepared using this method.[19]

Silica is formed via hydrolysis of an alkoxy silicate precursor, often tetraethyl orthosilicate

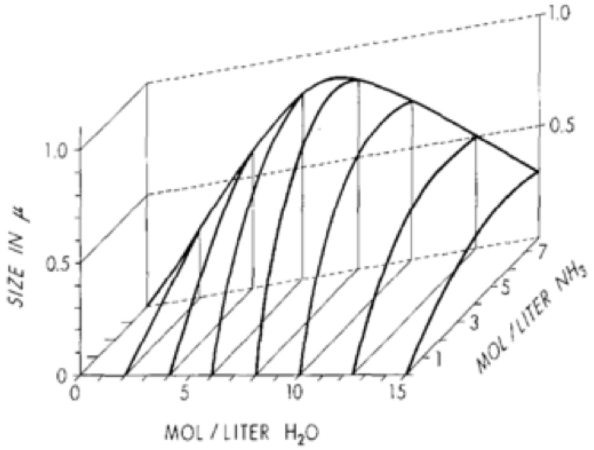

Fig. 1. Final particle sizes as obtained by reacting 0.28 mole/liter of tetraethyl silicate with various concentrations of water and ammonia in ethanol.

Figure 1.3: *Average Diameters of SiO_2-NPs upon Variation of Reagents*. Image ©1968 Elsevier[18]

(TEOS), to form a silanol and subsequent condensation of silanols to form a network of siloxanes (Scheme 1.1). Under basic conditions, the alkoxy silicate undergoes nucleophilic attack by a hydroxide ion in an S_N2 fashion to produce a silanol and an ethoxide anion. Silanol proton abstraction by hydroxide forms a siloxide ion and water in the first condensation step. Attack of the siloxide ion on the silicon atom of a neighboring silanol results in siloxane formation. Loss of hydroxide by the silanol regenerates the hydroxide catalyst.[13,20,21] Continued hydrolysis and condensation extend the siloxane network to form nanoparticles.

The hydrolysis rate increases with ammonium hydroxide concentration, as hydroxide ions are better nucleophiles than water. The rate of condensation is greater than that of hydrolysis, as silanol groups are more easily deprotonated than water, making silicon atoms of silanols more positively charged and poised for nucleophilic attack. Silanol molecules therefore prefer to condense onto larger siloxane aggregates as opposed to smaller aggregates or dimerization with other silanol molecules.[20,22,23]

Nanoparticle growth has been widely studied. Stöber silica was initially thought to proceed via the LaMer model for nanoparticle growth, which hypothesizes that an initial nucleation burst

Scheme 1.1: *Hydrolysis and Condensation of Alkyl Silicates to form* SiO_2*.*

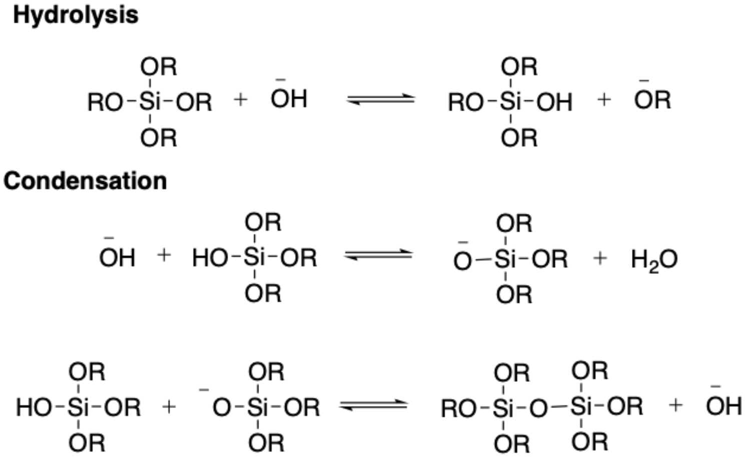

Scheme 1.2: *Schematic Depiction of LaMer Monomer Addition Process for Nanoparticle Growth.*

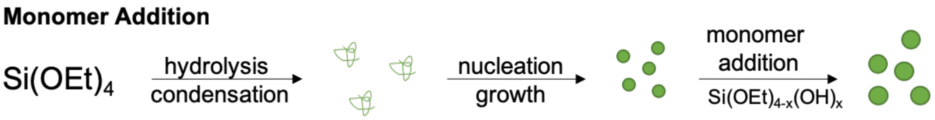

is followed by growth via monomer addition to aggregates (Scheme 1.2).[24] This model is useful for describing formation of silica nanoparticles at high concentrations of ammonium hydroxide.[25] Bogush and Zukoski later reported that the concentration of hydrolyzed TEOS is greater than what is required for nucleation until late in the reaction, suggesting that nanoparticle growth arises from aggregation of siloxane networks (Scheme 1.3).[26] In this model, nanoparticle size and polydispersity would be governed by size-dependent aggregation rates governed by the colloidal stability of particles. This model also accounts for the polydispersity often observed in Stöber silica populations, if large particles were to aggregate with other large particles instead of with smaller particles. Building on the experimental results of Bogush and Zukoski, Lee constructed an aggregation-based kinetic model which accurately represents diameters of Stöber silica nanoparticles at low ammonia concentrations.[25]

Han and co-workers studied the direct impacts of TEOS hydrolysis and condensation kinetics

Scheme 1.3: *Schematic Depiction of Aggregation and Growth Process for Nanoparticle Synthesis.*

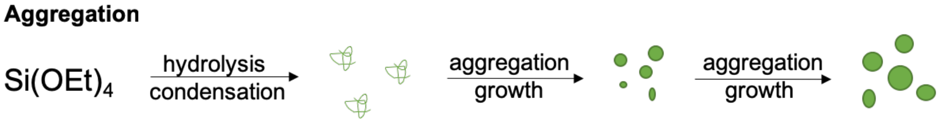

Scheme 1.4: *Schematic Depiction of Seeded Growth Process for Nanoparticle Synthesis.*

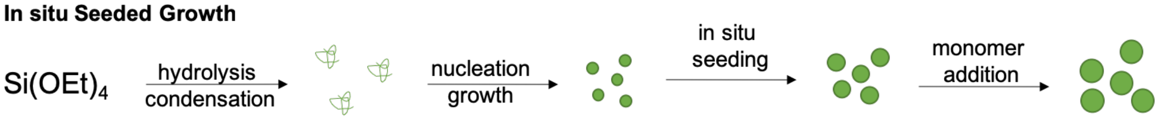

on nanoparticle size over time, reconciling the relationship between nucleation and aggregation in silica nanoparticle synthesis. They concluded that two pathways exist: TEOS hydrolysis dominates the first pathway, involving nucleation and early stages of silanol growth into small aggregates. The second pathway is comprised of silanol condensation onto aggregates formed in the first pathway (Scheme 1.4).[20] This in situ seeded growth process builds on both the LaMer and Bogush models and provides a more thorough understanding, leading to improvements in silica nanoparticle synthesis by way of smaller diameters and narrower distributions.

1.3 Porogens and Templates in Silica Nanoparticle Synthesis

Functionalized silica nanoparticles have been shown to be successful drug and gene delivery vehicles which exhibit low cytotoxicity.[27–37] In this work, the carbohydrate dextran has been incorporated into the Stöber Method to enhance the biocompatibility of the resulting silica nanomaterials. Dextrans are polysaccharides having a linear backbone made up of α(1-6) linked d-glucopyranosyl units and shorter d-glucose side chains linked in an α(1-2), α(1-3), or α(1-4) manner.[38] In a therapeutic setting, dextrans are used as anticoagulants, whereas cross-linked dextran particles are used in biochemical research settings for size exclusion chromatography.[39] Dextran and other polysaccharides have been used for delivery and enhancing biocompatibility of drugs and other materials both independently and via nanoparticle incorporation (Figure 1.4).[40–48]

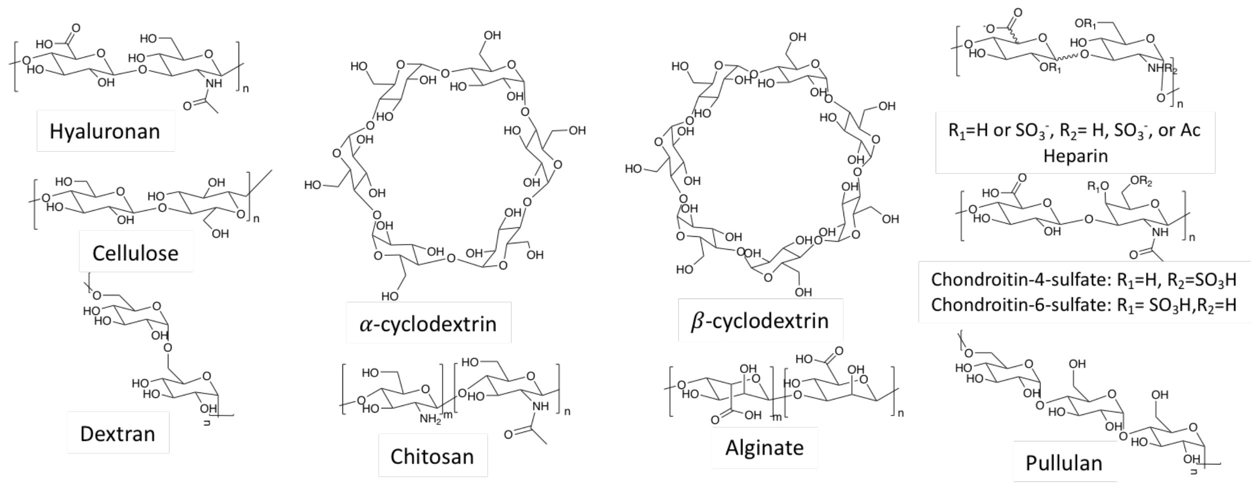

Figure 1.4: *Carbohydrates Used in Biocompatible Materials.*

Carbohydrates including some of those included in Figure 1.4 have previously been incorporated into silica nanostructures.[49–53] Lin and Sinha have both incorporated dextran onto the surface of mesoporous silica nanoparticles as gates, preventing payload release until certain biological conditions were met.[54,55] The hydrophilic/hydrophobic nature of cyclodextrins make them excellent for guest-host systems has been used to protect drugs within mesopores of silica nanoparticles.[56,57] Mansfiled and co-workers condensed a thiol-alkoxysilane in the presence of hydroxyethylcellulose, resulting in amorphous nanoparticles ranging from 50 - 500 nm.[58] The surface of silica nanoparticles were functionalized with chitosan and hyaluronic acid by Salis and co-workers, exhibiting high proliferation into cells and low cytotoxicity.[59] Silvestri and co-workers condensed tetrapropyl orthosilicate with heparin, resulting in hollow nanoparticles less than 100 nm in diameter.[60]

Surfactants including cetyltrimethylammonium bromide (CTAB) are used to template pores in Stöber silica nanoparticles. The amphiphilic nature of the surfactant directs the hydrolysis and condensation of an alkoxy silicate around surfactant assemblies, resulting in formation of pores having precise size and shape according to the surfactant used (Scheme 1.5).[13,61–64] Aside from carbohydrates and surfactants, polymers and polymer-based nanoparticles have been incorporated into silica structures.[65] Organic materials have been used both as templates for silica nanoparticle synthesis and as surface coatings. Polyamines and polylysine have been widely studied, as

Scheme 1.5: *Schematic Depiction of Nanoparticle Synthesis with Organic Template*.

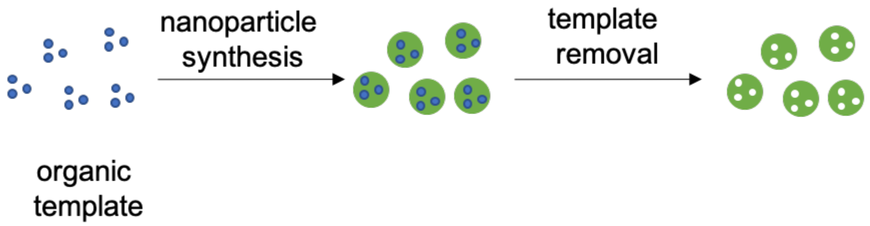

their cationic character can electrostatically direct TEOS hydrolysis and condensation and enables electrostatic binding of nucleic acids.[66–68]

As depicted in Scheme 1.5, porogens used in silica or ceramic synthesis are often removed before materials are used. Organic porogens may be washed or rinsed out of the structures using solvents or by thermal degradation under oxidative conditions. Ruckdeschel templated silica onto polystyrene nanoparticles, producing hollow silica nanoparticles with uniform thickness and dispersity after calcination.[69] However, porogens may impart unique properties to materials and are therefore not removed. This is the case for the first generation of Dex-SiO_2-NPs synthesized by Comiskey, the second generation of which are described herein.[11,12] Dex-SiO_2-NPs exhibit a hollow core, which has been observed in silica nanoparticles synthesized using polymers and aggregates as porogens.[70–73] While studies in the literature suggest the location of dextran within Dex-SiO_2-NPs, thorough characterization of these materials has been pursued with the ultimate goal of elucidating the role dextran plays in silica nanoparticle synthesis.

1.4 Characterization of Silica Nanoparticles

Silica nanoparticle characterization involves bridging methods from both chemistry and materials science. In this work, Dex-SiO_2-NPs are characterized using an array of well-established techniques.

Since Nuclear Magnetic Resonance (NMR) analysis of colloidal solutions is complicated due to their inherent lack of solubility, solid state NMR has become a prevalent analysis method for

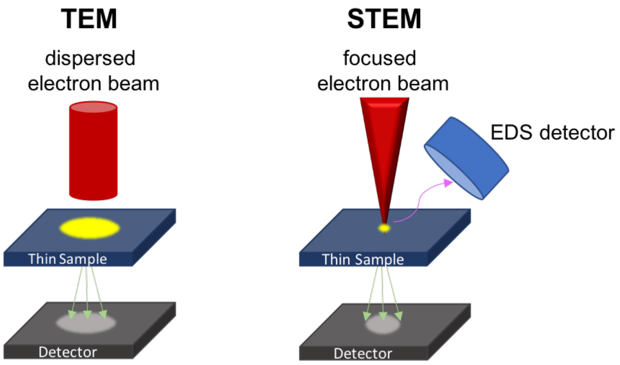

Figure 1.5: *Schematic Diagram of TEM and SEM*. Adapted from reference 77.

silica nanoparticles.[74] ^{13}C cross-polarization magic angle spinning (CP-MAS) minimizes line broadening often observed in solid state NMR by rapidly spinning the sample at 54.74 °relative to the magnetic field. In doing so, anisotropic interactions between nuclei which are typically averaged by Brownian motion in solution NMR can be averaged to zero. Cross-polarization is applied to enhance the signal from less abundant nuclei, including ^{13}C.[75,76]

Electron microscopy (EM) provides visual details of nano-scale materials and are widely used in characterization of silica nanoparticles and other materials. EM uses an accelerated electron beam which interacts with a sample, resulting in emission of electrons, x-rays, and photons. The contrast observed in EM originates from the different electron densities of elements comprising the material under analysis.[78–81] Depending on the arrangement of the sample relative to various lenses and the power of the beam, different details are apparent. A thick sample will scatter electrons rather than transmit them through the sample. With detectors situated above the sample, these scattered electrons are collected and provide details of surface morphology characteristic of scanning electron microscopy (SEM). A thinner sample, different lens placement, and detector on the opposite side of the sample relative the beam collects transmitted electrons in transmission electron microscopy (TEM) (Figure 1.5). Scanning Transmission Electron Microscopy (S-TEM) brings with it the opportunity to use x-ray Energy Dispersive Spectroscopy (EDS) to study the elemental profile of a defined sample area. S-TEM utilizes a convergent electron beam to scan the user-defined sample area. Upon being scanned by a convergent electron beam, the elements

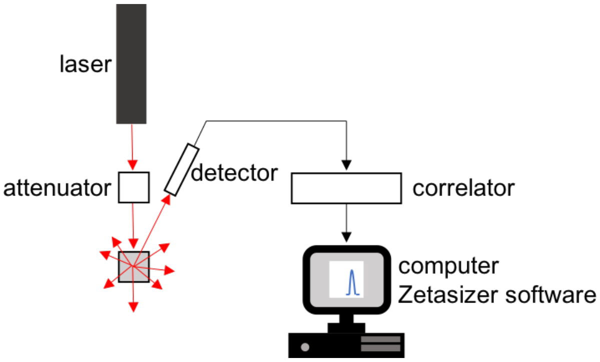

Figure 1.6: *Schematic Diagram of Light Scattering by DLS*. Adapted from reference 85.

within the sample emit characteristic x-rays which are analyzed by an electron detector. Analytical software uses this data to construct a spectra of elements present in the sample.[78, 82–84] The size, morphology, and elemental details obtained using electron microscopy provide significant insight to the quality and characteristics of materials.

Dynamic light scattering (DLS) uses the speed of particles diffusing according to Brownian motion to determine hydrodynamic size. The rate at which the intensity of scattered light fluctuates is measured. These rates are dependent on the size of particles, with larger particles taking longer to diffuse than smaller particles.[85, 86] The Zetasizer NanoZS uses a backscatter detector to measure the scattering by particles interacting with the laser (Figure 1.6). The backscatter angle near 180°decreases the effects of multiple scattering and larger dust contaminants, which are more likely to scatter forward. Since the incident beam does not travel through the entire sample cell and has a smaller path length, the concentration of sample measured increases while decreasing the collection of light scattered by a particle by other particles. The scattering intensity collected by the detector is interpreted by the correlator, which compares changes to the scattering pattern over time in order to derive the rate of change. Since the movement of particles follows Brownian motion, the Zetasizer software uses the Stokes-Einstein equation to calculate the particle size based on these data.[85, 86]

The electrophoretic mobility and velocity of nanoparticles, measured via laser doppler velocimetry (LDV) while an electric field is applied to the suspension, are used to determine the

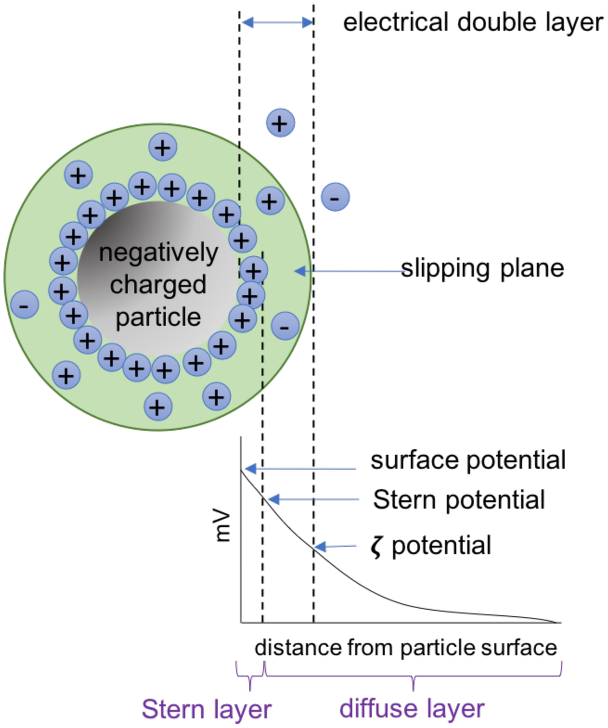

Figure 1.7: *Schematic Diagram Describing Zeta Potential*. Adapted from reference 85.

stability of particles in a suspension. Using the Henry equation, these measurements are used to calculate the ζ potential.[85–87] As depicted in Figure 1.7, a particle existing in a solution bears a net surface charge, increasing the concentration of counter ions near the surface. These strongly bound counter ions make up the Stern layer, while the outer regions are part of the diffuse layer. As a particle moves in solution, ions within the slipping plane travel with it while those beyond this region do not. The potential at the slipping plane is the ζ potential. Thus, ζ potential represents the stability of particles in a suspension: if the magnitude of ζ potential is large, particles will repel each other and remain well-dispersed, while a low-magnitude ζ potential suggests that there are not enough ions in the slipping plane to prevent particle aggregation.[85,86] As one may expect due to the importance of ions in these measurements, ζ potential is pH-dependent.

DLS and ζ potential measurements have been widely used in biomedical research.[88] Branda and co-workers used DLS and ζ potential measurements to study the impact of growth media and incubation conditions on Stöber silica nanoparticles. A decrease in hydrodynamic diameter and a

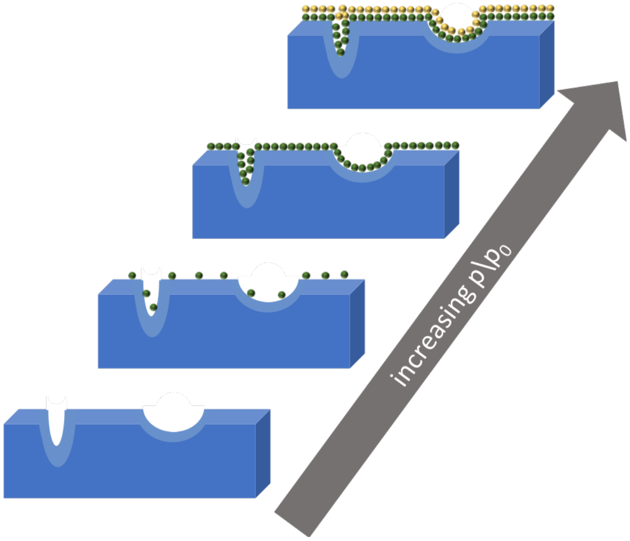

Figure 1.8: *Schematic Diagram of Gas Adsorption on a Porous Surface*.

decrease in ζ potential were observed after prolonged incubation, suggesting that aggregation of biomolecules decrease the aggregation of nanoparticles with each other. The DLS results were consistent with observations made in electron microscopy.[89]

Gas adsorption for surface area and porosity determination is an important and established part of characterizing porous solids. Inert gas, often nitrogen at 77 K, is dosed into a sample of porous solid to equilibrium, at which point the volume of gas is noted, and the dosing proceeds. These data are represented in an adsorption-desorption isotherm, the shapes of which are indicative of the porous nature of the analyzed materials (Figure 1.9).[90, 91]

Microporous materials exhibit type I isotherms, with concave shapes relative to the x-axis and plateaus at low relative pressure (p/p^0). Micropores are less than 2 nm in diameter, Type I(a) isotherms indicate the presence of micropores < 1 nm, while type I(b) indicates a broader pore size distribution containing either larger micropores (< 2 nm) or a combination of large and small micropores.[91] Type II isotherms are characteristic of macroporous and non-porous materials, with the gradual increase in volume adsorbed representing adsorption which is less restricted by pore size. Point B represents the relative pressure at which monolayer coverage is complete. A less distinctive point B, or no point B as seen in Type III, suggests that multilayer and monolayer

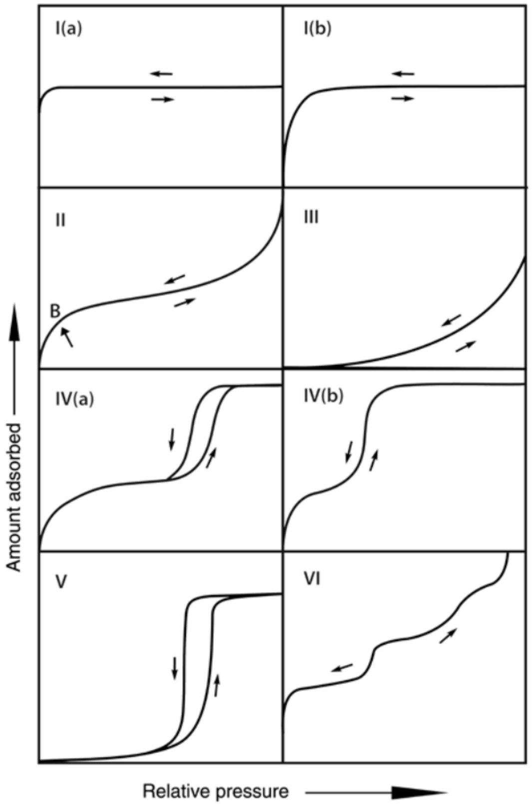

Figure 1.9: *Physisorption Isotherm Classifications Recommended by IUPAC*. Image ©2015 IUPAC & De Gruyter[91]

coverage are indistinguishable. Mesoporous (2 - 50 nm) materials have Type IV isotherms, with IV(a) depicting hysteresis arising from capillary condensation and IV(b) being reversible. While the low p/p^0 regions of Type IV isotherms resemble that of Type II isotherms, the larger size of mesopores result in condensation within pores. The eventual plateau represents saturation. Type V isotherms resemble Type III at low p/p^0, attributed to weak interactions between the adsorbent and adsorbate, often occurring in hydrophobic adsorbents having micro- and macropores. Type VI isotherms are characteristically stepwise, representing continuous adsorption on uniform, non-porous materials.[90, 91]

As indicated above, some isotherms are reversible while, for others, the desorption branch follows a different path than the adsorption branch. The different shapes of these variations, known as hysteresis, provide further information on pore structures (Figure 1.10). Type H1 is

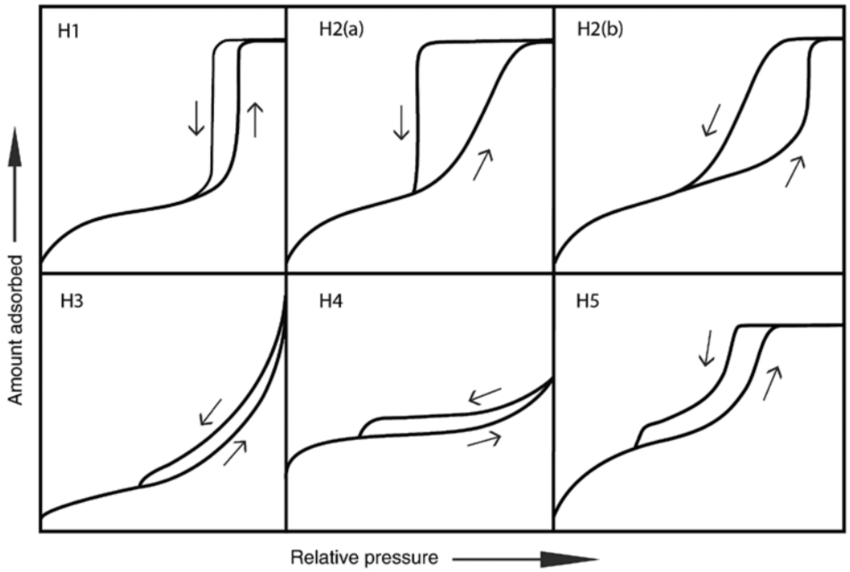

Figure 1.10: *Classification of Hysteresis Loops Observed in Physisorption Isotherms Recommended by IUPAC*. Image ©2015 IUPAC & De Gruyter[91]

common in materials having uniform mesopores and ink-bottle-shaped pores, with the hysteresis representing delayed condensation during adsorption. H2 hysteresis loops are characteristic of complex networks of pores where percolation and pore blocking may occur. Type H3 and H4 loops are somewhat similar, with the former resembling the early part of Type II isotherms. This loop is common among malleable plate-like particles and materials having macropores. Type H4 shares characteristics with Type I and Type II isotherms, and are present in materials containing micro- and mesopores. Hysteresis loops of Type H5 are less common, and distinctive of structures having mesopores that are both open and blocked.[91]

Adsorption data obtained between p/p^0 0.05 - 0.3 are used in the Brunauer-Emmet-Teller method (BET) to determine surface area. This region of the isotherm is typically linear, and application of the BET equation to this region provides an indication of the surface area of a sample. The linear form of the BET equation,

$$\frac{p/p^0}{n(1-p/p^0)} = \frac{1}{n_m * C} + \frac{C-1}{n_m * C} * (p/p^0) \tag{1.1}$$

is applied, where n is the specific volume adsorbed at relative pressure p/ptextsuperscript0, and

n_m is the specific monolayer capacity. The term C, related to the energy of monolayer adsorption, provides an indication of the isotherm shape. The specific surface area a_s is calculated using

$$a_s = \frac{n_m * L * \sigma_m}{m} \tag{1.2}$$

where σ_m is the average molecular cross-sectional area of the adsorbate molecule (0.162 nm^2 for N_2 at 77 K), and m is the mass of the adsorbent.[90–95] In addition to characterization by isotherm shapes, hysteresis loops, and BET surface area determination, density functional theory (DFT) is useful in providing a more detailed view of porous structures. Since pore characteristics and their correlation with different types of isotherms are well established, the pore size distribution may be calculated by integrating the pore size distribution f(H) and theoretical isotherm ρ(P, H),

$$\int_0^\infty f(H)\rho(P,H)\,dH \tag{1.3}$$

known as the integrated adsorption equation (IAE). The pore size distribution curve is calculated by fitting IAE isotherms to experimental isotherms.[96,97]

Gu and co-workers recognized the variation of surface area measurements of silica nanoparticles by nitrogen adsorption.[79,98,99] Careful attention revealed differences in specific surface area as much as 300 m^2/g depending on post-synthetic treatment. The most significant differences arise as a result of washing and thermal drying procedures. A decrease in dissolved silica was observed after successive washing with water, but not with ethanol. In fact, an increase in carbon was measured when silica nanoparticles were washed with ethanol alone. This suggests that water removes unhydrolyzed ethoxy groups remaining in the silica structure, whereas ethanol exacerbates this process by introducing more ethanol which is then esterified onto the silica surface.[79] Previous work identified that maximum surface areas and porosity measurements were obtained after heating at 300°C, with both metrics rapidly decreasing upon higher temperatures.[100] The greatest surface area measured by Gu and co-workers was when water-washed silica nanoparticles were dried under vacuum at 120°C. Low surface area (< 50 m^2/g) was measured after thermal treatment ranging from 50 - 200°C at atmospheric pressure.[98]

The contents of this work builds upon the discoveries and developments of innumerable scientists, some of which have been described here. Insights from the RNAi community have informed functionalization dextran-containing silica nanoparticles prepared via a modified Stöber method. Established chemical and physical characterization techniques have been implemented to further understand the silica structure. As previously stated, some porogens used in silica nanoparticle synthesis are removed via rinsing or calcination. Dextran, the porogen used herein, has been removed via calcination to enable characterization of Dex-SiO_2-NP structures in its absence. Thus many of the characterization methods discussed here have been applied to Dex-SiO_2-NPs both before and after calcination, with surface area and porosity analysis being the most indicative of the vacancies remaining in the silica structures in the absence of dextran. These studies have been embarked upon with the intention that these changes may provide insight to the location of dextran and, further, its role in Dex-SiO_2-NP synthesis.

CHAPTER 2

ESTABLISHING SIZE CONTROL OF DEXTRAN-SILICA NANOPARTICLES

2.1 Introduction

Comiskey synthesized amine-coated dextran-containing silica nanoparticles that were successful *in vitro* siRNA delivery vehicles.[11,12] The bimodal distribution of nanoparticles begs the question of which group of nanoparticles are active as delivery vehicles (Figure 2.1). Aside from their activity as delivery vehicles, several questions about the physical characteristics of these nanoparticles remained, including 1) the origins of and difference between large and small nanoparticles, 2) the location of dextran within nanoparticles, and 3) the reason for hollow-looking nanoparticle centers.

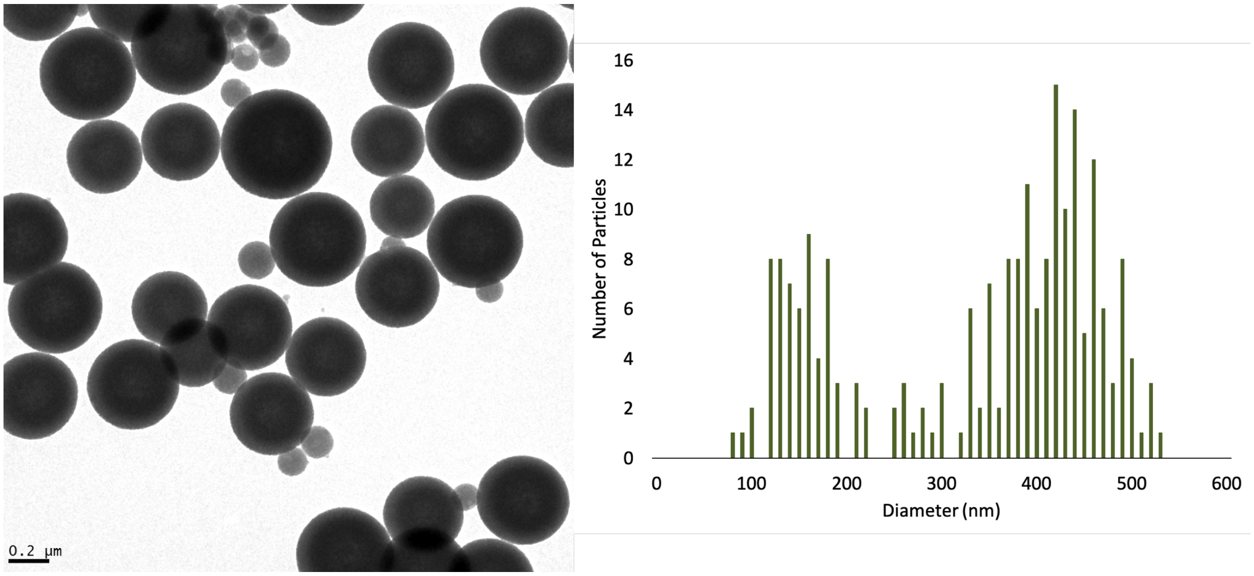

Figure 2.1: *TEM Micrograph and Size Distribution of Bimodal Amine-Coated Dex-SiO$_2$-350 Nanoparticles*. Brightness enhanced by 20% to emphasize detail, 27kx magnification, Scale bar 0.2 μm.

2.2 Synthetic Optimization of Dex-SiO_2-NP

Interest in whether the small and large nanoparticles function differently as delivery vehicles led us to first pursue separation of the two different Dex-SiO_2-NP size populations such that the silencing of each population could be evaluated independent of the other. Others have separated nanomaterials using density gradient centrifugation.[101, 102] Comiskey explored density gradient centrifugation as a method for separating the differently sized Dex-SiO_2-NPs, though all fractions contained bimodal nanoparticle distributions.[?] Size exclusion filtration was therefore pursued as a means of separating Dex-SiO_2-NPs.

Though NP density varies within the large and small Dex-SiO_2-NP populations, average diameter remains consistent. Size exclusion membranes were explored as a means of separating the 100 nm Dex-SiO_2-NPs from the 350 nm Dex-SiO_2-NPs. All Dex-SiO_2-NPs are separated from the reaction mixture using a 30kDa MWCO regenerated cellulose membrane in a pressure filtration unit (Figure 2.2). Following the initial concentration of the reaction suspension, the product is rinsed three times with approximately 200 mL of MilliQ water. This method is problematic in several ways, mainly in that the 30kDa MWCO is too small to allow 100 nm particles to pass through, as a 30kDa protein would have a diameter of approximately 5 nm. Additionally, the nanoparticles build up on the membrane, making it such that even if the pore size of the membrane would allow the particles through, the aggregation at the membrane surface may prevent effective filtration. The use of 0.2 μm ultrafiltration membranes is a promising means of separating the 100 and 350 nm nanoparticles within our most effective delivery vehicle. However, a 10x size difference is necessary for effective separation of materials with these types of membranes. Therefore it is very possible that this method of separation will not be effective for our nanoparticles. Low pressure filtration was attempted with low-concentration (1 or 0.1 mg/mL) nanoparticle suspensions, collecting the filtrate and rinsing the filter with MilliQ water. A variety of filter membranes have been used to this point: polycarbonate, polyvinylidene fluoride (PVDF), nylon, and cellulose acetate. Polycarbonate, cellulose, PVDF, and nylon membranes, all with pore sizes of 0.2 μm, were used within a pressure filtration reservoir. While the polycarbonate membrane's pores are laser-etched and therefore more

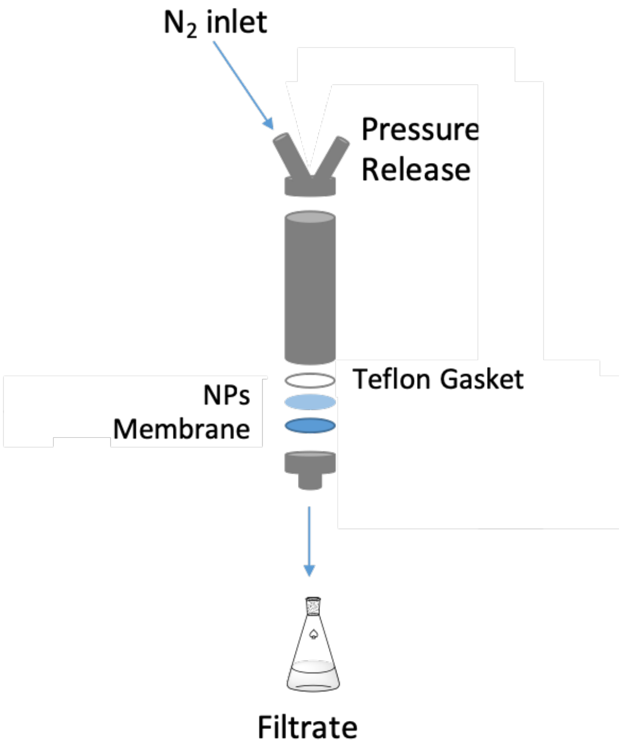

Figure 2.2: *Diagram of Pressure Filtration Apparatus.*

accurately 0.2 μm in size, the pores of the cellulose, PVDF, and nylon membranes are formed by a polymer web, resulting in more variation in the actual pore size (Figure 2.3). At all concentrations attempted, both the filtrate and the retentate contained large and small nanoparticles. Therefore, studies at lower concentrations were not pursued for the PVDF, nylon, and cellulose membranes. At 1 mg/mL, the polycarbonate membrane was likely fouling, as no particles were evident in the filtrate and both small and large particles were observed in the retentate. Decreasing to 0.1 mg/mL or 0.01 mg/mL resulted in less fouling, as hypothesized. Nevertheless, there was still a large amount of filter fouling at these low concentrations.

In order to minimize filter fouling, suspending the nanoparticles in 10% ethanol or ethanol alone in order to form a more stable suspension was studied. The process was first run on a small scale, with 10 mL aliquots of 0.1 and 0.01 mg/mL nanoparticle. While some particles were able to pass through the polycarbonate membrane when filtration was performed in 10% ethanol, filter

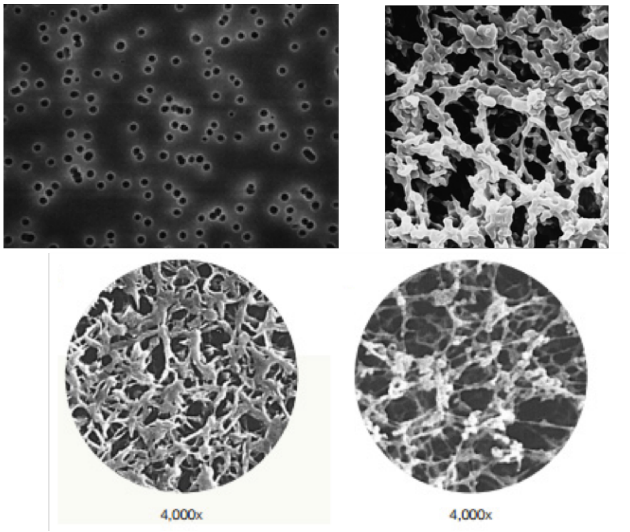

Figure 2.3: *TEM Micrographs of Size Exclusion Membranes*. Polycarbonate membrane (top left) and mixed cellulose esters membrane (top right), PVDF membrane (bottom left) and nylon membrane (bottom right), Image ©Millipore Sigma.[103]

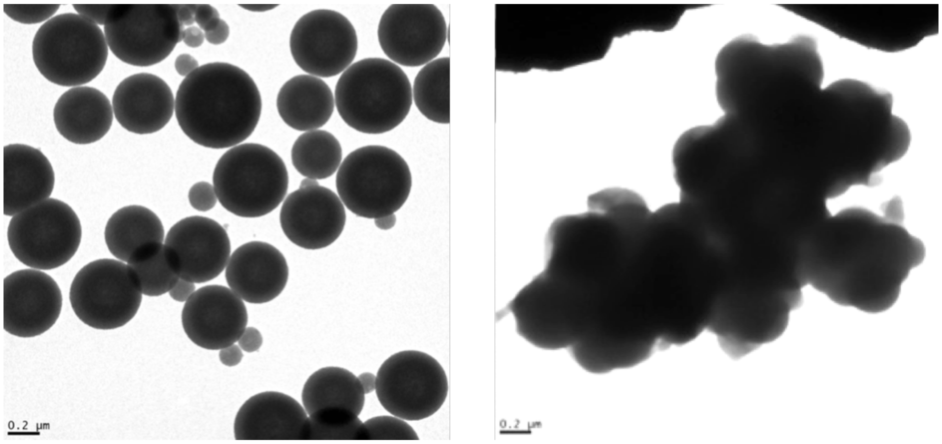

Figure 2.4: *TEM Micrographs of Dex-SiO$_2$-350 NPs Filtered Through 0.2 μm Polycarbonate Membrane*. 50 mL of 0.01 mg/mL of Dex-SiO$_2$-350 NPs suspended in 10% ethanol underwent pressure filtration using a 0.2 μm Polycarbonate Membrane, before (left) and after (right) filtration. 27kx magnification, scale bar 0.2 μm. Brightness enhanced by 20% to emphasize detail.

fouling was still a problem (Figure 2.4). Performing the filtration process in 100% ethanol was even more effective. While nanoparticles with both 100 and 200 nm diameter were observed (Figure 2.5), there was notably less aggregation than the filtration with 10% ethanol.

Despite the low concentration (0.01 mg/mL) and the stable suspension of our nanoparticles in ethanol, aggregation on the membrane is still present, evidenced by both large and small

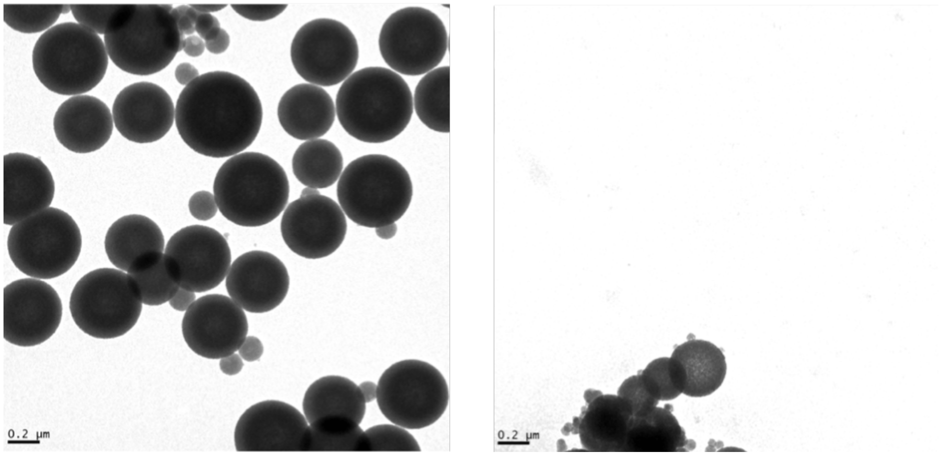

Figure 2.5: *TEM Micrographs of Dex-SiO$_2$-350 NPs Filtered Through 0.2 µm Polycarbonate Membrane*. 50 mL of 0.01 mg/mL of Dex-SiO$_2$-350 NPs suspended in 100% ethanol underwent pressure filtration using a 0.2 µm Polycarbonate Membrane, before (left) and after (right) filtration. 27kx magnification, scale bar 0.2 µm. Brightness enhanced by 20% to emphasize detail.

nanoparticles observed in the retentate sample by TEM. The original purpose of separating the large and small nanoparticles within our delivery vehicle population was to investigate whether either size is a more effective delivery vehicle than the other. Only a small amount of nanoparticle was recovered from each filtration, which is attributed to filter fouling, which withholds a significant portion of nanoparticle from the already dilute suspension. Considering its low efficiency and effectiveness, filtration was not further pursued as a separation method.

In addition to attempts to separate the 100 nm and 350 nm diameter Dex-SiO$_2$-NPs in order to obtain a monomodal size distribution, the starting materials were purified immediately before use. Other than dextran, the two primary reagents, tetraethylorthosilicate (TEOS) and 3-aminopropyl triethoxysilane (APTES) are both alkyl silicates, which readily hydrolyze in the presence of moisture. Partial or complete hydrolysis of ethoxy groups present in the reagents would leave the more active silicic acids as impurities. In the base-catalyzed hydrolysis and condensation of silicates, silicic acid would have a different reaction rate than TEOS, ultimately impacting nanoparticle size. TEOS and APTES were purified by distillation and evaluated by ^{1}H-NMR and the distributions of NPs by TEM. Despite producing bimodal Dex-SiO$_2$-NPs, any existing impurities are not evident in the ^{1}H-NMR spectrum of TEOS (Figure 2.6). Distilled TEOS produces monodisperse Dex-SiO$_2$-NPs

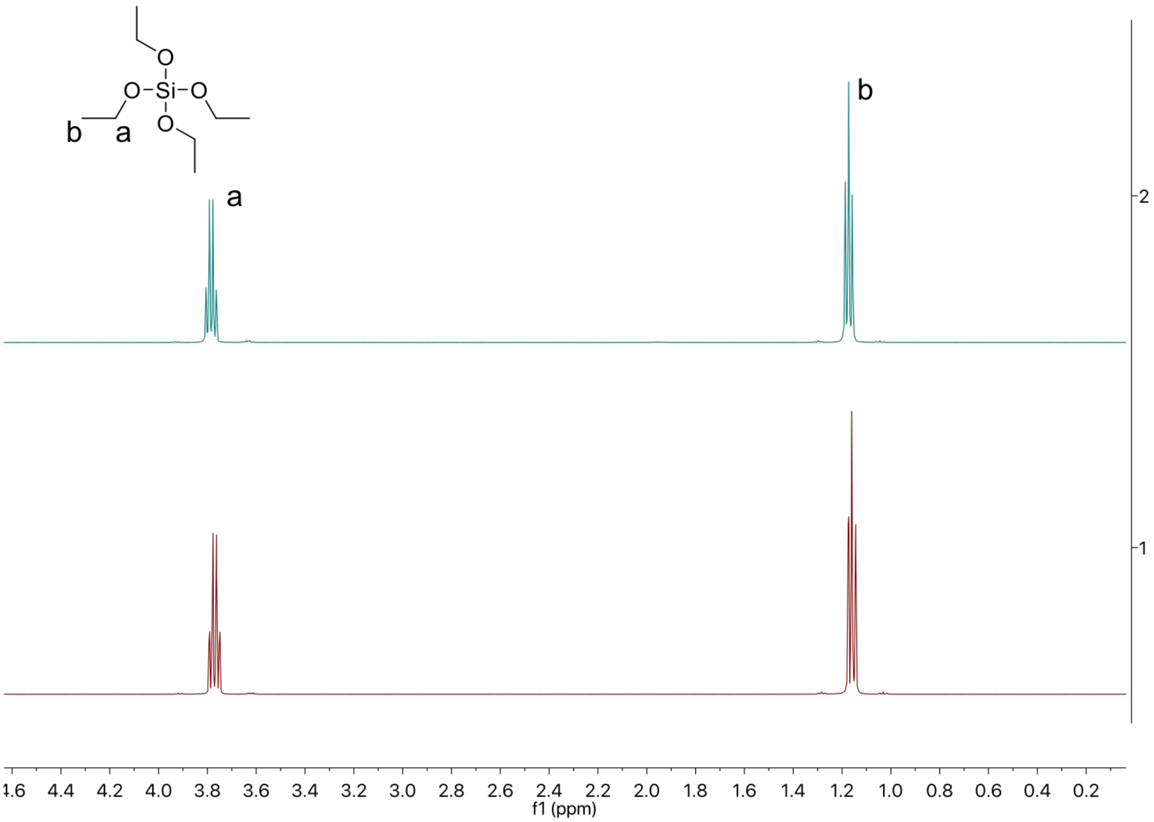

Figure 2.6: *^{1}H-NMR Spectra of TEOS*. Before (bottom) and after (top) purification by distillation.

consistent with new reagents, as evidenced by TEM (Figure 2.8). APTES was similarly distilled and evaluated by ^{1}H-NMR. The ^{1}H-NMR spectrum of impure APTES contains one apparent impurity peak, a quartet centered at 3.6 ppm (Figure 2.9), which is not present after distillation. ^{13}C-NMR revealed two impurity peaks, which indicate more clearly than the ^{13}C-NMR that the impurity is ethanol (Figure 2.10). Alkyl silicates readily hydrolyze, which explains the presence of ethanol in the APTES reagent.

Improper storage and lack of purification of the silicate starting materials has been identified as the origin of the bimodal distribution of Comiskey's Dex-SiO_2-NPs. Though the lone impurity identified via NMR was ethanol, it likely results from hydrolysis of the silicate to silicic acid based on understanding of the reactivity of the reagents.[104] These results, as well as the distribution of resulting Dex-SiO_2-NPs, support the hypothesis that APTES and TEOS hydrolyzed into more

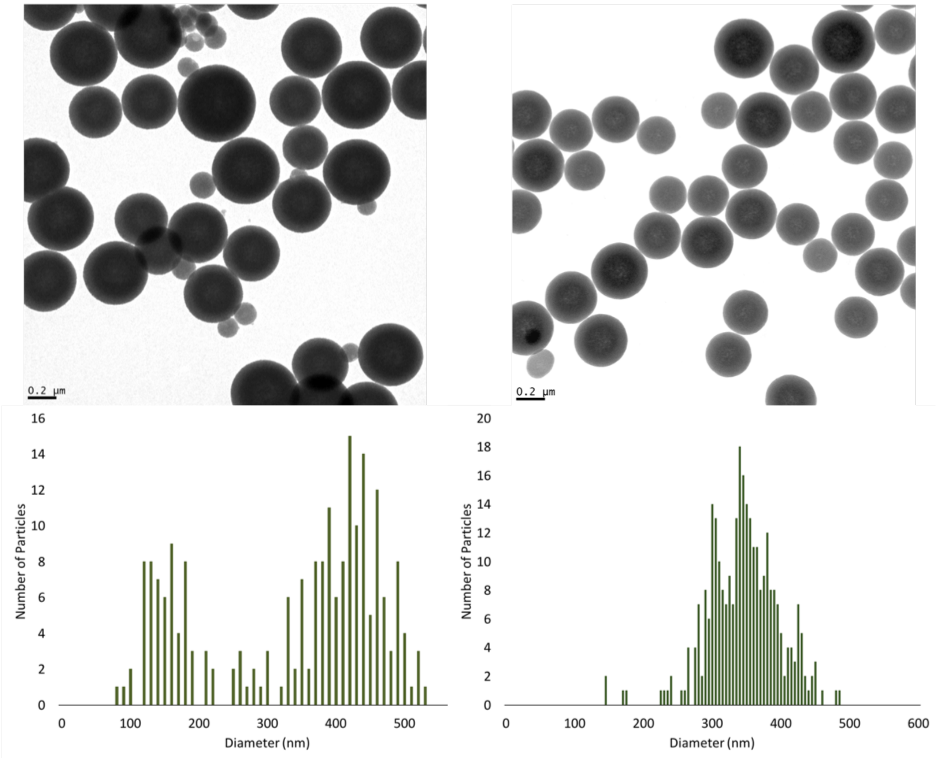

Figure 2.7: *TEM Micrographs and Number Distributions of Dex-SiO$_2$-350 NPs.* Dex-SiO$_2$-350 NPs prepared with impure (left) and distilled (right) TEOS. 27kx magnification, scale bar 0.2 μm. Brightness enhanced by 20% to emphasize detail.

reactive silicic acids under improper storage conditions. This decomposition was mitigated in the future by storing silicon alkoxide reagents under inert gas and distilled periodically in order to maintain reagent purity and produce uniform Dex-SiO$_2$-NPs.

2.3 Size Control in Modified Stöber Silica Nanoparticle Synthesis

With purified starting materials in hand, the dextran-modified Stöber method was further developed. The classical Stöber method adjusts the concentrations of TEOS, ethanol, water, and ammonium hydroxide as a means to adjust the rates of hydrolysis and condensation, in turn tuning the NP diameter. With the addition of 10 kDa dextran to the synthesis solution, resulting NP diameters vary from those expected based on the studies of Stöber and others.

Building upon the optimization of Comiskey's work described above and the precedent established by Stöber and others, reagents were adjusted to afford Dex-SiO$_2$-NPs with decreased average

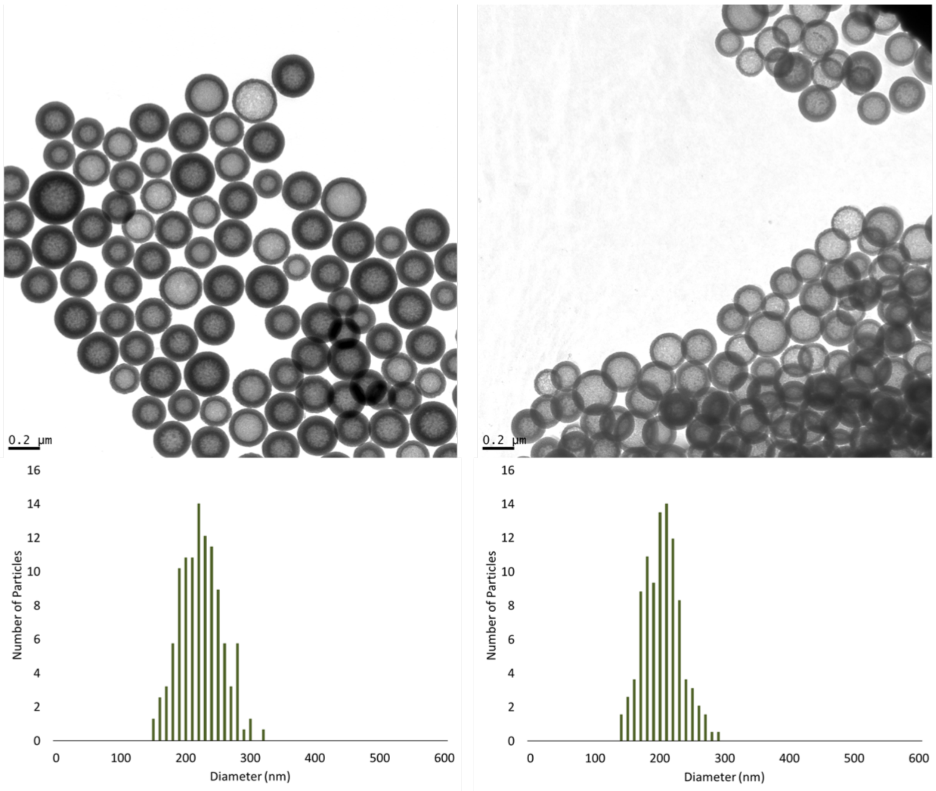

Figure 2.8: *TEM Micrographs and Number Distributions of Dex-SiO_2-250 NPs.* Dex-SiO_2-250 NPs prepared with distilled (left) and new (right) TEOS. 27kx magnification, scale bar 0.2 μm. Brightness enhanced by 20% to emphasize detail.

Table 2.1: *Nanoparticle Diameter as a Function of Reagent Concentrations.*

NP	NH_4OH (M)	H_2O (M)	TEOS (M)	Average NP Diameter (nm)
Dex-SiO_2-100	0.6	10.6	0.001	100
Dex-SiO_2-200	0.7	5.5	0.01	200
Dex-SiO_2-240	0.6	10.6	0.01	240
Dex-SiO_2-350	0.6	15.6	0.01	350

diameters (Figure 2.11, Table 2.1). Decreasing the concentration of H_2O from 15.6 M to 10.6 M afforded a decrease in average NP diameter by approximately 100 nm. Further decreasing the concentration of H_2O to 5.5 M, along with an increase in NH_4OH to 0.7 M produced Dex-SiO_2-NPs with an average diameter of 200 nm. Dex-SiO_2-NPs with average diameters of approximately 100 nm were obtained by decreasing the concentration of TEOS from 0.01 M to 0.001 M, with variation of other reagents only resulting in 200 nm NPs. Generally, decreasing the concentration of H_2O and increasing the concentration of NH_4OH decreases the average diameter of the Dex-SiO_2-NPs

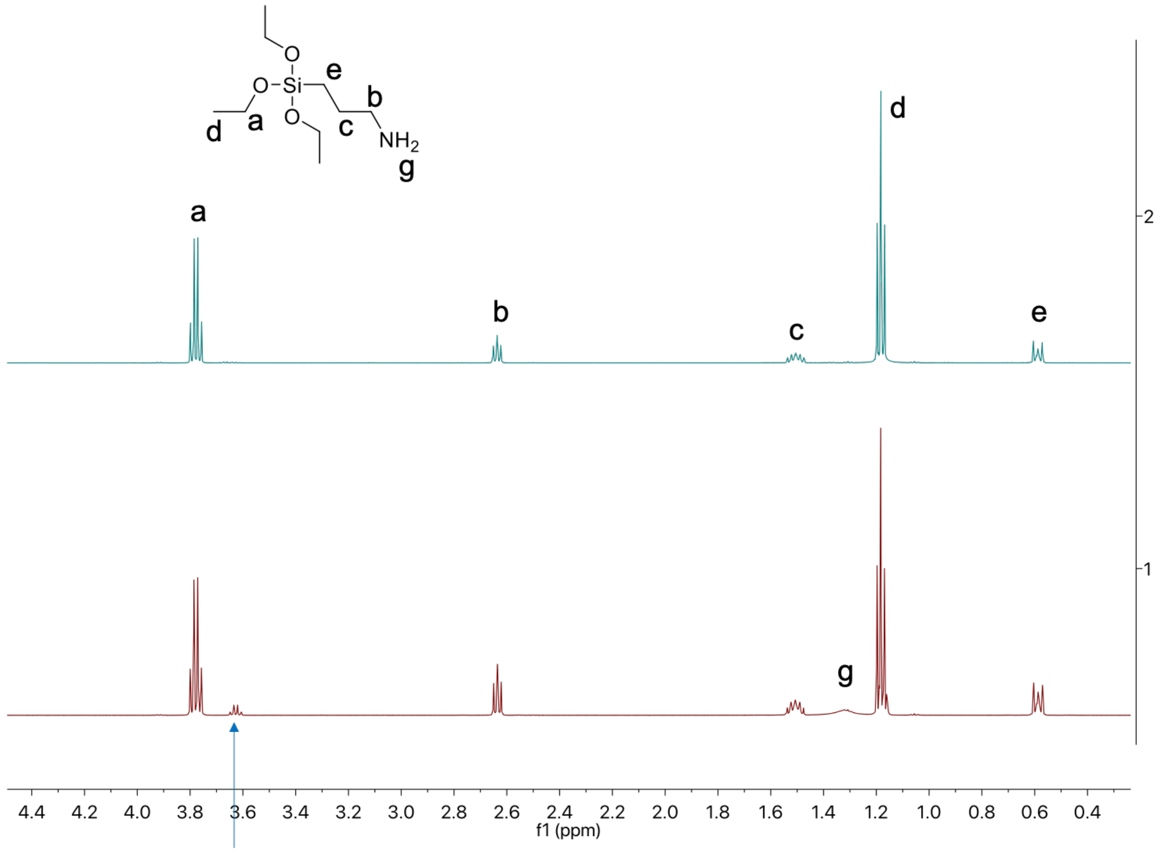

Figure 2.9: *^{1}H-NMR Spectra of APTES*. Before (bottom) and after (top) purification by distillation. Arrow indicates impurity peaks attributed to ethanol.

most closely related to Comiskey's Dex-SiO_2-NP. In addition to the observed decrease in diameter, Dex-SiO_2-NPs have characteristic hollow centers, which are further investigated in Chapter 3.

Beyond Comiskey's Dex-SiO_2-NP synthetic configuration, NH_4OH and H_2O were further studied to probe the effects of the different reagents on NP diameter. The average diameters of Dex-SiO_2-NPs were compared according to the concentrations of NH_4OH and H_2O used in their preparation. Some anomalies exist, though a general trend may be extracted. While a greater range of reagent concentrations would provide more generalizable conclusions, the current study indicates that Dex-SiO_2-NP diameters increase with increasing NH_4OH and H_2O concentrations (Figure 2.12, Figure 2.13). Greater concentrations of NH_4OH result in the opposite trend, with the greatest diameters resulting from the least amount of H_2O.

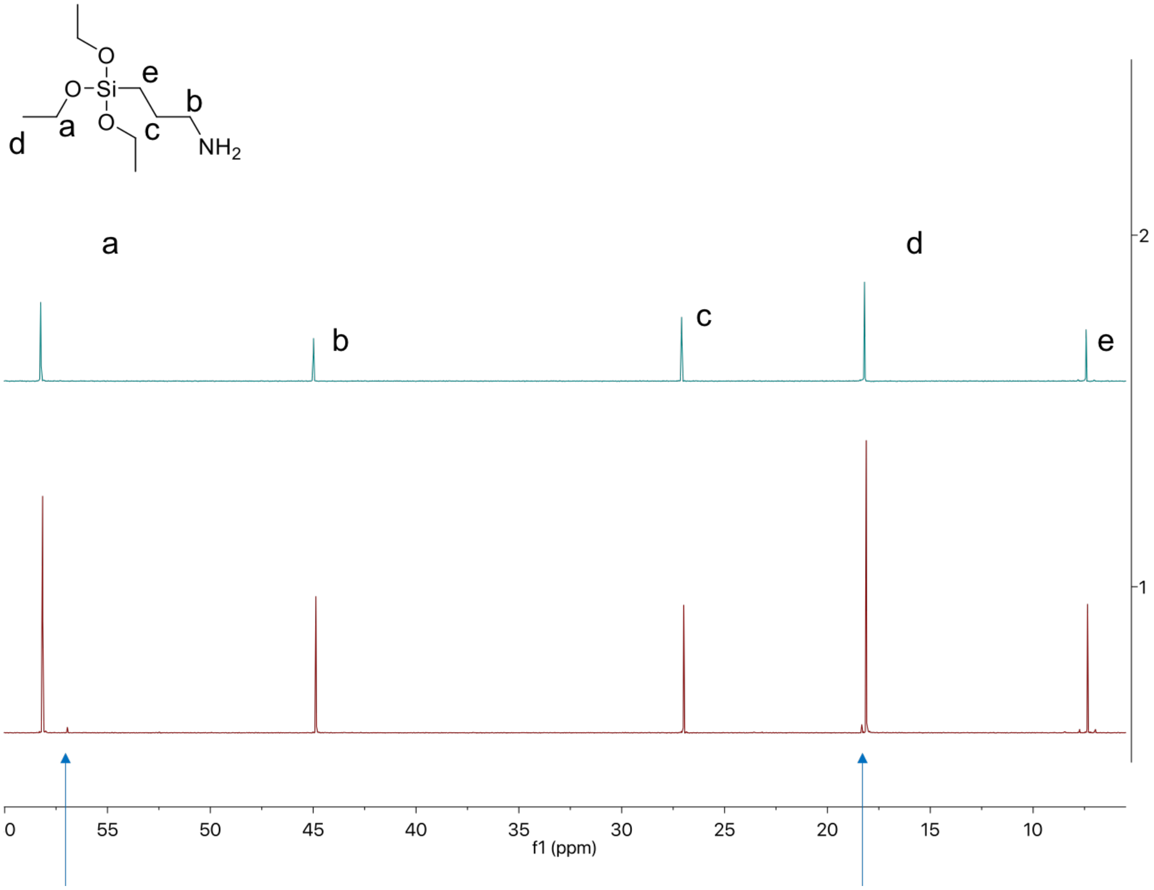

Figure 2.10: *^{13}C-NMR Spectra of APTES*. Before (bottom) and after (top) purification by distillation. Arrows indicate impurity peaks attributed to ethanol.

Rates of hydrolysis and condensation of alkyl silicates are governed by the concentrations of hydroxide and water within the reaction solution. The results observed here are consistent with those of Stöber and others,[18,105] NP diameter increases with increasing H_2O and NH_4OH concentrations to a maximum, followed by a decrease in diameter at the highest concentrations.

Among the conditions studied, there was persistent difficulty obtaining monodispersed Dex-SiO_2-NPs with diameters less than 200 nm, which would be ideal for gaining entry to cells for therapeutic delivery applications. Decreasing the concentration of TEOS was successful in obtaining Dex-SiO_2-NPs having an average diameter of approximately 100 nm (Figure 2.14). Adjusting the concentration of TEOS within Dex-SiO_2-250 by $\frac{1}{4}$ and $\frac{1}{8}$ (Figure 2.14 left and left-center, respectively) afforded very similar monodisperse distributions of NPs. Despite the

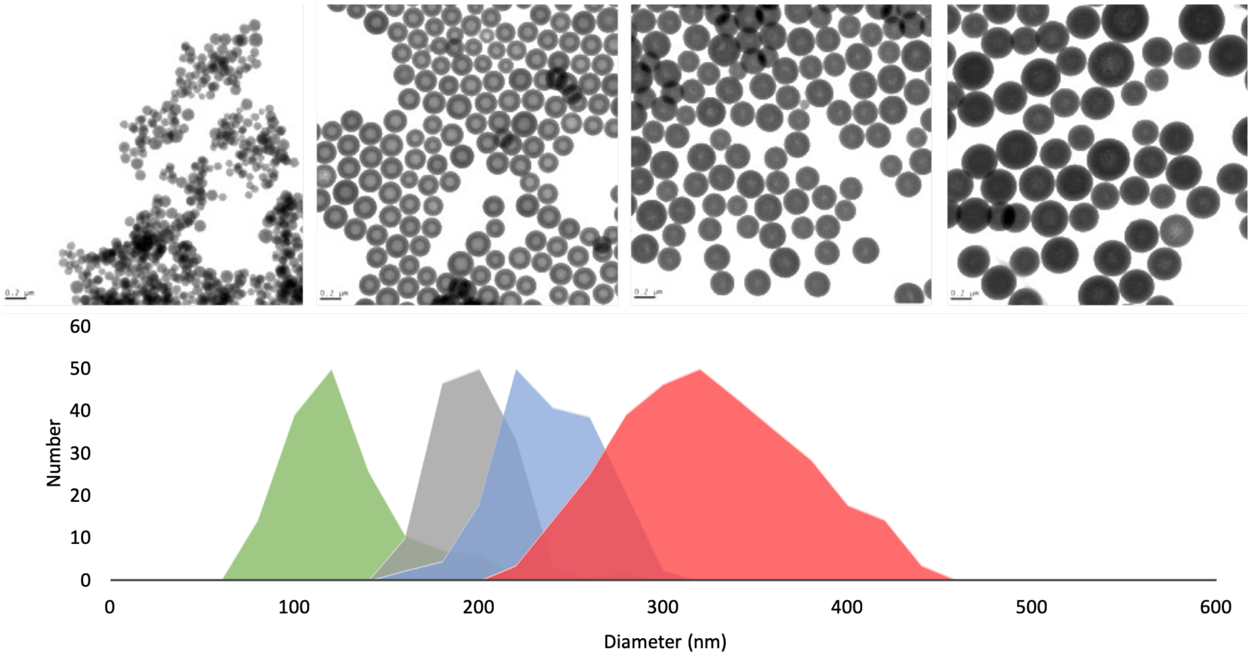

Figure 2.11: *TEM Micrographs and Number Distributions of Dex-SiO$_2$-NPs*. From left: Dex-SiO$_2$-100, Dex-SiO$_2$-200, Dex-SiO$_2$-250, Dex-SiO$_2$-350. 27kx magnification, scale bar 0.2 μm. Brightness enhanced by 20% to emphasize detail.

similarities in their distributions, these two NPs vary in their morphology, with Dex-SiO$_2$-250-$\frac{1}{4}$TEOS having a more spherical appearance and Dex-SiO$_2$-250-$\frac{1}{8}$TEOS having a rougher surface. Similarly, Dex-SiO$_2$-350-$\frac{1}{4}$TEOS and Dex-SiO$_2$-350-$\frac{1}{8}$TEOS have similar average diameters but different apparent surface morphologies (Figure 2.14 right-center and right, respectively).

APTES is a key component in transforming Dex-SiO$_2$-NPs into effective delivery vehicles, as the amine moiety can electrostatically bind nucleic acids. Integration of APTES into these smaller NPs at a decreased concentration proportional to TEOS does not significantly alter the size distribution or morphology of any of the studied conditions (Figure 2.15).

Decreasing the amount of TEOS and dextran in the reaction mixture did not produce significantly smaller Dex-SiO$_2$-NPs (Figure 2.16). Nevertheless, these NPs do appear to have a smoother shell, which is to be expected as the amount of dextran and TEOS are scaled evenly from the original amounts in both populations.

The Dex-SiO2-NPs discussed to this point were prepared with 9-11 kDa dextran and have unique

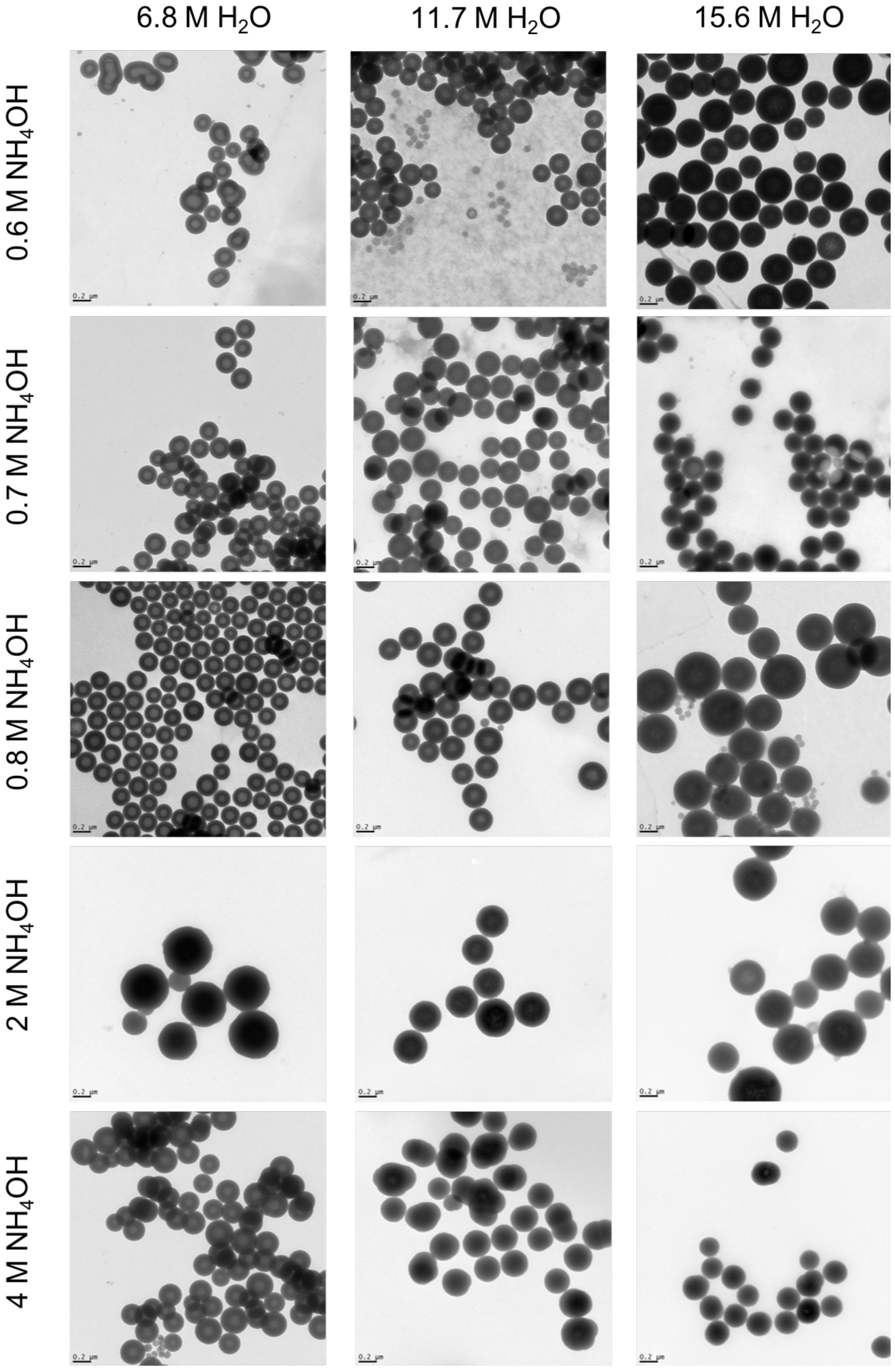

Figure 2.12: *TEM Micrographs of Dex-SiO_2-NPs upon Variation of Reagents*. With 0.011 M TEOS, in ethanol. 27kx magnification, scale bar 0.2 μm. Brightness enhanced by 20% to emphasize detail.

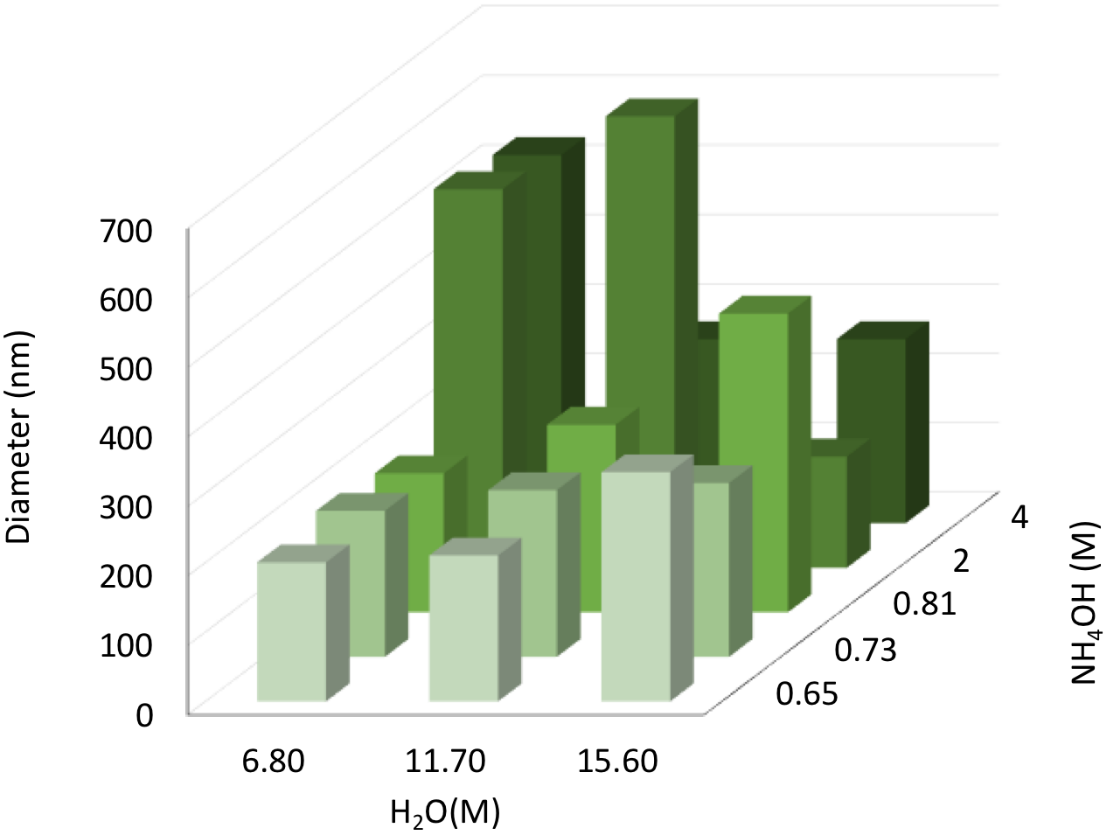

Figure 2.13: *Average Diameters of Dex-SiO_2-NPs upon Variation of Reagents*. With 0.011 M TEOS, in ethanol.

morphology and have been shown to enhance silencing by siRNA *in vitro*.[12] Further exploration of size, morphology, and function as delivery vehicles was pursued via incorporation of different dextrans and carbohydrates (Scheme 2.17). In each case, the alternative carbohydrate was used in place of 9-11 kDa dextran as indicated in Table 2.2.

TEM micrographs of alternative carbohydrate NPs prepared according to Dex-SiO_2-250 conditions are shown in Figure 2.18. NPs prepared using 6kDa dextran and 40 kDa dextran closely resemble those prepared using 9-11 kDa dextran in size and appearance, as both populations contain hollow centers. NPs prepared using α-cyclodextrin and β-cyclodextrin (CDex-SiO_2-NPs) are more bimodal in diameter compared to the 6 kDa, 9-11 kDa, and 40 kDa NPs. Additionally, CDex-SiO_2-NPs do not appear to have a hollow center. While dextrans and cyclodextrins share

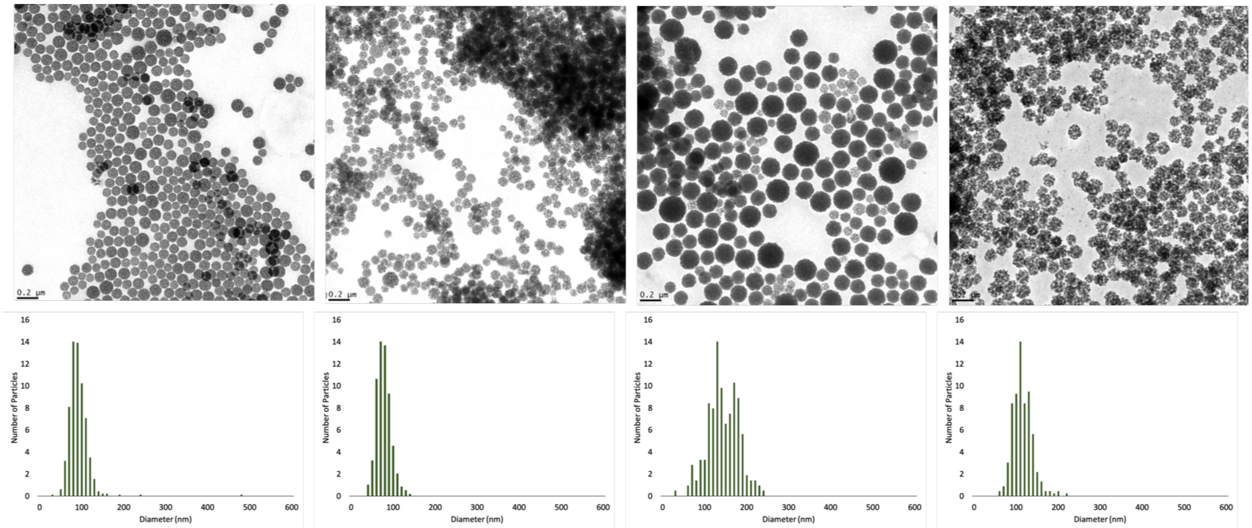

Figure 2.14: *TEM Micrographs and Number Distributions of Dex-SiO_2-NPs*. From left: Dex-SiO_2-250-$\frac{1}{4}$TEOS, Dex-SiO_2-250-$\frac{1}{8}$TEOS, Dex-SiO_2-350-$\frac{1}{4}$TEOS, Dex-SiO_2-350-$\frac{1}{8}$TEOS. 27kx magnification, scale bar 0.2 μm. Brightness enhanced by 20% to emphasize detail.

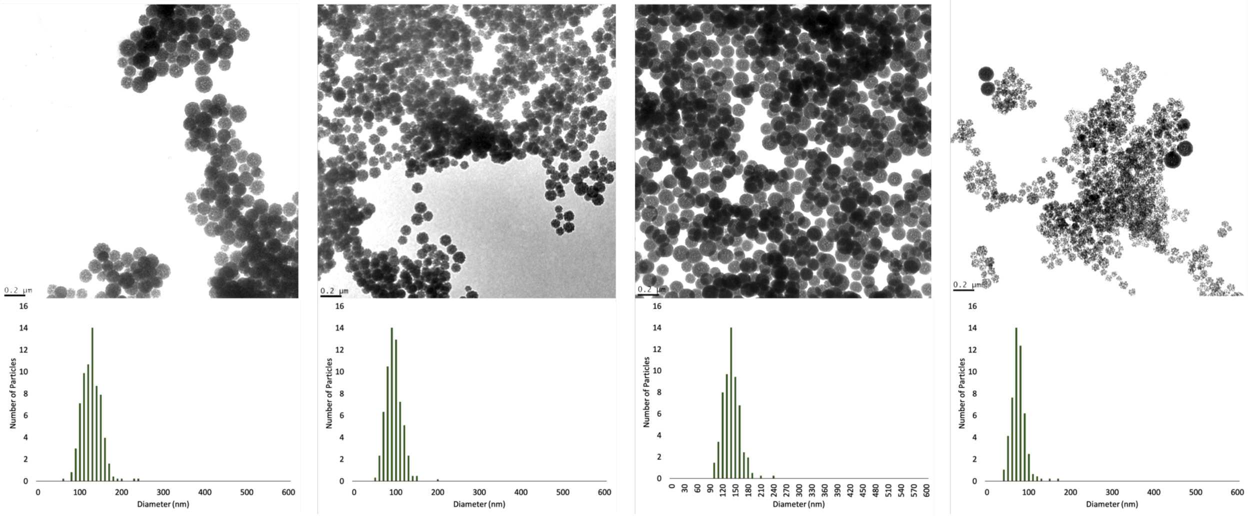

Figure 2.15: *TEM Micrographs and Number Distributions of Dex-Amine-SiO_2-NPs*. From left: Dex-Amine-SiO_2-250-$\frac{1}{4}$TEOS, Dex-Amine-SiO_2-250-$\frac{1}{8}$TEOS, Dex-Amine-SiO_2-350-$\frac{1}{4}$TEOS, Dex-Amine-SiO_2-350-$\frac{1}{8}$TEOS. 27kx magnification, scale bar 0.2 μm. Brightness enhanced by 20% to emphasize detail.

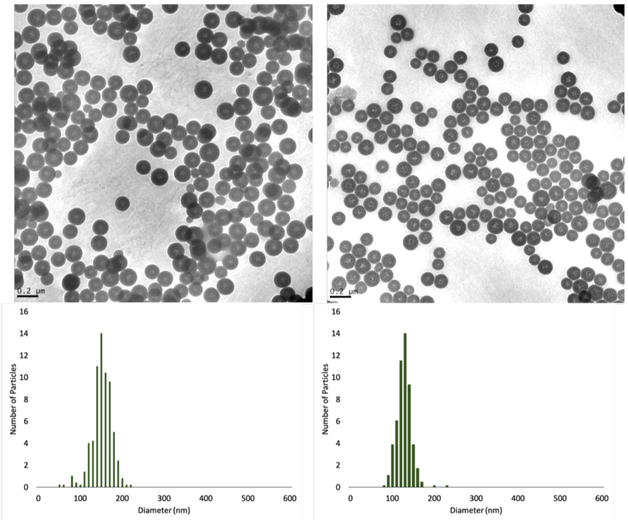

Figure 2.16: *TEM Micrographs and Number Distributions of Dex-SiO$_2$-NPs*. From left: $\frac{1}{4}$Dex-SiO$_2$-250-$\frac{1}{4}$TEOS, $\frac{1}{8}$Dex-SiO$_2$-250-$\frac{1}{8}$TEOS. 27kx magnification, scale bar 0.2 μm. Brightness enhanced by 20% to emphasize detail.

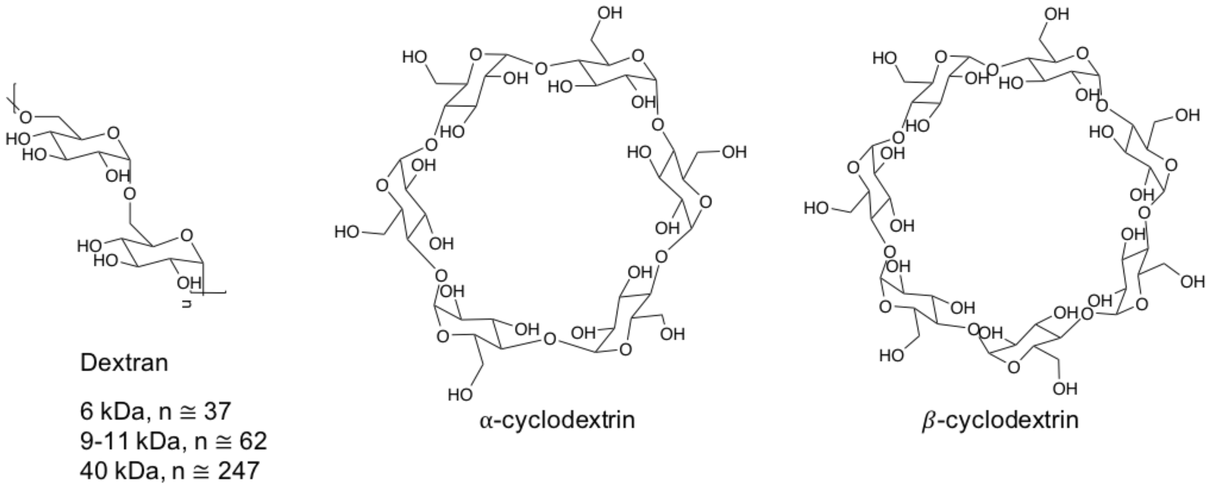

Figure 2.17: *Structures of Dextran and Cyclodextrins*. Dextrans of varying molecular weight and α-cyclodextrin and β-cyclodextrin.

Table 2.2: *Dex-SiO$_2$-NP Diameters with Dextran Variation.*

Carbohydrate	Hydrodynamic Diameter of Dextran in MQ H_2O	Dex-SiO$_2$-NP Synthesis Conditions	Weighted Average NP Diameter (nm)
6 kDa Dextran	3	Dex-SiO$_2$-200	146
6 kDa Dextran	3	Dex-SiO$_2$-250	194
6 kDa Dextran	3	Dex-SiO$_2$-350	318
10 kDa Dextran	6	Dex-SiO$_2$-200	211
10 kDa Dextran	6	Dex-SiO$_2$-250	245
10 kDa Dextran	6	Dex-SiO$_2$-350	276
40 kDa Dextran	7	Dex-SiO$_2$-200	187
40 kDa Dextran	7	Dex-SiO$_2$-250	242
40 kDa Dextran	7	Dex-SiO$_2$-350	312
α-Cyclodextrin	-	Dex-SiO$_2$-200	168
α-Cyclodextrin	-	Dex-SiO$_2$-250	311
α-Cyclodextrin	-	Dex-SiO$_2$-350	63
β-Cyclodextrin	-	Dex-SiO$_2$-200	259
β-Cyclodextrin	-	Dex-SiO$_2$-250	391
β-Cyclodextrin	-	Dex-SiO$_2$-350	63

the glucose monomer, the greater structure varies from a branched polymer to a wreath of discrete glucose units which could certainly impact NP assembly.

2.4 Growth of Dex-SiO$_2$-NPs

Pursuant to understanding the formation of Dex-SiO$_2$-NPs, samples of reaction solution were extracted at designated points in the synthesis process, purified, and studied by TEM. The synthetic procedure employed here, as described in Chapter 6, first dissolves dextran in MilliQ water. After stirring ethanol, NH_4OH and MilliQ water, dextran is added and allowed to stir for 10 minutes. TEOS is then added, and the reaction solution is stirred 10 minutes before the addition of APTES. Samples were extracted using a syringe, diluted, and centrifuged. After removal of the supernatant liquid, the remaining solids are rinsed three times with MilliQ water before suspension in ethanol for deposition on a TEM grid. Key points in this process at which samples were extracted include soon after addition of TEOS, immediately before APTES addition, and after APTES addition. Figure 2.19 includes several TEM micrographs from this process.

After TEOS addition, dark, amorphous aggregates are evident, as well as a strand-like network

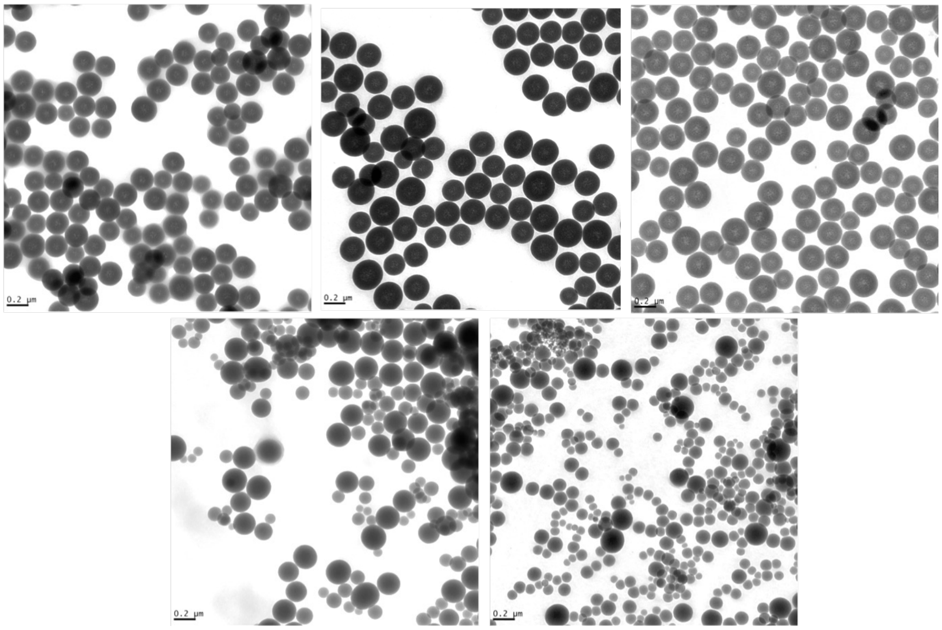

Figure 2.18: *TEM Micrographs of Dex-SiO$_2$-NPs Prepared with Different Dextrans*. Top, from left: 6 kDa, 9-11 kDa, 40 kDa. Bottom, from left: α-cyclodextrin, β-cyclodextrin prepared using Dex-SiO$_2$-250 conditions. 27kx magnification, scale bar 0.2 μm. Brightness enhanced by 20% to emphasize detail.

of a lighter shade. The TEM micrograph collected after several more minutes of stirring TEOS in the dextran-containing reaction solution shows more spherical aggregates, though smaller, lighter objects are still evident. With APTES addition (Figure 2.19, bottom), spherical nanoparticles quickly took shape. There is no observable change in the observed NPs between 4 minutes and 8 minutes post APTES addition. 20 hours after APTES addition a bimodal size distribution is observed. Extraction of more samples within that time frame may have provided information pertaining to the origins of the bimodal distribution. Further, it should be noted that these experiments were conducted prior to Dex-SiO$_2$-NP synthetic optimization, resulting in the bimodal distribution of nanoparticles.

Curious about the process in the absence of APTES, the same experiment was conducted without the addition of APTES (Figure 2.20). In this case, after preparation of the grid for TEM analysis, a solution of 5% periodic acid was applied to the grid in order to oxidize dextran, followed by a silver methanamine stain which would stain the dextran by precipitating silver. While the staining process could provide valuable insight into the location of dextran, in practice it raised questions as to which of the dark crystalline regions result from stained dextran and which result from SiO_2-NP or Dex-SiO_2-NP precipitation.

Aggregates similar to those apparent in Figure 2.19 were evident at 4, 8, and 20 minutes after TEOS addition (Figure 2.20). Spherical nanoparticle structures were evident in the TEM micrographs beginning at 30 minutes post TEOS addition. One hour after TEOS addition, both spherical nanoparticles and aggregates were evident. These observations are consistent with the nucleation and aggregation mechanism for SiO_2-NP assembly discussed by Han and others.[20] Closer examination of Dex-SiO_2-NPs 60 minutes after the addition of TEOS evidences abundant granules on the surface of the two nanoparticles shown in the micrograph (Figure 2.21). Upon cursory analysis, one may speculate that this suggests that dextran is accessible from the surface both by periodic acid and silver methanamine, which would certainly an exciting prospect. Nevertheless, the nature of this experiment is such that one cannot eliminate the possibility that these granules

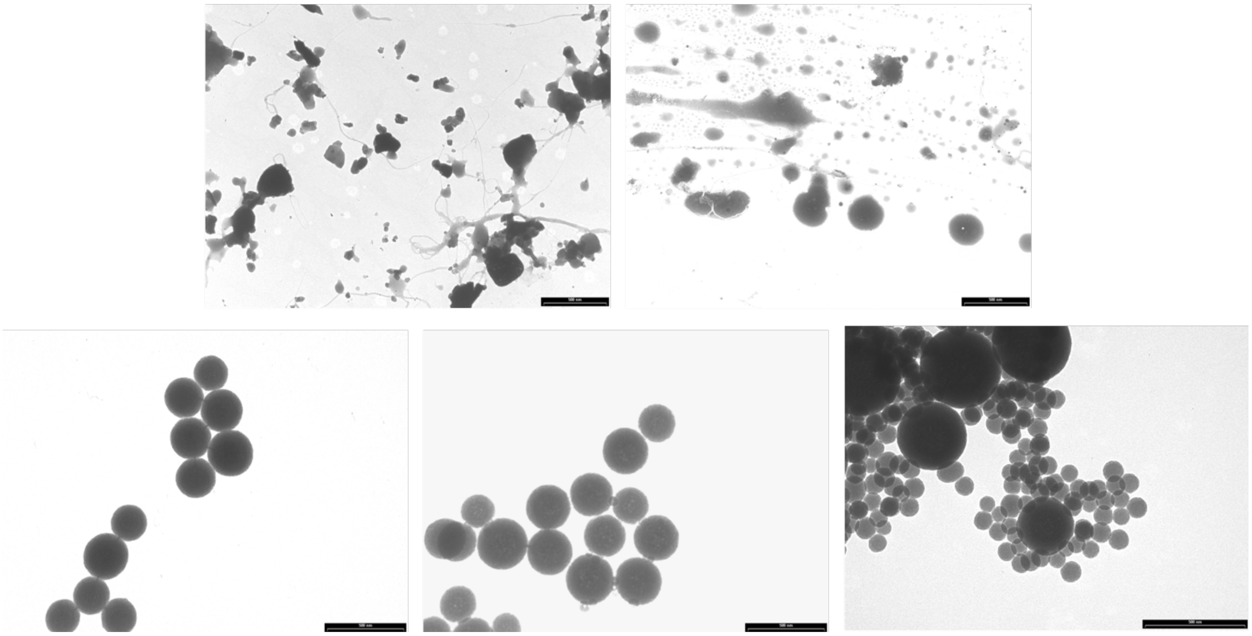

Figure 2.19: *TEM Micrographs of Purified Reaction Mixture during Dex-SiO_2-350 NP Synthesis*. Top, from left: 5.45 minutes post TEOS, 8.3 minutes post TEOS. Bottom, from left: 4 minutes post APTES, 8.3 minutes post APTES, 20 hours post APTES. Scale bar 500 nm. Brightness enhanced by 20% to emphasize detail.

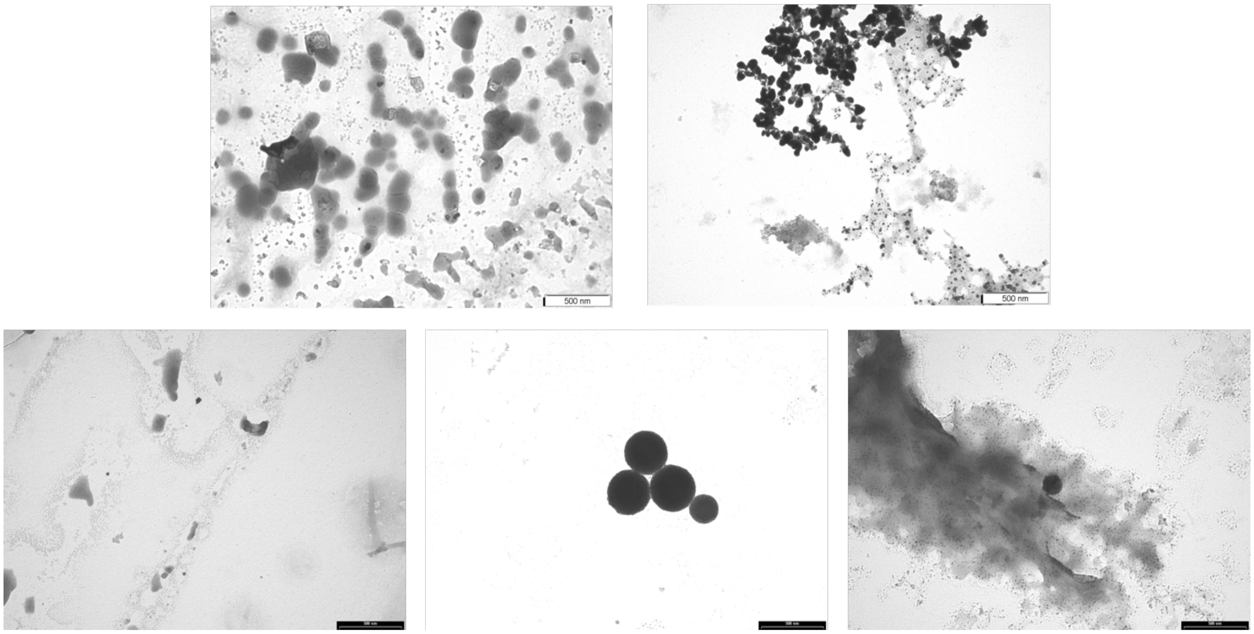

Figure 2.20: *TEM Micrographs of Purified Reaction Mixture during Dex-SiO$_2$-350 NP Synthesis*. Top, from left: 4 minutes post TEOS, 8 minutes post TEOS. Bottom, from left: 20 minutes post TEOS, 30 minutes post TEOS, 60 minutes post TEOS. Stained using silver methanamine to detect dextran after NPs were deposited onto TEM grid. Scale bar 500 nm. Brightness enhanced by 20% to emphasize detail.

originate from excess dextran in the reaction solution having adhered to the nanoparticle surface whilst the sample upon the TEM grid dried.

Though CDex-SiO$_2$-NPs were not studied in this way, one could hypothesize that the structural differences between branched dextran and cyclodextrin would influence the formation of Dex-SiO$_2$-NPs compared to CDex-SiO$_2$-NPs. Additionally, while these microscopic observations provide insight to the process of Dex-SiO$_2$-NP formation, it is important to acknowledge the effect of purification procedures and sample preparation, including drying, may have on the results.

A new hypothesis of Dex-SiO$_2$-NP formation based on dextran solubility emerged. Polymer solubility is known to be a complex relationship between polymers and non-polymeric solvents. In simplest terms, the θ solvent is one in which a polymer behaves as an ideal random coil.[106] The process of Dex-SiO$_2$-NP synthesis is described in Figure 2.22. 9-11 kDa dextran dissolved in water is added to the reaction solution of ethanol, water, and ammonium hydroxide while stirring.

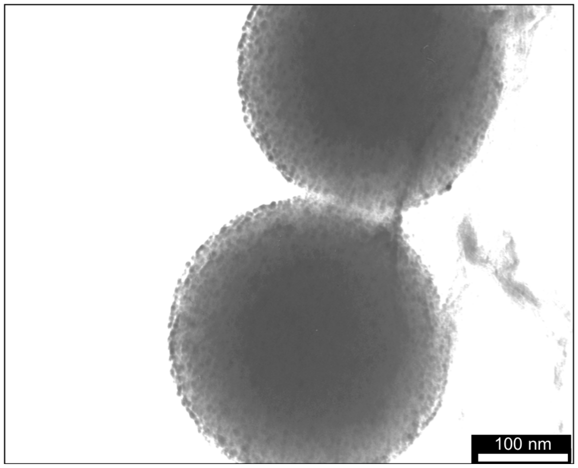

Figure 2.21: *TEM Micrograph of Dex-SiO$_2$-350 NPs During Synthesis.* 60 minutes post TEOS. Stained using silver methanamine to detect dextran after NPs were deposited onto TEM grid. Scale bar 100 nm. Brightness enhanced by 20% to emphasize detail.

It is possible that this solution is not ideal for dextran solubility, which may result in aggregates of dextran existing within aqueous solvation spheres (Figure 2.22, top center). Upon TEOS additon to this solution, condensation around these localized water-rich aggregates could result in the

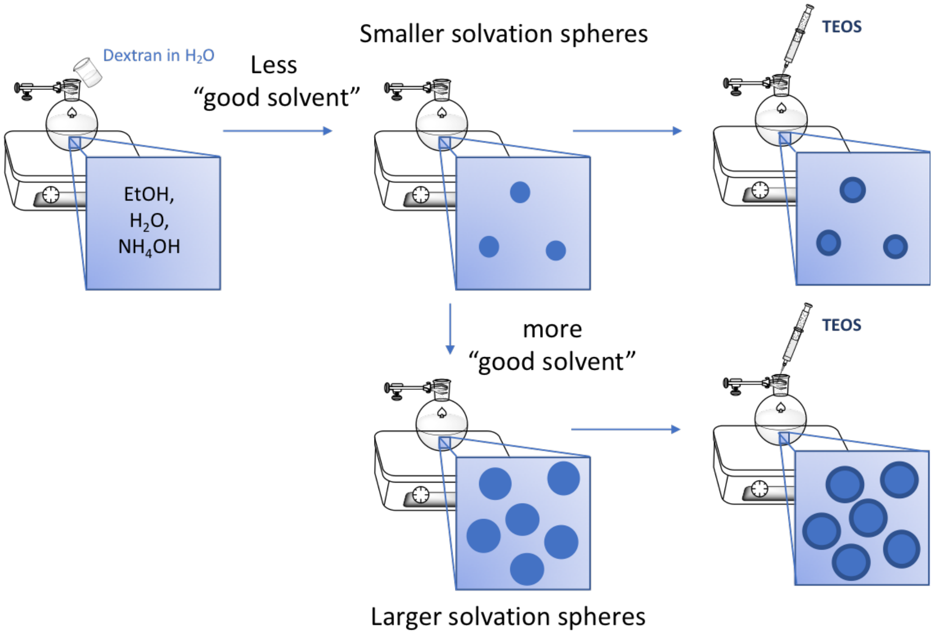

Figure 2.22: *Diagram Depicting Dex-SiO$_2$-NP Synthesis and Dextran Solubility Hypothesis.*

hollow center morphology observed. Alternatively, in the presence of more "good solvent" (i.e. a higher concentration of H_2O, Dex-SiO_2-350 compared to Dex-SiO_2-200) dextran will dissolve to a greater extent, possibly existing as a random coil and resulting in greater dispersion throughout NPs.[107] Alternatively, it's possible that the increased concentration will expand the solvation spheres resulting in larger aggregates, and larger Dex-SiO_2-NPs (Figure 2.22).

This hypothesis was probed by measuring the hydrodynamic radii of aggregates when dextran dissolved in MilliQ water is mixed in reaction solutions containing methanol, ethanol, and isopropanol as a function of time (Figure 2.23). Presently, water is added to dextran and the solution is manually agitated and given the opportunity to dissolve over a period of ten minutes prior to addition to the reaction mixture. Greater precautions could be taken to ensure that dextran is well-dissolved in water before addition to the reaction solution. The greater polarity and decreased steric effects of methanol compared to ethanol and isopropanol increase its ability to solvate water. Since dextran is water-soluble, the increased solubility of water in methanol is expected to enlarge the solvation sphere. The aggregates in methanol observed by DLS are expected be larger than those of the other two solvents. This hypothesis was validated by DLS results, which evidenced that aggregates arising from the solution containing methanol and dextran were the largest, with the isopropanol solution giving rise to the smallest aggregates.

In solutions where dextran and TEOS were added, which most resemble Dex-SiO_2-NP synthetic conditions, methanol aggregates were the largest, followed by isopropanol and then ethanol, though the last two were similar. In conditions that excluded dextran (Figure 2.23, bottom), methanol again produced the largest aggregates, while isopropanol and ethanol solutions were very similar. There was no significant change in aggregate size over the course of 140 minutes.

Dex-SiO_2-NPs and SiO_2-NPs resulting from these experiments are shown in Figures 2.24 and 2.25, respectively. From the starting point of Dex-SiO_2-NPs synthesized in ethanol solution, both methanol and isopropanol-produced NPs exhibit a decrease in diameter. The SiO_2-NPs produced in the absence of dextran produced monomodal size distributions. The distributions of NPs produced in methanol and ethanol were approximately the same size, though the breadth of distributions

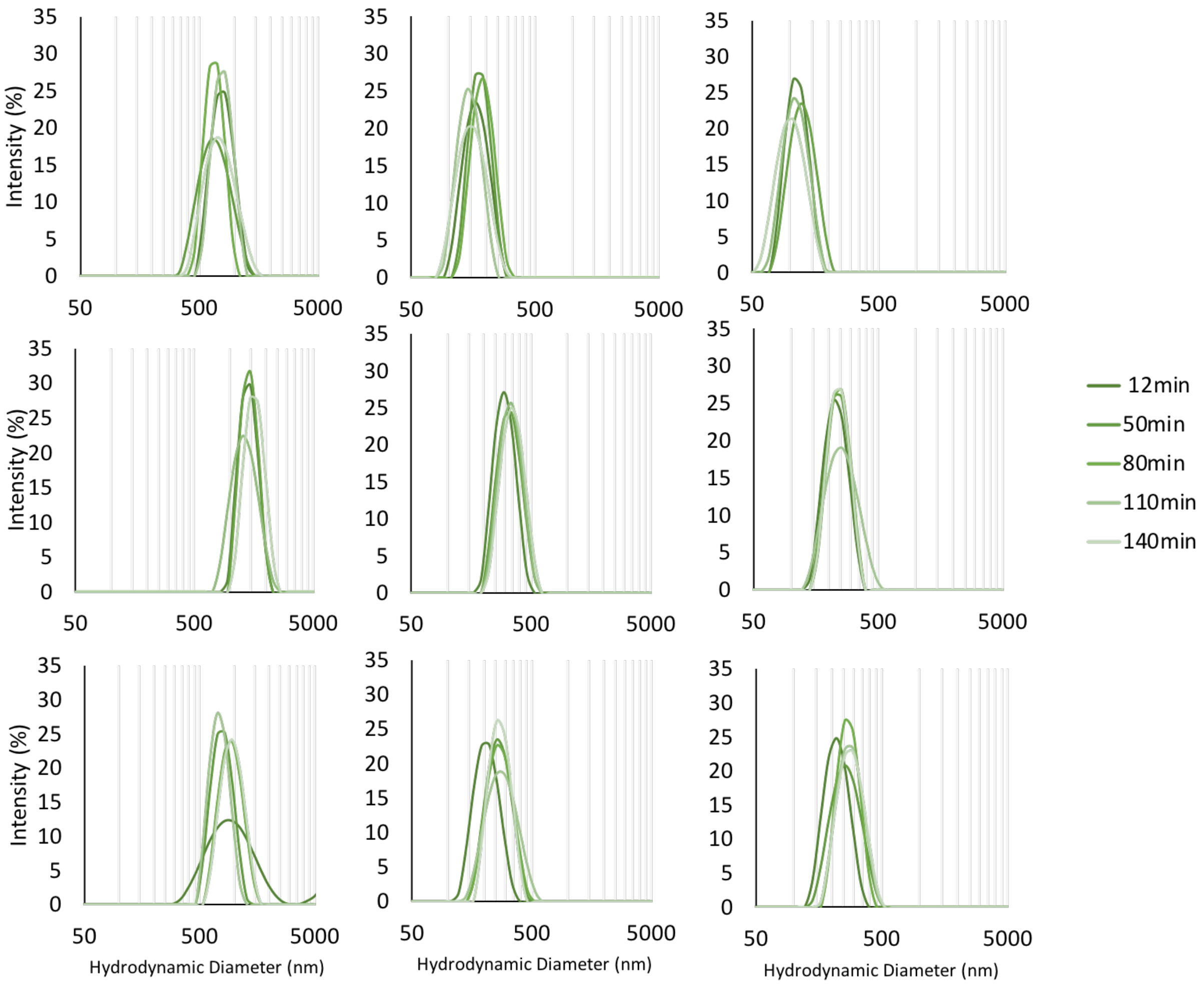

Figure 2.23: *Hydrodynamic Diameter of Aggregates During Dex-SiO$_2$-NP Synthesis.* Solution of Dex-SiO$_2$-250 conditions with methanol (left), ethanol (center), and isopropanol (right), containing 9-11 kDa dextran (top), dextran and TEOS (middle), and TEOS (bottom).

varied among the larger and smaller populations. NPs produced in the isopropanol solution were larger than those in ethanol or methanol.

DLS results indicate that time does not play a significant role in aggregation in the process of NP synthesis. Based on these results, correlation of dextran aggregate size and resulting NP diameter is only observed in cases using ethanol. The different morphologies observed in Dex-SiO$_2$-NPs synthesized in methanol and isopropanol suggests that dextran may be incorporated differently. Further studies varying polarity and sterics via different solvents may provide further insight into dextran aggregation and NP formation.

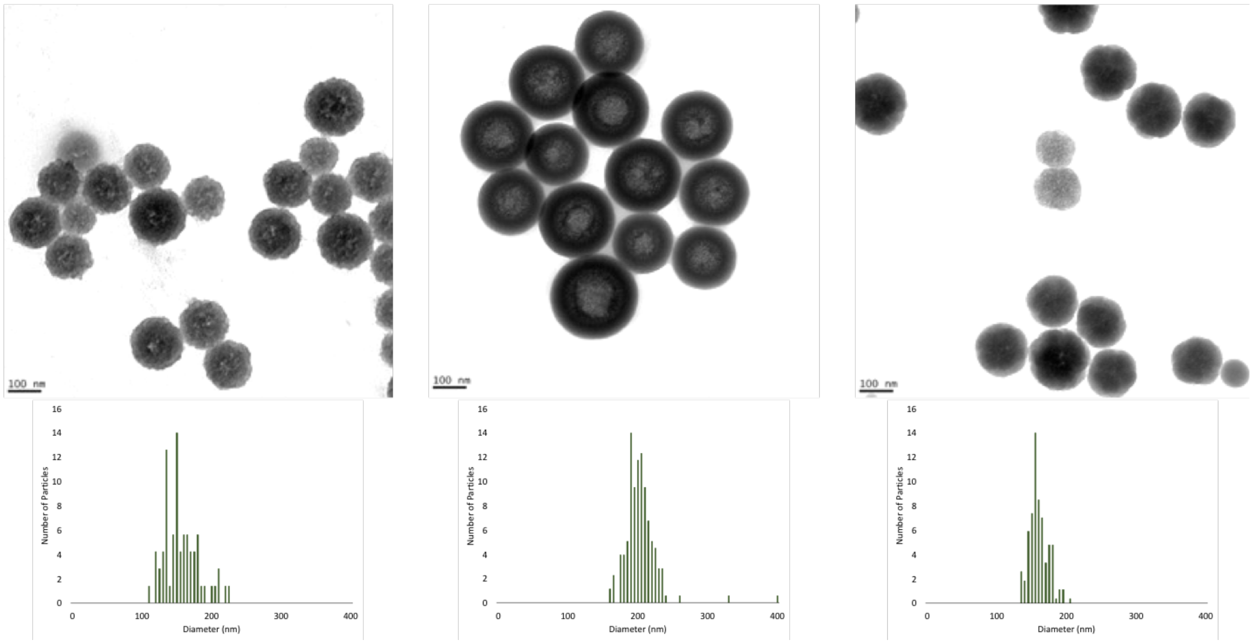

Figure 2.24: *TEM Micrographs and Number Distributions of Dex-SiO$_2$-NPs Prepared Using Methanol, Ethanol, and Isopropanol*. 67kx Magnification, scale bar 100 nm. Brightness enhanced by 20% to emphasize detail.

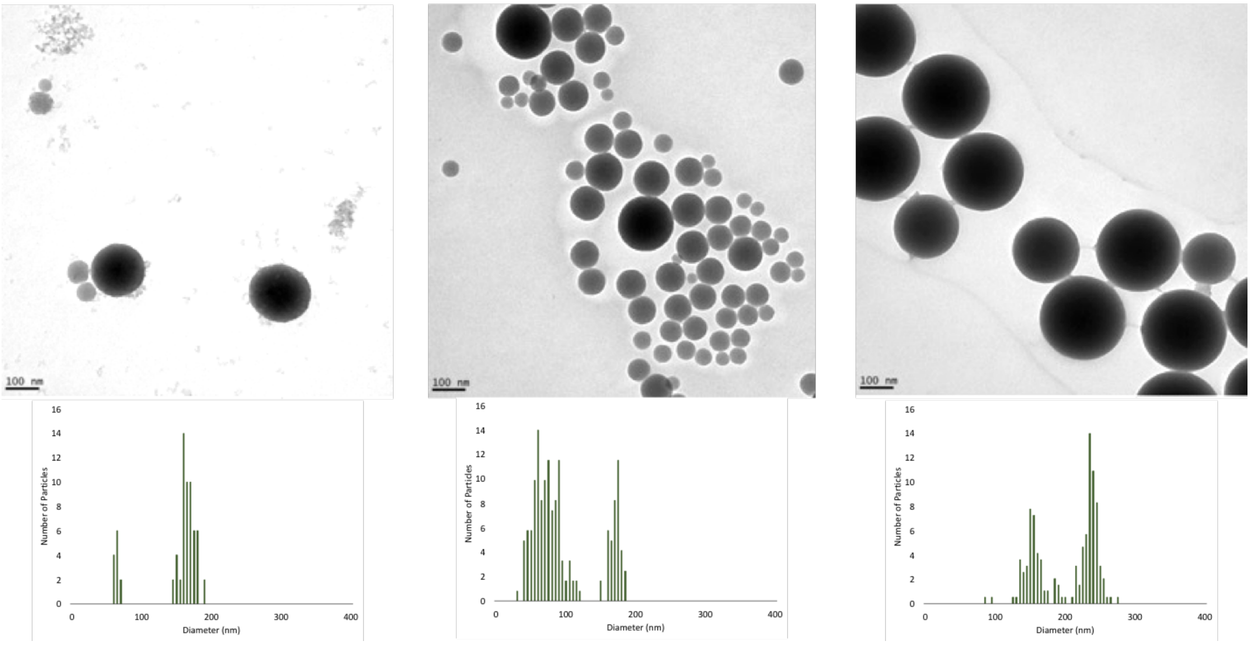

Figure 2.25: *TEM Micrographs and Number Distributions of SiO$_2$-NPs Prepared Using Methanol, Ethanol, and Isopropanol*. 67kx Magnification, scale bar 100 nm. Brightness enhanced by 20% to emphasize detail.

2.5 Conclusions

Though effective delivery vehicles for silencing, the bimodal size distribution of Comiskey's Dex-SiO_2-NPs hindered more thorough understanding of delivery vehicle construction and activity. Though size exclusion membranes were ineffective at separating the two populations of Comiskey's Dex-SiO_2-NPs, purification of the alkyl silicate starting materials yielded monodispersed size distributions. Building on the work of Stöber and others, concentrations of ammonium hydroxide, water, and TEOS were varied to produce Dex-SiO_2-NPs of varying diameter. The effects of different dextrans and cyclodextrins in NP synthesis were also examined. TEM was used to investigate Dex-SiO_2-NP formation at different time points before and after the addition of TEOS and APTES, revealing amorphous aggregates that grow into spherical nanoparticles. Lastly, DLS and TEM were used to probe the presence and behavior of aggregates in Dex-SiO_2-NP and SiO_2-NP reaction solutions. Methanol and isopropanol solutions produced Dex-SiO_2-NPs smaller than those prepared in ethanol, though further study is necessary to draw conclusions about the role of dextran in the reaction solution and, ultimately, the nanoparticle structure.

CHAPTER 3

UNRAVELING DEXTRAN'S ROLE IN DEX-SIO$_2$-NP MORPHOLOGY

3.1 Introduction

Dextran-containing silica nanoparticles (Dex-SiO$_2$-NPs) have shown promise as delivery vehicles for RNAi therapeutics. This, along with their unique appearance by TEM, prompted further study and characterization. This study was approached with the aim of determining the location of dextran in the NPs, which could ultimately result in understanding dextran's role in NP synthesis.

The complexity of Dex-SiO$_2$-NPs presents several characterization challenges. Therefore, a combination of chemical and physical characterization techniques are used herein. As insoluble structures, solution NMR of Dex-SiO$_2$-NPs is ineffective. CP-MAS ^{13}C-NMR, a method for measuring the magnetic resonances of materials in the solid state, is used herein to determine the organic components present in Dex-SiO$_2$-NPs. Thermogravimetric analysis is used to determine the water and organic content of NPs. Dextran was removed from Dex-SiO$_2$-NPs by Soxhlet extraction and calcination, followed by porosity and surface area analysis before and after dextran removal from NPs.

3.2 Characterization of Dex-SiO$_2$-NP Morphology

When compared to SiO$_2$-NPs prepared in the absence of dextran, the apparent core-shell structure exhibited by Dex-SiO$_2$-NP in TEM images (Figure 3.1) prompted further study. While the outer shells of Dex-SiO$_2$-NPs appear smooth like the nanoparticles prepared without dextran, the interior is consistently less dense.

Upon examination at higher magnification, several differences among the Dex-SiO$_2$-NPs are evident apart from size. The core and shell regions of Dex-SiO$_2$-200 (Figure 3.2, left) appear distinct from one another. Dex-SiO$_2$-200 NPs also have a smooth center region, in contrast with Dex-SiO$_2$-250 and Dex-SiO$_2$-350 NPs. A gradual transition from the outer shell to the NP center,

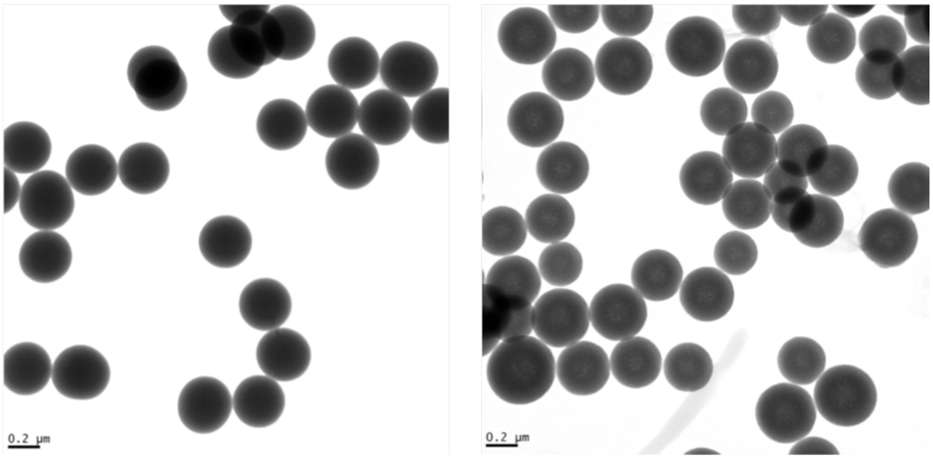

Figure 3.1: *TEM Micrograph of SiO_2-NPs and Dex-SiO_2-NPs*. SiO_2-NPs (left) and Dex-SiO_2-250 NPs (right), exhibiting less dense centers. 27kx magnification, Scale bar 0.2 μm. Brightness enhanced by 20% to emphasize detail.

along with fine, grainy center details set Dex-SiO_2-350 NPs apart (Figure 3.2, right). Dex-SiO_2-250 NPs fall between Dex-SiO_2-200 and Dex-SiO_2-350 NPs in both size and appearance. Distinct center and shell regions resemble Dex-SiO_2-200 NPs, while the grainy center (Figure 3.2, center) is akin to that of Dex-SiO_2-350 NPs.

Having spatially defined the area via scanning transmission electron microscopy, a series of successive EDS spectra build the profile observed in Figure 3.3. The sample area of a Dex-SiO_2-350 nanoparticle is shown on the left side of Figure 3.3, with the white line indicating the area scanned. The elemental profile (Figure 3.3, right) of silicon and oxygen were examined along this line. The y-axis presents the counts of x-rays of the specified energy detected, and is therefore indicative of elemental abundance. The low electron density of carbon (K_α = 0.277 compared to 1.739 (Si) and 0.525 (O)), as well as the use of microscopy grids containing carbon films does not allow for reliable measurement of the carbon content within the sample. Another limitation of the EDS method used here is its qualitative nature. Nevertheless, the results obtained by EDS confirm that Dex-SiO_2-NPs decrease in density of SiO_2 toward the center.

The sizes of the central cavities visible by TEM in Dex-SiO_2-NPs range from 10 - 100 nm (Figure 3.2), and is dependent on the type of Dex-SiO_2-NP being analyzed. Dex-SiO_2-350 NPs,

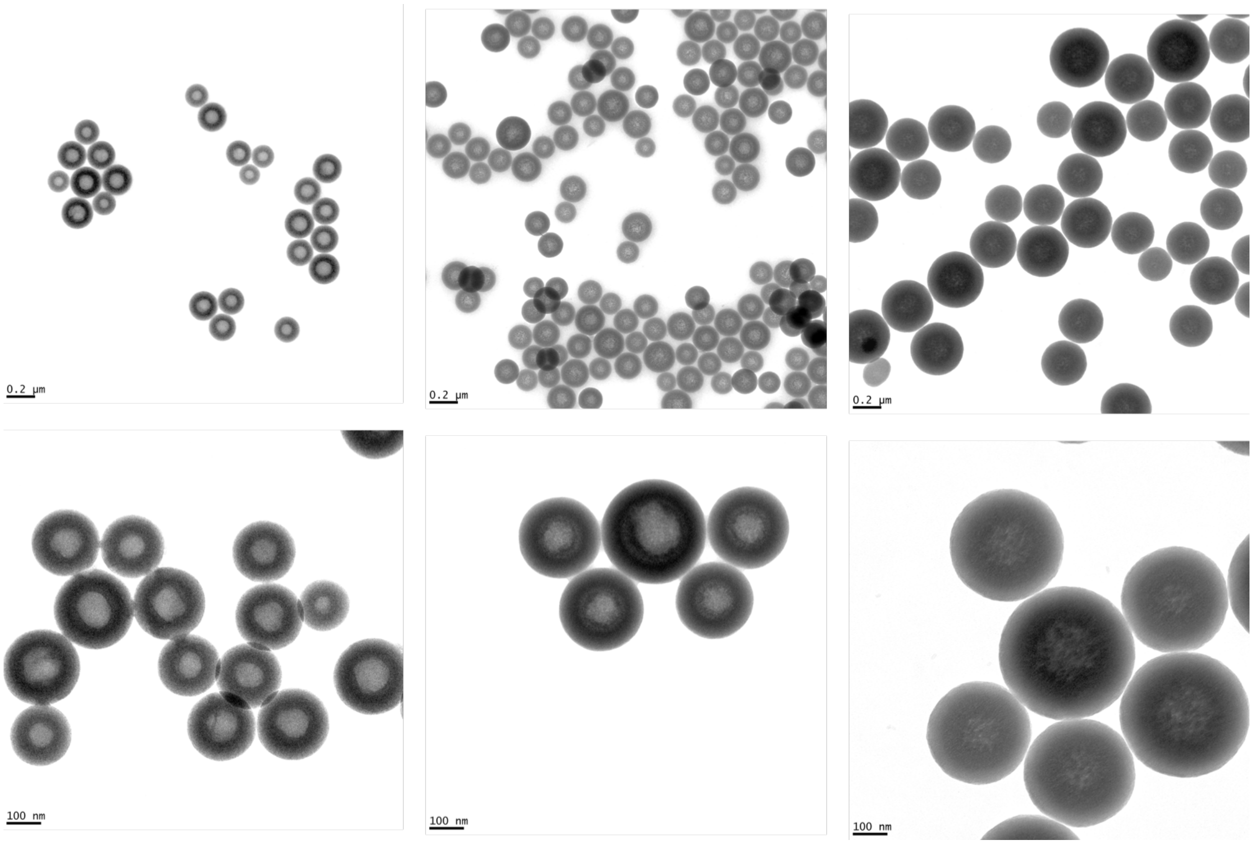

Figure 3.2: *TEM Micrographs of Dex-SiO_2-NPs*. Dex-SiO_2-200 (left), Dex-SiO_2-250 (center), and Dex-SiO_2-350 (right) at 27kx magnification, scale bar 0.2 μm (top) and 67kx magnification, scale bar 100 nm (bottom). Brightness enhanced by 20% to emphasize detail.

though larger than the 200 and 250 series, generally has smaller cavities. Since the cavernous centers are the most distinguishable features of Dex-SiO_2-NPs and SiO_2-NPs, it was hypothesized that the central cavity may be composed of dextran. Diameters of the hollow centers visible by TEM were measured and compared with the hydrodynamic diameter of dextran dissolved in water as measured by DLS. Three different size domains were evident by DLS (Figure 3.4). The most narrow peak was centered at 10 nm, followed by a less intense, broader peak at 200 nm, and the least intense peak at 5000 nm. The radius of gyration of a 9-11 kDa unit of dextran has been determined to exist between 10 - 15 nm,[108–110] larger than the diameter of a 10kDa protein (approximately 3 nm).[111] The less precise folding of dextran, as well as its branched structure may contribute to its greater hydrodynamic diameter. The DLS results represent different dextran aggregates which

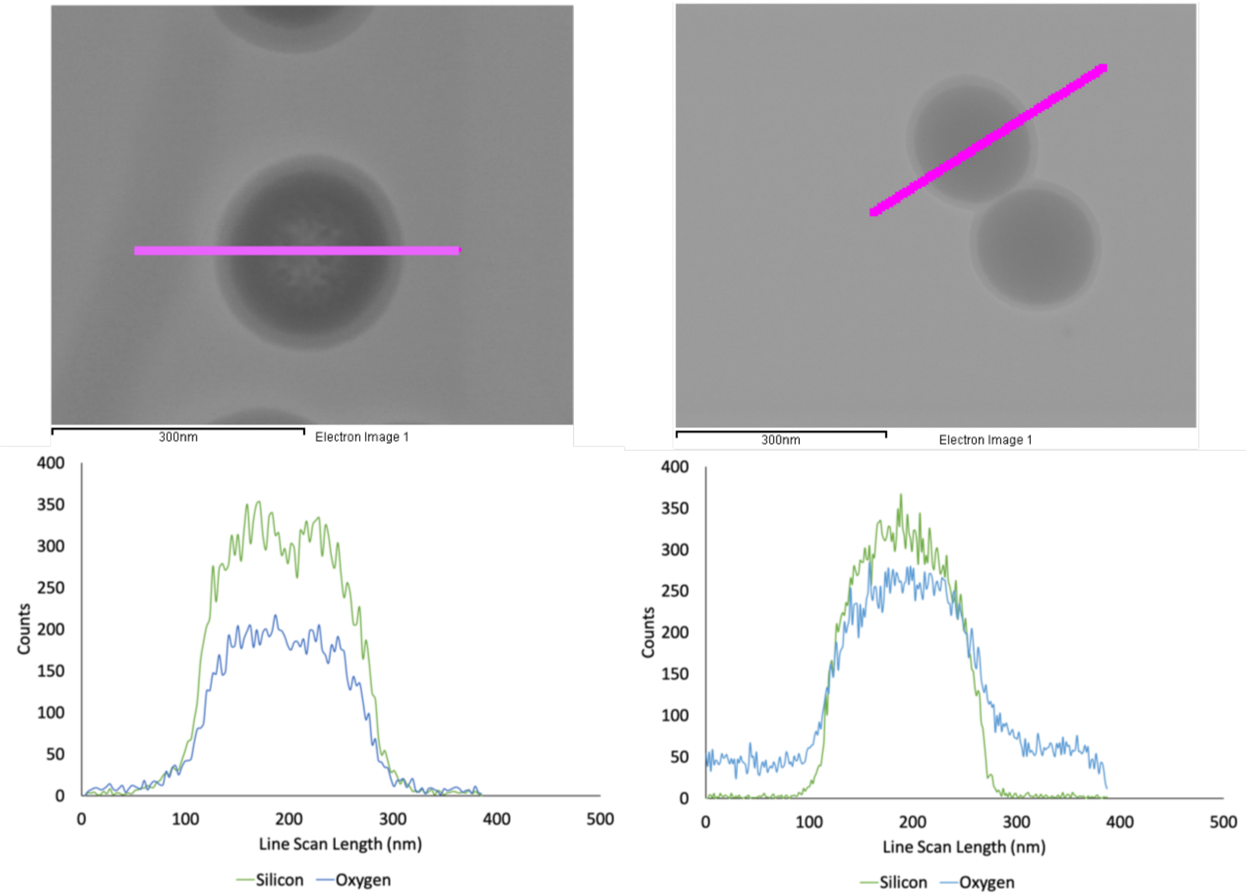

Figure 3.3: *STEM Micrographs and EDS Line Scan of Dex-SiO_2 and SiO_2 Nanoparticles*. S-TEM micrographs of Dex-SiO_2-NPs (left) and SiO_2-NPs (right), with area scanned for EDS analysis indicated by fuschia line (top), and silicon and oxygen elemental abundance profile along indicated area (bottom). Scale bar 300 nm. Y-axis indicates abundance as measured by X-ray counts.

are solubilized in water to differing degrees and ranging in diameter. Dissolving dextran in water and then stirring in ethanol, simulating synthesis conditions, revealed aggregates with diameters consistent with those observed within Dex-SiO_2-NP cavities (Figure 3.5). These results indicate that dextran aggregates may be templates around which the SiO_2 shell forms.

Microscopy and EDS have elucidated the SiO_2 component of the various Dex-SiO_2-NPs, as well as structural variations from SiO_2-NPs synthesized without dextran. It can be concluded from these results that the morphological differences between Dex-SiO_2-NPs and SiO_2-NPs result from the use of dextran during synthesis, though its presence in the final NP structure cannot be established from the microscopy or EDS results shown here.

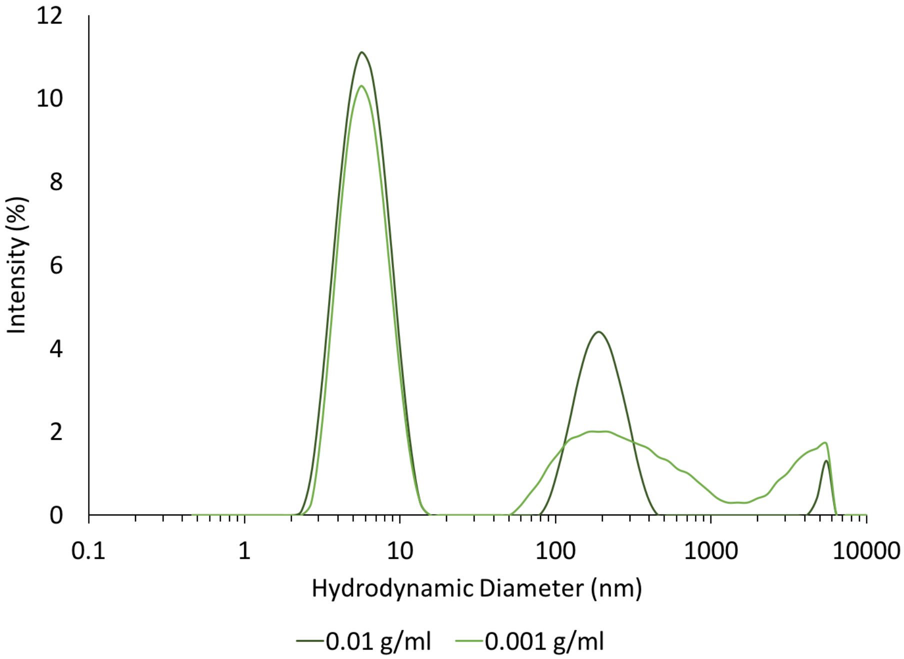

Figure 3.4: *Hydrodynamic Diameter of Dextran in Water.* Distribution of Hydrodynamic Diameters of 9-11 kDa dextran dissolved in MilliQ Water at 0.01 g/mL and 0.001 g/mL obtained using Dynamic Light Scattering.

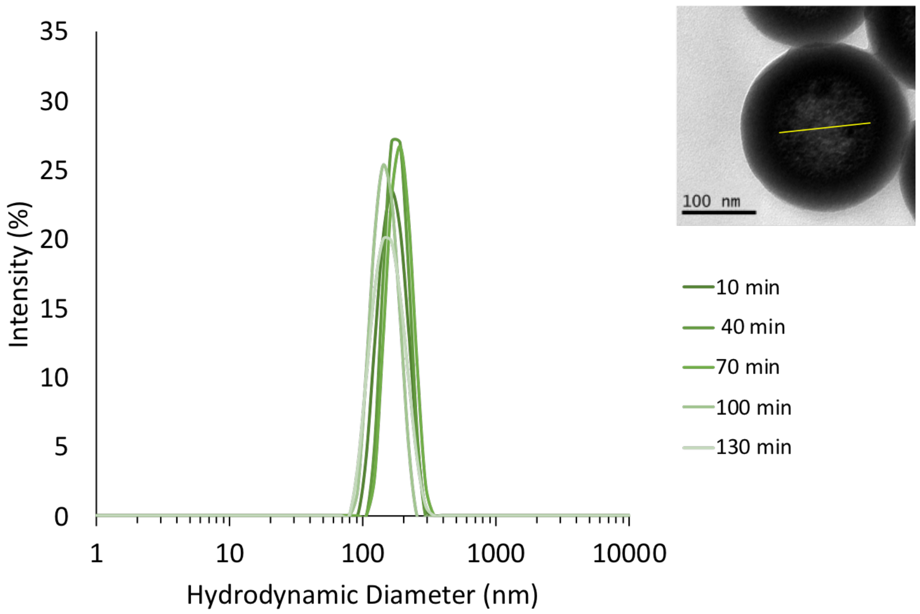

Figure 3.5: *Hydrodynamic Diameter of Dextran Aggregates in Ethanol.* Distribution of Hydrodynamic Diameters of at 0.01 g/mL 9-11 kDa dextran dissolved in MilliQ water and stirred in ethanol for the indicated time obtained using Dynamic Light Scattering.

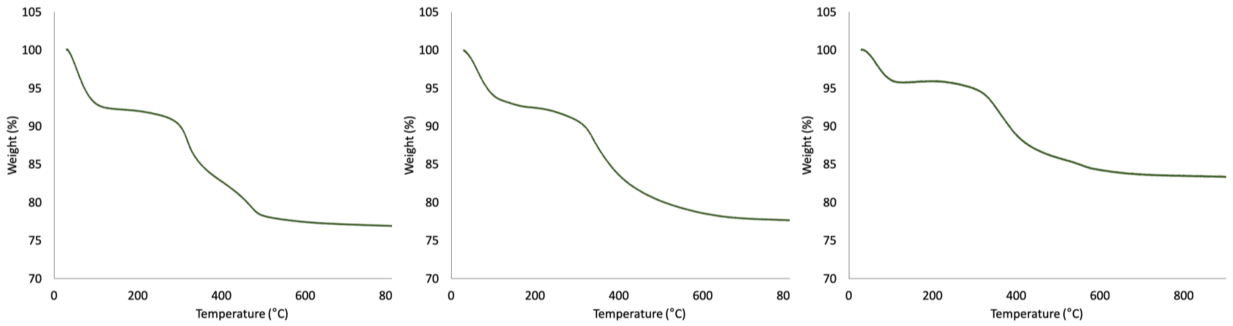

Figure 3.6: *TGA Profile of Dex-SiO_2-NPs.* TGA of Dex-SiO_2-200 (left), Dex-SiO_2-250 (center), and Dex-SiO_2-350 (right).

Table 3.1: *Percent Weight Lost of Dex-SiO_2-NPs, SiO_2-NPs, and Dextran by Thermogravimetric Analysis.*

NPs	25 - 100 °C	100-800 °C	25 - 800 °C
Dex-SiO_2-200	7.09	15.98	23.08
Dex-SiO_2-250	5.95	16.40	22.34
Dex-SiO_2-350	3.94	12.59	16.53
SiO_2-NPs	9.30	8.30	17.6
Dextran	8.70	89.06	97.76

3.3 Verifying Incorporation of Dextran into Dex-SiO_2-NPs

The high temperatures used in the thermogravimetric analysis of Dex-SiO_2-NPs allowed for removal and determination of percent incorporation of dextran within NPs. An initial loss from 25 °C to 100 °C was observed for all Dex-SiO_2-NPs, due to loss of water from within the nanoparticles (Figure 3.6, Table 3.1). Dex-SiO_2-200 NPs lost 7% of its weight to water, while Dex-SiO_2-250 NPs lost approximately 6%, and Dex-SiO_2-350 NPs lost 4%. Silica nanoparticles are known to be hygroscopic, therefore the initial loss of water is not surprising. SiO_2 NPs lost 9.3% of mass due to water, while dextran itself contains 8.7% of water by weight (Figure 3.7, Table 3.1).

The second loss begins at 300 °C and plateaus at 600 °C. Consistent with observations of pure dextran (Figure 3.7), this loss represents the loss of dextran from NPs. Accounting for the loss of water, Dex-SiO_2-200 NPs lost 16% due to dextran. Dex-SiO_2-250 NPs lost 16%, and Dex-SiO_2-350 NPs lost approximately 13%. The TGA of Dex-SiO_2-200 NPs exhibits a stepwise loss of weight at 500 °C, also observed in the TGA of dextran alone (Figure 3.7), and attributed

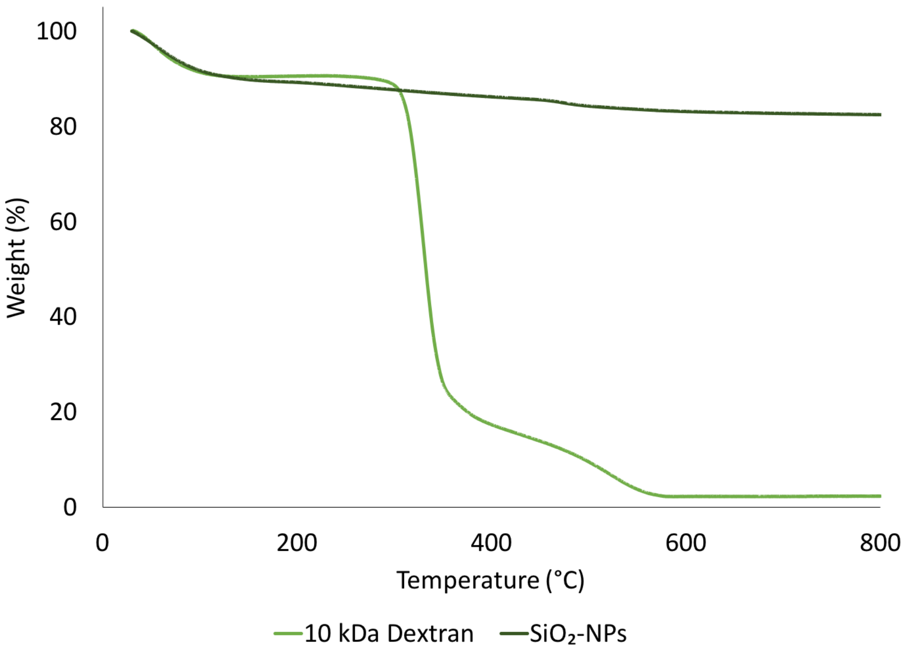

Figure 3.7: *TGA Profile of Dextran and SiO_2 NPs.* TGA of 9-11 kDa Dextran and SiO_2 NPs synthesized without dextran.

to complex decomposition processes of dextran. If all dextran included in the reaction mixture is incorporated into nanoparticles, it would be 24% of the weight of the nanoparticles. Considering the moisture present in dextran and silica, loss of 16 - 23% of NP weight by TGA indicates that nearly all dextran included in synthesis is incorporated into nanoparticles. After loss of water, SiO_2 NPs lost only 83% of mass, which is attributed to residual ethanol. Dextran itself loses nearly all of it's remaining mass, an additional 89% after loss of water (Figure 3.7, Table 3.1). Interestingly, NPs with different diameters, produced by variation of ethanol and water, exhibit variable dextran incorporation. There is also a correlation between decreased water content with increasing nanoparticle diameter. This may be due to the difference in dextran content across the different sizes of nanoparticles. This system uses lyophilized dextran dissolved separately in water, therefore it is reasonable to conclude that the correlation is due to different dextran content.

The hollow appearance of Dex-SiO_2-NPs varies significantly from the more solid-looking products of the analogous reaction produced in the absence of dextran (Figure 3.1). These ob-

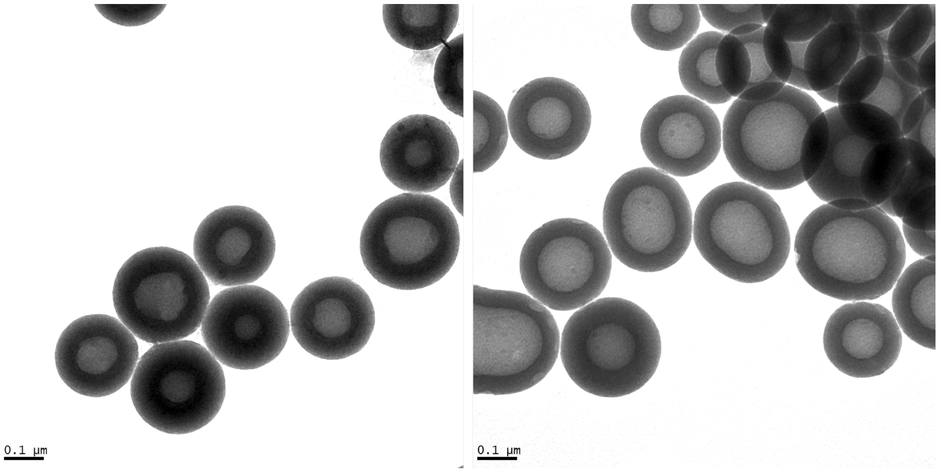

Figure 3.8: *TEM Micrographs of Dex-SiO_2-200 Nanoparticles after TGA*. Dex-SiO_2-200 before (left) and after (right) TGA. Decreased density in the nanoparticle shell post-TGA suggests fracturing of SiO_2 surface with thermal removal of dextran. 67kx magnification, scale bar 0.1 μm. Brightness enhanced by 20% to emphasize detail.

servations are consistent with other reports in the literature of hollow SiO_2-NPs prepared using templates.[73, 112] In order to confirm the presence of dextran in Dex-SiO_2-NPs, solid state CP-MAS ^{13}C-NMR was performed. The resulting NMR spectra shows a singlet at 97.8 ppm corresponding to C1 of dextran, and a broad singlet centered at 71.5 ppm corresponds to C2-C6 (Figure 3.9). These resonances are consistent with the literature and solution NMR of dextran, confirming that dextran is incorporated in the Dex-SiO_2-NPs. The low intensity resonances at 30 and 40 ppm result from the presence of adamantane, used as a reference, while the resonance at 8 ppm ethoxy groups originating from the TEOS starting material and/or the ethanol used as solvent.

Solid state NMR results verify the presence of dextran in the Dex-SiO_2-NPs. TEM and EDS line scan results show monodispersed Dex-SiO_2-NPs bearing a dense shell and less dense core. Nevertheless, neither method provides direct evidence of the location of dextran on the surface or within the Dex-SiO_2-NPs. Attempts to identify dextran's location within Dex-SiO_2-NPs via chemical derivatization were unsuccessful. The inability to quantify dextran through chemical derivatization may provide an indication of the accessibility of dextran from the NP surface.

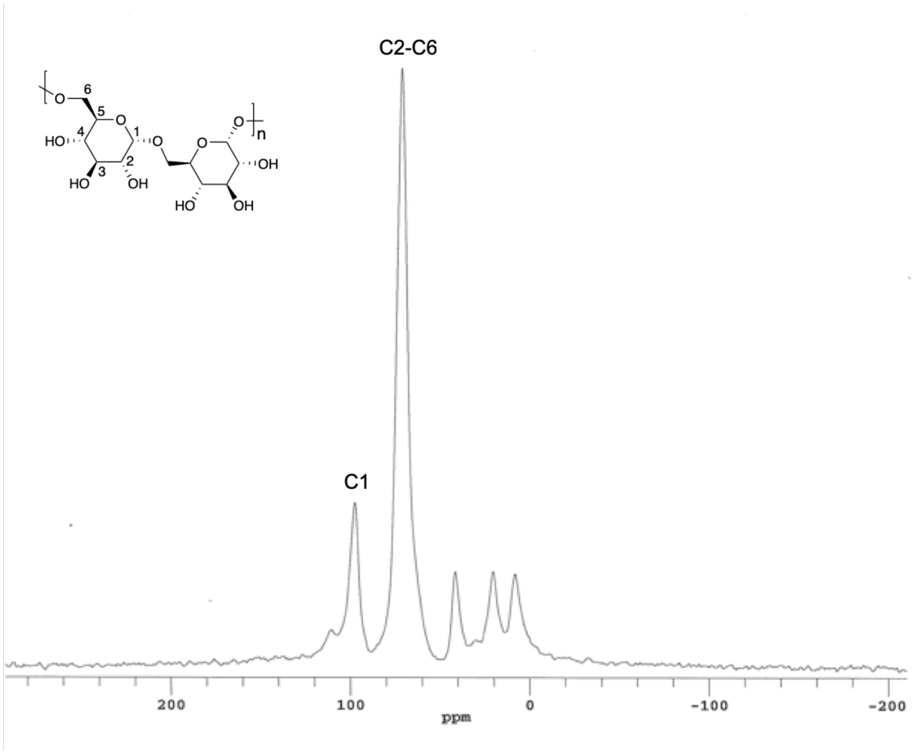

Figure 3.9: *Solid State CP-MAS ^{13}C-NMR of Dex-SiO$_2$-350 Nanoparticles*. Dextran appears in solid state CP-MAS ^{13}C-NMR of Dex-SiO$_2$-NPs, confirming its presence in nanoparticles after synthesis and purification.

3.4 Removal of Dextran and Post-Mortem Porosity Analysis

While TEM, EDS, TGA, and CP-MAS ^{13}C-NMR have provided valuable information confirming the amount and presence of dextran, as well as variation of silica content across NPs, the location of dextran within Dex-SiO$_2$-NPs has not been informed by these means. The present approach removes dextran from Dex-SiO$_2$-NPs, which are then subjected to surface area and porosity analysis by gas adsorption. This so-called "post-mortem" analysis, when compared with gas adsorption results from intact Dex-SiO$_2$-NPs, can reveal the volume vacated by dextran, as well as its location within the NPs.

Soxhlet extraction was used to remove dextran from Dex-SiO$_2$-NPs using water, followed by characterization by TEM for observation of structural changes, while TGA reveals how much dextran is removed by the extraction process. Soxhlet extraction was performed using water as

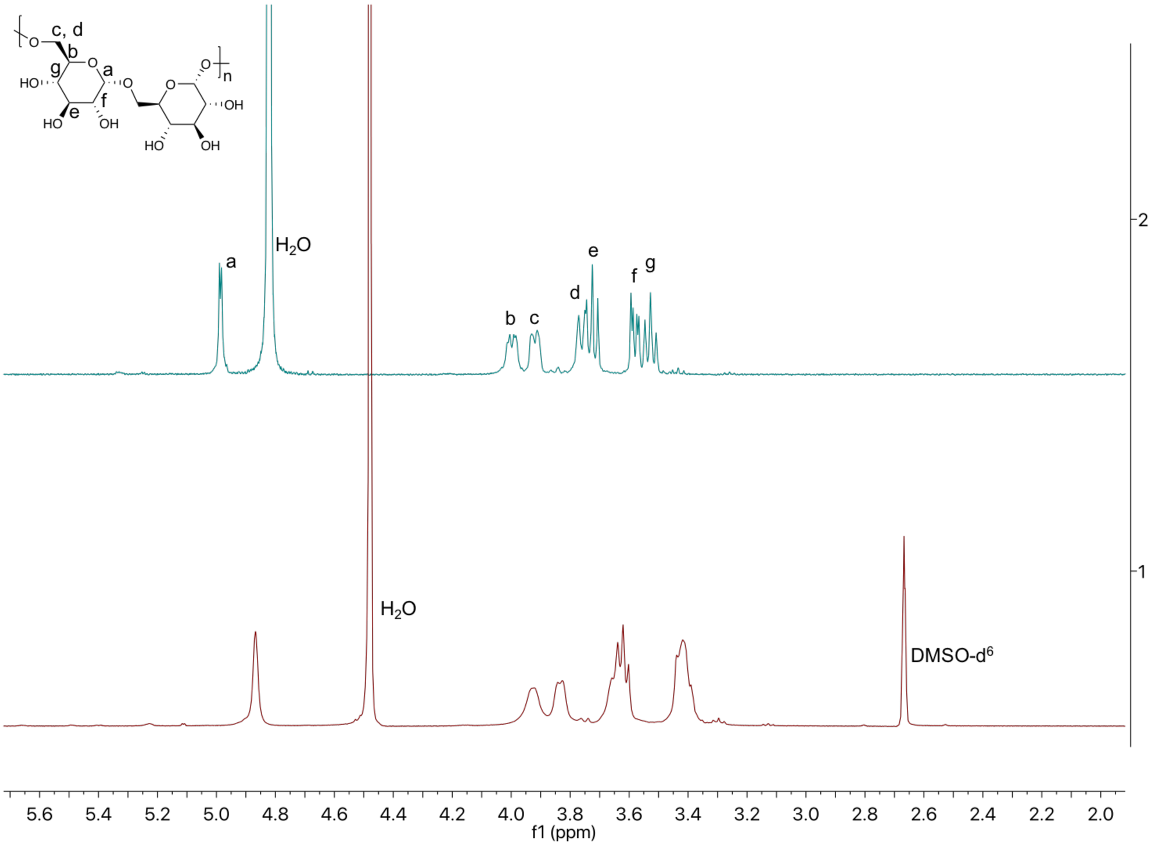

Figure 3.10: *500 MHz ^{1}H-NMR of Dextran.* 10 kDa Dextran in D_2O (top), and recovered from Dex-SiO_2-NPs by Soxhlet extraction in D_2O/DMSO-d_6 (bottom).

a solvent to enhance the solubility of dextran. Nanoparticles were recovered from the cellulose thimble and analyzed using TEM and TGA. The filtrate was lyophilized to obtain a white solid, confirmed as dextran via ^{1}H-NMR (Figure 3.10).

The electron density of carbon is too low to be detected by TEM, thus it is interesting that structural changes arising from Soxhlet extraction are observed by TEM (Figure 3.11, compared to Figure 3.2), indicating that the silica structure itself is compromised. Overall, the surfaces of Dex-SiO_2-NPs become more rough after Soxhlet extraction and the centers appear more hollowed. Dex-SiO_2-200 NPs have smaller amorphous, granular pieces within the NP population, which may be pieces of silica that were removed from the NPs along with dextran. Dex-SiO_2-250 NPs bear a significantly less dense center, a more grainy appearance, and a less gradual progression from the

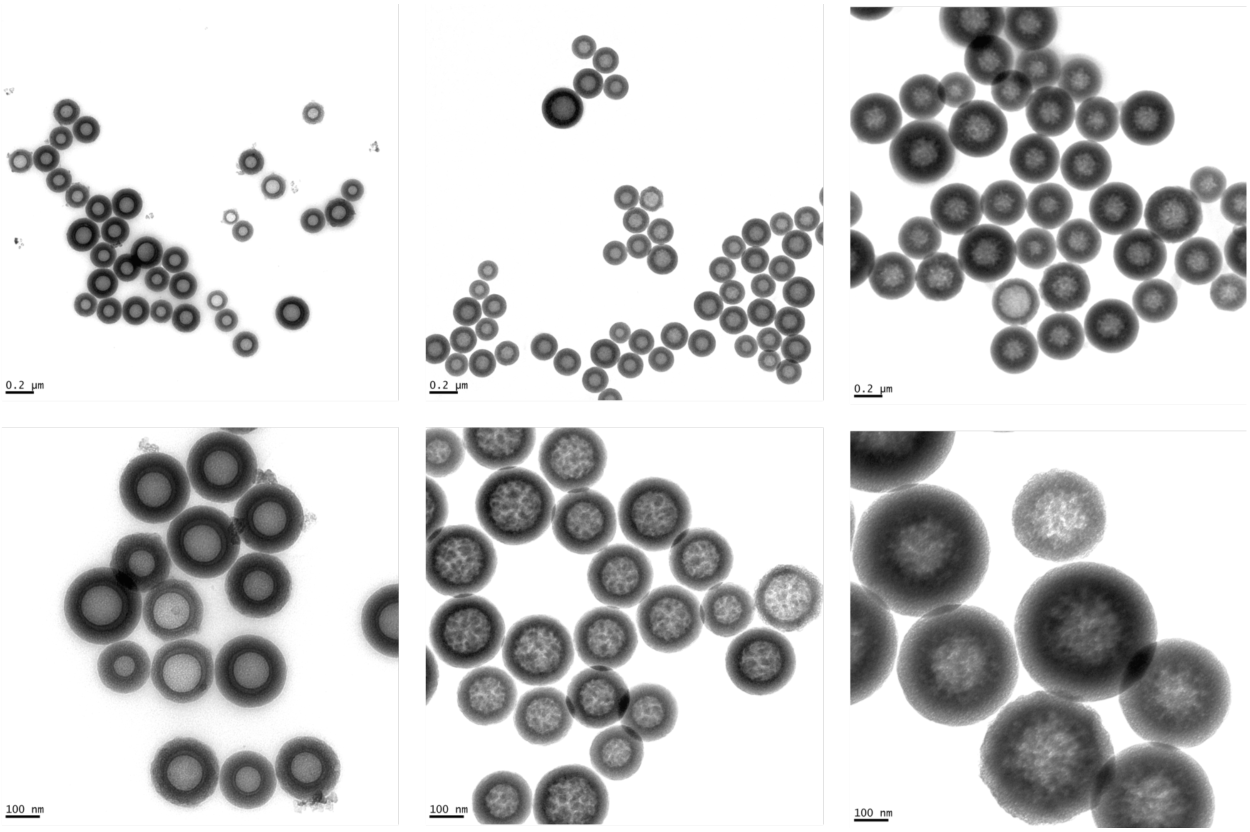

Figure 3.11: *TEM Micrographs of Dex-SiO$_2$-NPs After Soxhlet Extraction.* Dex-SiO$_2$-200 (left), Dex-SiO$_2$-250 (center), and Dex-SiO$_2$-350 (right) at 27kx magnification, scale bar 0.2 μm (top) and 67kx magnification, scale bar 100 nm (bottom). Brightness enhanced by 20% to emphasize detail.

center to the core. The most apparent change to Dex-SiO$_2$-350 is the more grainy center and rough exterior shell.

Another noticeable feature of the Dex-SiO$_2$-NPs following Soxhlet extraction of dextran is the variation in appearance of different nanoparticles within one sample. While many appear more hollow, other nanoparticles retain a solid appearance, with little transmission. This may be attributed to varying rates of condensation and hydrolysis during nanoparticle synthesis, potentially resulting in non-uniform incorporation of dextran. VanBlaaderen and co-workers noted that decreased rates of hydrolysis results in persistence of ethoxy groups within SiO$_2$-NPs.[?] Since the ethoxy group is larger than a hydroxyl group, a less dense silica network arises from such conditions. The overall decrease in density at the center of the particles after extraction may be explained by small amounts

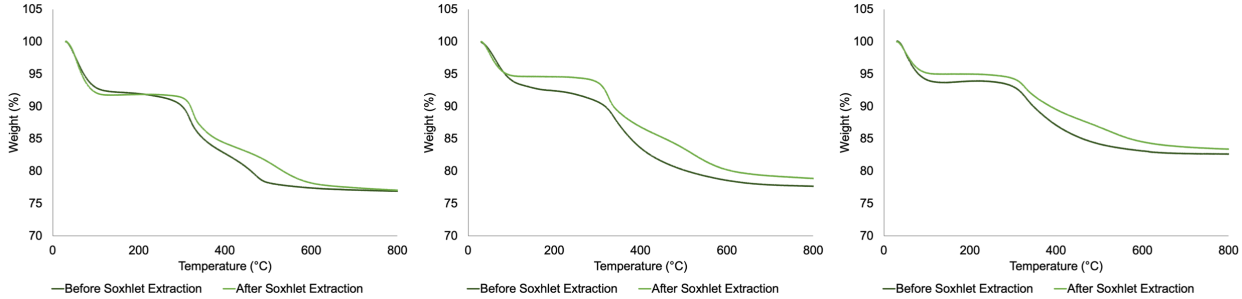

Figure 3.12: *TGA Profile of Dex-SiO$_2$-NPs Before and After Soxhlet Extraction.* Dex-SiO$_2$-200 (left), Dex-SiO$_2$-250 (center), and Dex-SiO$_2$-350 (right)

Table 3.2: *Percent Weight Lost of Dex-SiO$_2$-NPs after Soxhlet Extraction by Thermogravimetric Analysis.*

NPs	25 - 100 °C	100-800 °C	25 - 800 °C
Dex-SiO$_2$-200	7.86	15.07	22.93
Dex-SiO$_2$-250	5.23	15.09	21.13
Dex-SiO$_2$-350	4.83	11.74	16.57

of silica that are fused to dextran being removed during the extraction.

TGA revealed a minimal loss of dextran by Soxhlet extraction (Figure 3.12, Table 3.2). The different Dex-SiO$_2$-NPs exhibited decreasing water content with increasing molecular weight, consistent with data collected on NPs before extraction (Table 3.1). After Soxhlet extraction, the amount of dextran extracted from Dex-SiO$_2$-200 and Dex-SiO$_2$-250 were both approximately 15%, while Dex-SiO$_2$-350 NPs lost 11.74%. Compared with the amount of dextran initially incorporated into Dex-SiO$_2$-NPs, the amount of dextran extracted by Soxhlet ranged from 0.85% - 1.31%. Incomplete removal of dextran by Soxhlet extraction may be due to its intimate incorporation within the molecular structure of SiO$_2$ nanoparticles. Considering the low efficiency of dextran extraction, the change in appearance of Dex-SiO$_2$-NPs after Soxhlet extraction is more likely due to repeated rinsing of water eroding the silica structure than due to removal of dextran.

The low dextran removal efficiency of Soxhlet extraction led to exploration of different methods of dextran removal. Since removal of organic components from ceramic structures has been accomplished via calcination at temperatures ranging from 500°C - 700°C, we proceeded with calcination as the means of removing dextran.[113] TEM and TGA were used to determine the

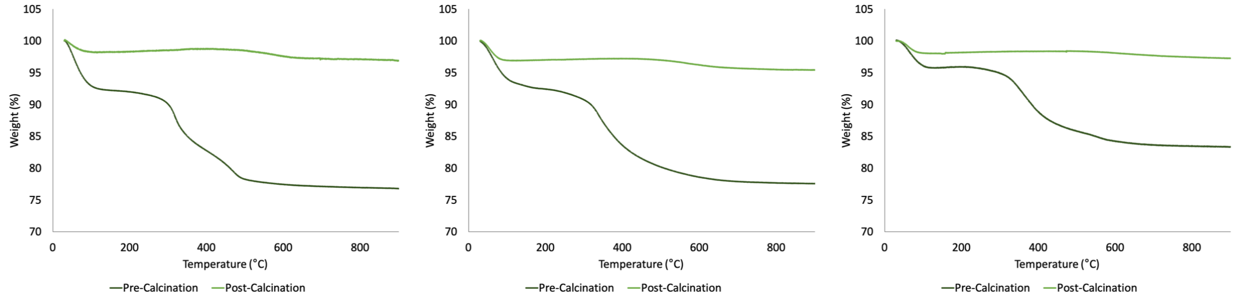

Figure 3.13: *TGA Profile of Dex-SiO$_2$-NPS Before and After Calcination*. Dex-SiO$_2$-200 before (left) and after (right) TGA.

Table 3.3: *Percent Weight Lost of Dex-SiO$_2$-NPs after Calcination by Thermogravimetric Analysis*.

NPs	25 - 100 °C	100-800 °C	25 - 800 °C
Dex-SiO$_2$-200	1.80	1.06	2.86
Dex-SiO$_2$-250	3.06	1.43	4.50
Dex-SiO$_2$-350	1.88	0.66	2.54

efficacy of dextran removal and assess the physical characteristics of Dex-SiO$_2$-NPs. TGA of Dex-SiO$_2$-NPs after calcination at 350°C over four days evidenced a minor loss of water, and small loss of organic content (<2%) indicating that the majority of dextran was removed during the heating process (Figure 3.13, Table 3.3). Microscopy revealed that, unlike Soxhlet extraction, calcination did not compromise the structure of Dex-SiO$_2$-NPs (Figure 3.14). No significant erosion of the silica surface was evident, and the size distributions did not vary as a result of calcination.

With successful dextran removal by calcination, nitrogen adsorption-desorption analysis was performed to analyze changes to the surface area and porosity of Dex-SiO$_2$-NPs arising in the absence dextran. The obtained Dex-SiO$_2$-NPs isotherms are shown in Figure 3.15. The three isotherms in the top row represent Dex-SiO$_2$-200, Dex-SiO$_2$-250, and Dex-SiO$_2$-350 before calcination. The presence of a plateau classifies these as Type I, according to IUPAC classification.[91] Type I isotherms indicate early completion of monolayer adsorption and microporosity. The increase in adsorption nearing a partial pressure of one bears similartities to the macroporous region of the Type II isotherm. The presence of characteristics suggests that both micro- and macropores exist within Dex-SiO$_2$-NPs. Type II character is present in all isotherms obtained, and may rep-

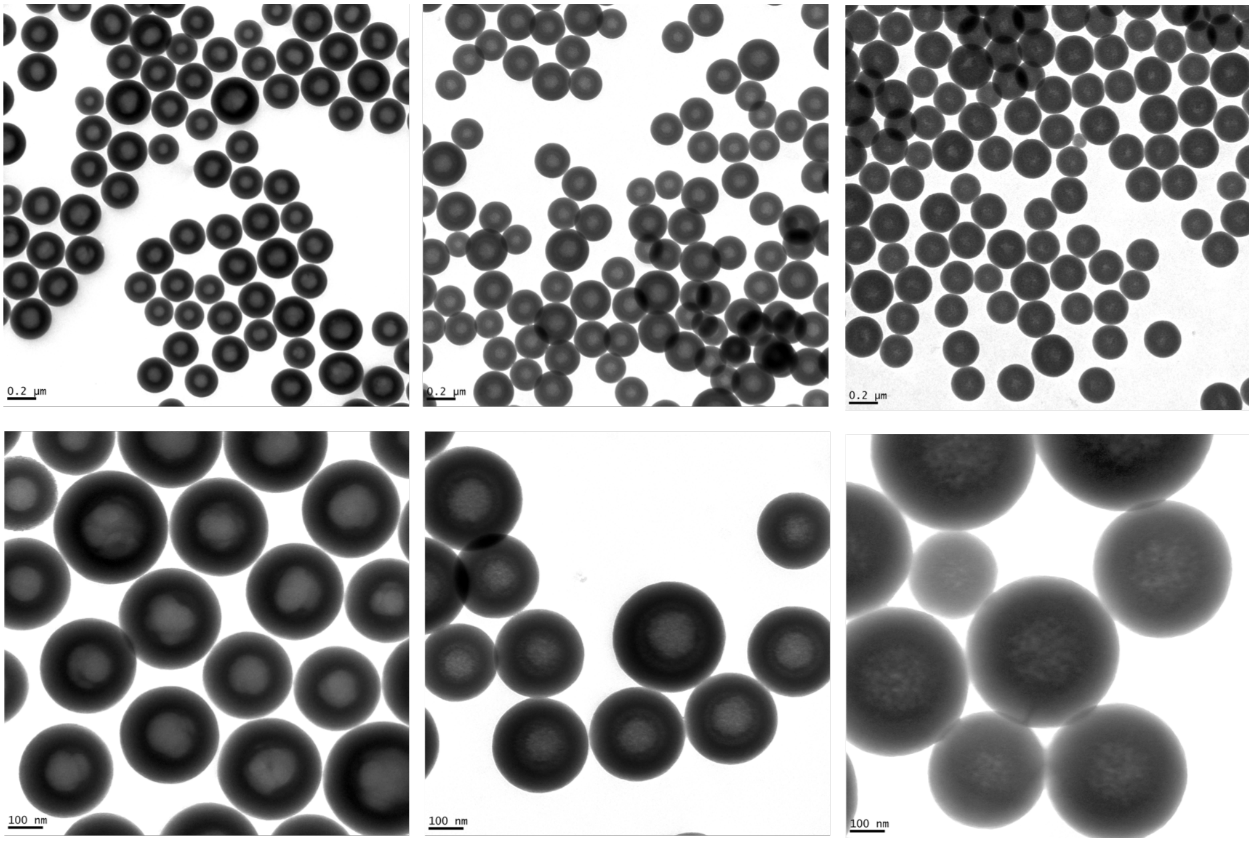

Figure 3.14: *TEM Micrographs of Dex-SiO_2-NPs After Calcination*. TGA of Dex-SiO_2-200 NPs (left), Dex-SiO_2-250 NPs (center), and Dex-SiO_2-350 NPs (right) at 27kx magnification, scale bar 0.2 μm (top) and 67kx magnification, scale bar 100 nm (bottom). Brightness enhanced by 20% to emphasize detail.

resent the hollow centers within Dex-SiO_2-NPs and/or the interstitial spaces between NPs in the sample. After calcination, the isotherm shapes vary more significantly among the different types of Dex-SiO_2-NPs. Calcined Dex-SiO_2-350 NPs exhibit a Type IV isotherm, which is typical of mesoporous materials. The isotherm shapes of calcined Dex-SiO_2-200 and Dex-SiO_2-250 NPs do not differ much from those of the non-calcined NPs.

The significant hysteresis loop observed after calcination of Dex-SiO_2-350 NPs resembles H2(a) the most, indicating complex pore shapes. The steep desorption branch characteristic of H2(a) hysteresis loops are attributed to pore blocking in pore necks or cavitation-induced evaporation.[91] The hysteresis loops of Dex-SiO_2-200 and Dex-SiO_2-250 are more pronounced in isotherms obtained before calcination than after (Figure 3.15). Unlike Dex-SiO_2-350, the hysteresis

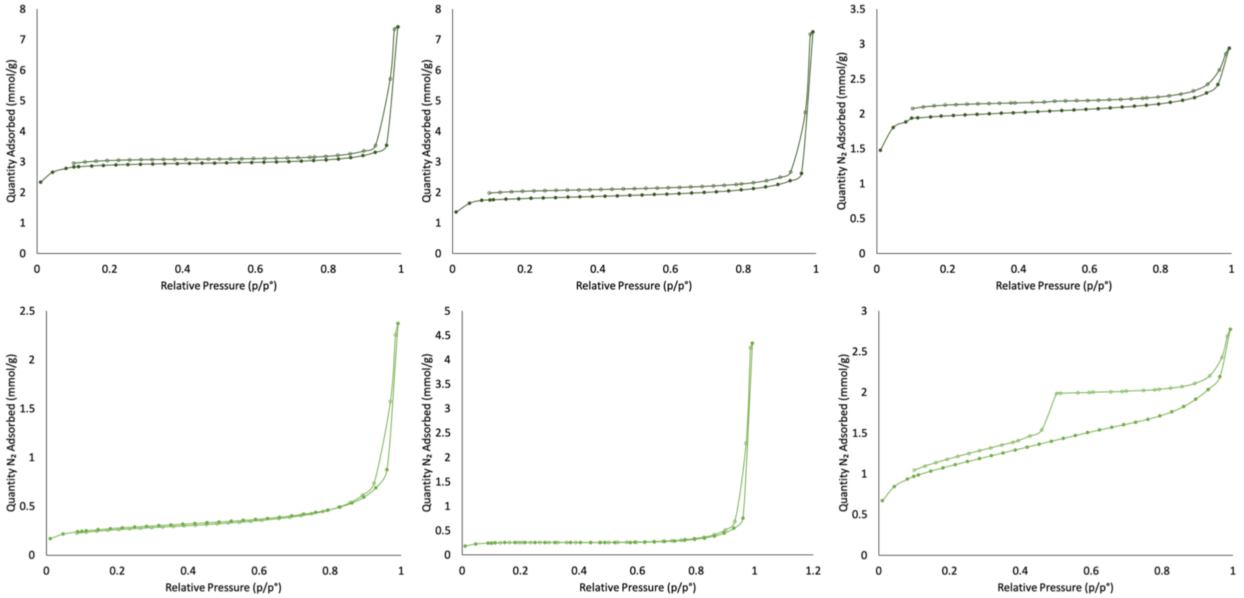

Figure 3.15: *Nitrogen Adsorption-Desorption Isotherms of Dex-SiO$_2$-NPs.* Adsorption (top) and desorption (bottom) isotherms of Dex-SiO$_2$-200 NPs (left), Dex-SiO$_2$-250 NPs (center), and Dex-SiO$_2$-350 NPs (right).

of the smaller NPs is more consistent with type H4. Signatures of H4 hysteresis loops include the Type I/II character of the adsorption branch and the lower limit of the desorption branch existing at the partial pressure where cavitation occurs.

Insights gained from isotherm shapes are illustrated by the differential pore volume distributions obtained via DFT (Figure 3.16, Figure 3.17, and Figure 3.18). Non-calcined NPs contain more micropores (< 2 nm) than mesopores (2 - 50 nm). Following calcination, a decrease in micropores is accompanied by an increase in mesopores (Table 3.4). It can be inferred from these results that the removal of dextran creates larger pores within the Dex-SiO$_2$-NPs and results in the loss of smaller pores. These observations are consistent with the behavior of organic templates and/or porogens, which are widely used to customize pore size and shape within materials, including SiO$_2$ NPs.[114] The presence of micropores and some mesopores before dextran removal suggests that, though its removal from the NPs results in larger pore formation, even with dextran intact Dex-SiO$_2$-NPs are porous.

Before calcination, the porosity of Dex-SiO$_2$-200 and Dex-SiO$_2$-250 NPs are consistent with

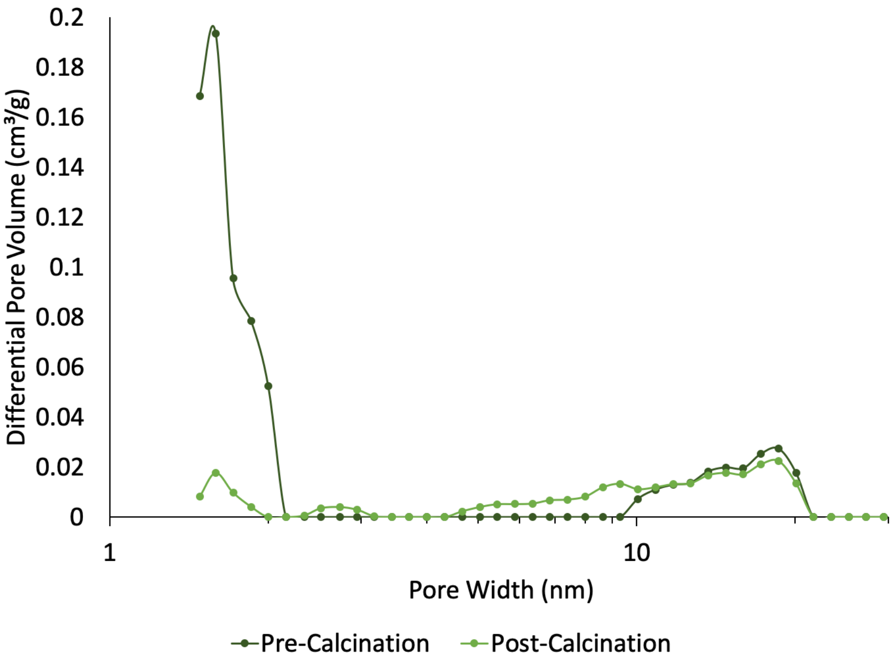

Figure 3.16: *Differential Pore Volume of Dex-SiO_2-200 NPs Before and After Calcination*. Differential Pore Volume of Dex-SiO_2-200 NPs before and after calcination.

Dex-SiO_2-350. Post-calcination, the microporosity of Dex-SiO_2-200 and Dex-SiO_2-350 decrease along with an increase in mesoporosity (Figure 3.16 and Figure 3.18), while Dex-SiO_2-250 loses microporosity but does not gain significant mesoporosity (Figure 3.17).

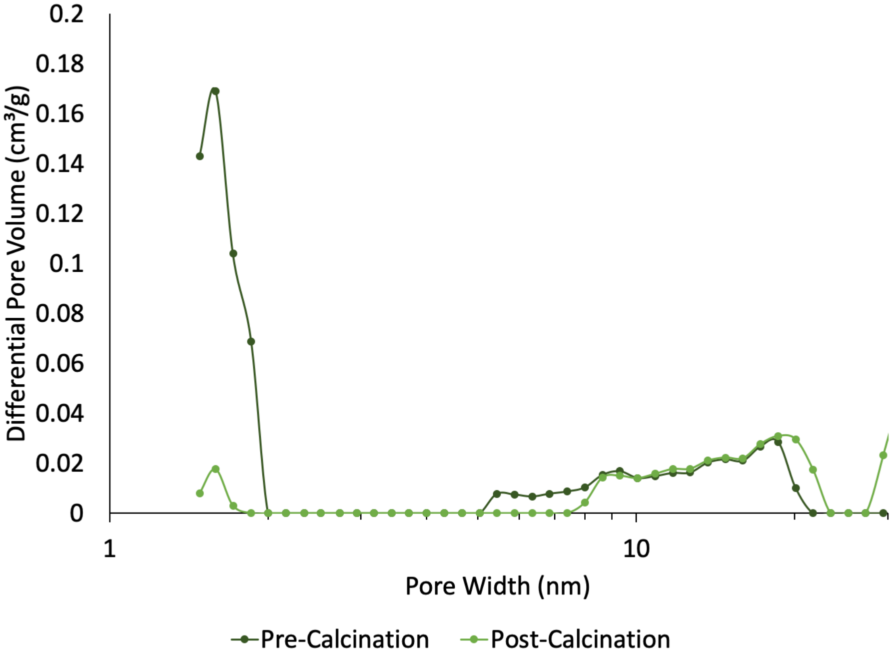

Figure 3.17: *Differential Pore Volume of Dex-SiO$_2$-250 NPs Before and After Calcination.* Differential Pore Volume of Dex-SiO$_2$-250 NPs before and after calcination.

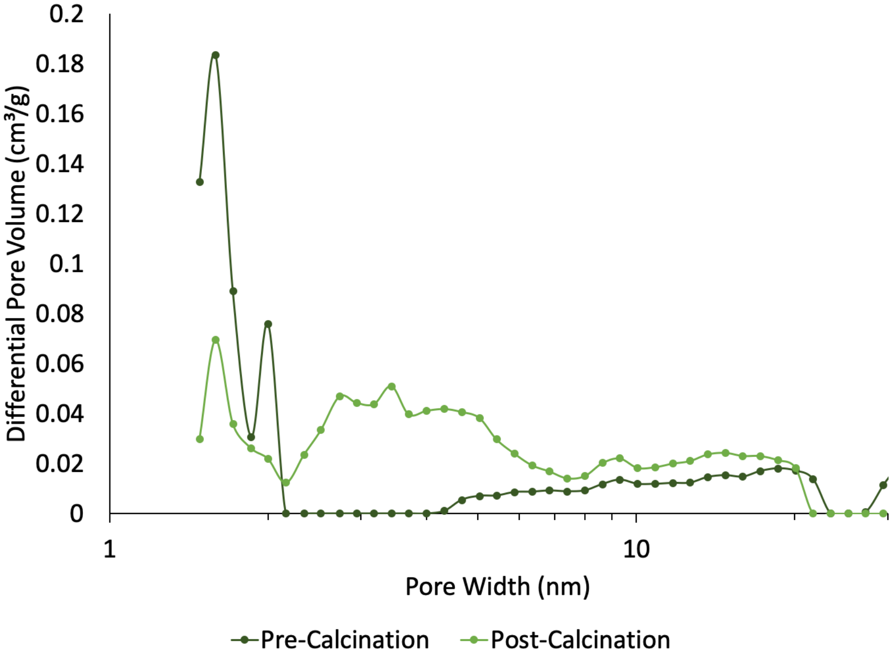

Figure 3.18: *Differential Pore Volume of Dex-SiO$_2$-350 NPs Before and After Calcination.* Differential Pore Volume of Dex-SiO$_2$-350 NPs before and after calcination.

Table 3.4: *Summary of Surface Area and Porosity of Dex-*SiO_2*-NPs Before and After Calcination.*

NPs	Heat Treatment	BET Surface Area (m^2/g)	1.5-2 nm Pore Volume (cm^3/g)	2-10 nm Pore Volume (cm^3/g)	10-25 nm Pore Volume (cm^3/g)
Dex-SiO_2-200	120 °C, 2h	183	0.019	0	0.005
Dex-SiO_2-200	300 °C, 96h	20	0.0013	0.003	0.005
Dex-SiO_2-250	120 °C, 2h	183	0.018	0.004	0.006
Dex-SiO_2-250	300 °C, 96h	14	0	0	0.005
Dex-SiO_2-350	120 °C, 2h	125	0.016	0.003	0.005
Dex-SiO_2-350	300 °C, 96h	80	0.006	0.021	0.007

Nitrogen adsorption data for Dex-SiO_2-NPs ranging from a partial pressure of 0 to 0.3 correlate well with the BET equation (Figure 3.19), with correlation coefficients > 98%. Dex-SiO_2-200 and Dex-SiO_2-250 NPs exhibit a large decrease in surface area after calcination from 183 cm^3/g to 20 cm^3/g (Dex-SiO_2-200) and 183 cm^3/g to 14 cm^3/g (Dex-SiO_2-250) (Table 3.4). Each variation of Dex-SiO_2-NPs lose surface area following calcination, though Dex-SiO_2-200 and Dex-SiO_2-250 lose more than Dex-SiO_2-350. This is hypothesized to arise as a result of the decreased structural integrity at the surface of Dex-SiO_2-NPs as the surface area to volume ratio increases. Here, the loss of structural integrity is manifest as pore collapse and/or nanoparticle fusion. Gu and co-workers and Li and co-workers made similar observations of low SiO_2-NP surface areas as a function of purification and heat treatment.[79, 98, 99, 115]

3.5 Conclusions

Dex-SiO_2-NPs present a challenge for typical chemical characterization techniques and have herein been studied using both chemical and physical techniques. TEM was used to study the physical differences of SiO_2-NPs and Dex-SiO_2-NPs, revealing hollow core-shell structures bearing variable gradients and diameters for NPs synthesized in the presence of dextran. Elemental details across a two dimensional plane of the NPs were obtained via S-TEM equipped with EDS capabilities, confirming that the increased light transmitted through the centers of NPs were due to a decrease in SiO_2. While carbonaceous materials cannot be detected by EDS, solid state CP-MAS ^{13}C-NMR provided spectral evidence of dextran incorporation into Dex-SiO_2-NPs. TGA revealed that

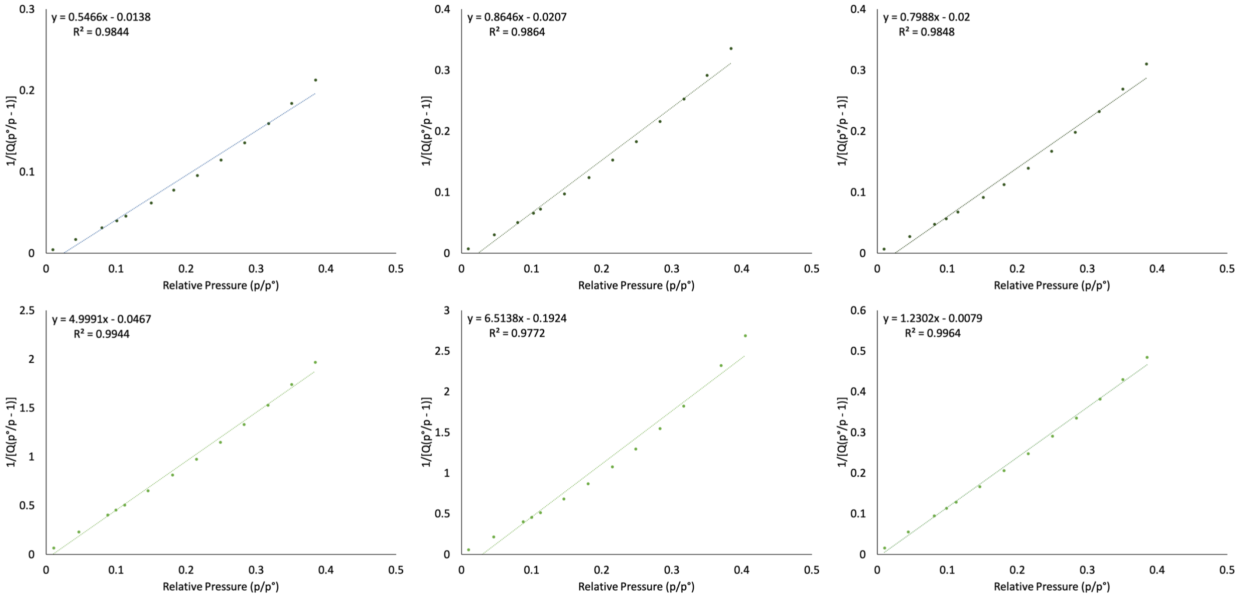

Figure 3.19: *BET Fit of Dex-SiO_2-NPs Before and After Calcination*. Brunauer, Emmett, and Teller Fit of Nitrogen Adsorption-Desorption Data for Dex-SiO_2-200 NPs (left), Dex-SiO_2-250 NPs (center), and Dex-SiO_2-350 NPs (right) before (top) and after (bottom) calcination.

5-7% of Dex-SiO_2-NP sample mass is due to water and 12-16% originates from dextran. Full incorporation of dextran into Dex-SiO_2-NPs would account for 24% of sample mass. Surface area and porosity measurements revealed that Dex-SiO_2-NPs contain both micro- and mesopores and have surface areas ranging from 183 cm^3/g for smaller NPs to 125 cm^3/g for larger NPs.

While Soxhlet extraction was an inefficient method for removing dextran, TEM images of NPs after extraction suggested that NPs within the same population may be heterogeneous in dextran incorporation. The different appearance of Dex-SiO_2-NPs by TEM after Soxhlet extraction has been attributed to erosion by continual extraction with water. Calcination was successfully implemented to remove dextran from Dex-SiO_2-NPs. Surface area and porosity analysis following calcination showed a decrease in surface area resulting from partial pore collapse and NP fusion. TEM micrographs provide no evidence indicating pore collapse or fusion of NPs after calcination, though this method is limited by the inability to observe details at the surface of Dex-SiO_2-NPs.

DLS evidence indicates that, when dissolved in MilliQ water at 25 °C, a range of hydrodynamic diameters of dextran and dextran aggregates exist. These data and other evidence in the literature

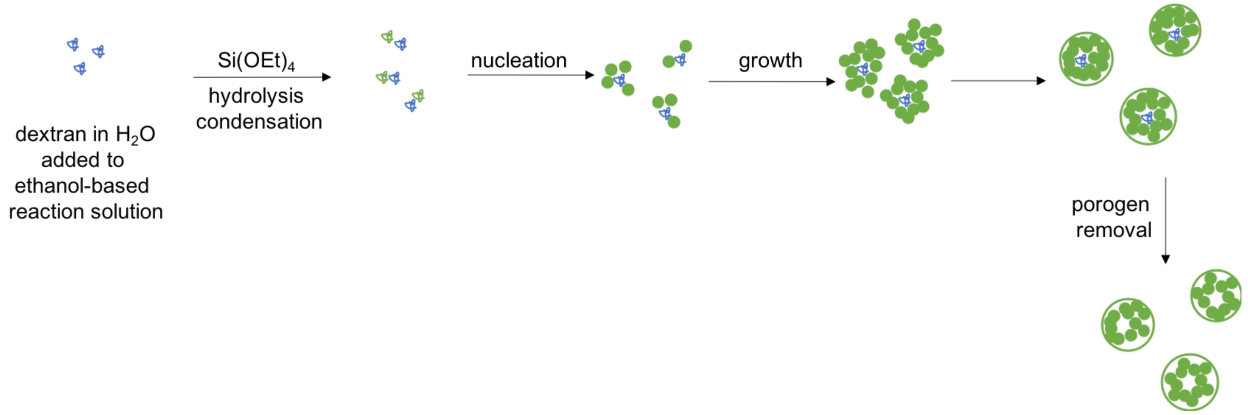

Figure 3.20: *Schematic Diagram of Dex-*SiO_2*-NPs Synthesis and Calcination.*

suggest that the increased concentration of water around these aggregates results in higher rates of TEOS hydrolysis and condensation than elsewhere in the reaction mixture, resulting in the observed hollow structures. BET indicates the presence of micropores (< 2 nm) and mesopores (2 - 50 nm). The change in isotherm shape and DFT pore volume analysis indicate that calcination results in a decrease in microporosity and an increase in mesoporosity for Dex-SiO_2-200 and Dex-SiO_2-350 NPs. Based on these results, it can be concluded that dextran exists primarily throughout the silica shell and acts as a porogen in the synthetic process (Figure 3.20). The range of pore sizes apparent by pore size analysis and TEM are hypothesized to originate from dextran and larger aggregates of dextran present in the synthesis solution.

CHAPTER 4

DESIGN OF AMINE-COATED DEXTRAN-INCORPORATED SILICA NANOPARTICLES AS SIRNA DELIVERY VEHICLES

4.1 Introduction

Taking advantage of the RNA interference (RNAi) pathway for therapeutic gain requires the use of a delivery vehicle in order to protect siRNA, transport it to the target location, and release it for use in the RNAi pathway. Numerous variations of delivery vehicles have been developed to date. Here, carbohydrate-silica nanoparticles with exposed amines are studied in order to understand the role of diameter, carbohydrate incorporation, and amine content in silencing. Dex-SiO_2-NPs are effective at delivering siRNA and inducing silencing, as exhibited via *in vitro* sudies using enhanced green fluorescent protein (EGFP) (Figure 4.1).[11, 12] Herein the design and characterization of Dex-SiO_2-NPs as delivery vehicles are described. The performance of select variations as siRNA delivery vehicles is presented in terms of EGFP fluorescence *in vitro*.

4.2 Nanoparticle Delivery Vehicle Design and Characterization

Dex-SiO_2-NP delivery vehicles were designed to be biocompatible, bind siRNA, and be of precise size and shape. The carbohydrate dextran, known for its biocompatibility, is incorporated into the nanoparticle. Amine moieties are incorporated into Dex-SiO_2-NPs using APTES (Scheme 4.1). At physiological pH, at which the delivery vehicles would operate, exposed amines will be protonated and therefore positively charged, electrostatically binding negatively charged siRNA.

Zeta potential measurements were used to verify that amine groups were present on the surface, as indicated by a positive zeta potential. Comiskey varied the concentration of APTES in the synthesis of from 0.05 - 99 mol % Dex-SiO_2-NPs and SiO_2-NPs (Figure 4.1). Comiskey observed increasing silencing (decreased fluorescence of EGFP) from 0.05% amine to 40% amine in NPs containing dextran. An increase in fluorescence, indicative of less effective silencing, was observed

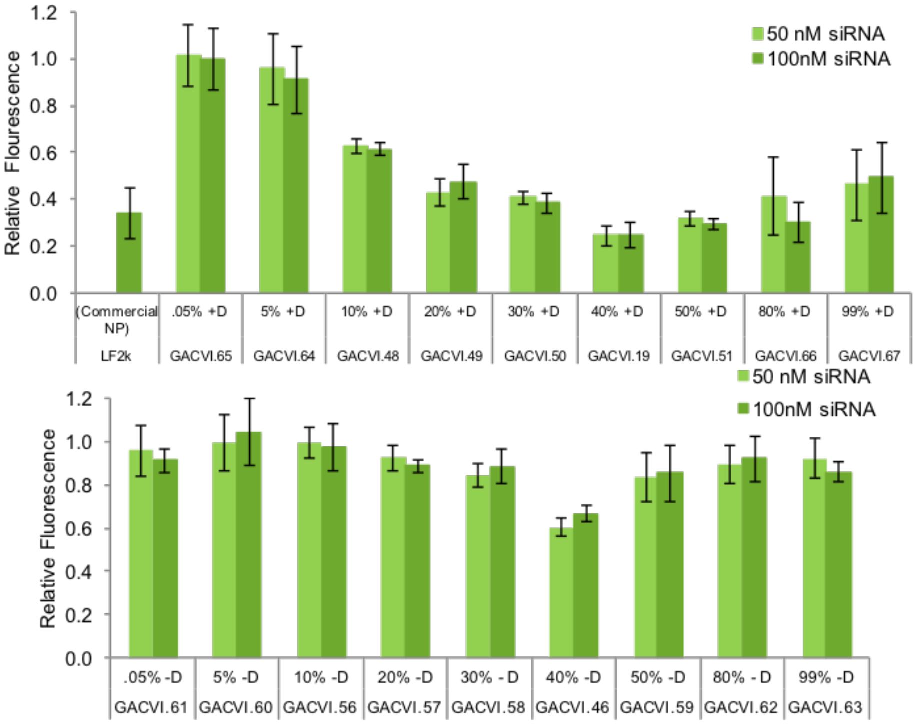

Figure 4.1: *EGFP Silencing by Comiskey Dex-SiO_2-NPs and SiO_2-NPs.* Silencing of EGFP expressed as relative fluorescence by Dex-SiO_2-NPs (top) and SiO_2-NPs (bottom) of varying amine content.[11]

for the 50%, 80%, and 99% Dex-SiO_2-NPs. SiO_2-NPs synthesized without dextran did not elicit significant silencing regardless of amine content.[11]

Scheme 4.1: *Dex-SiO_2-NP Synthetic Scheme.*

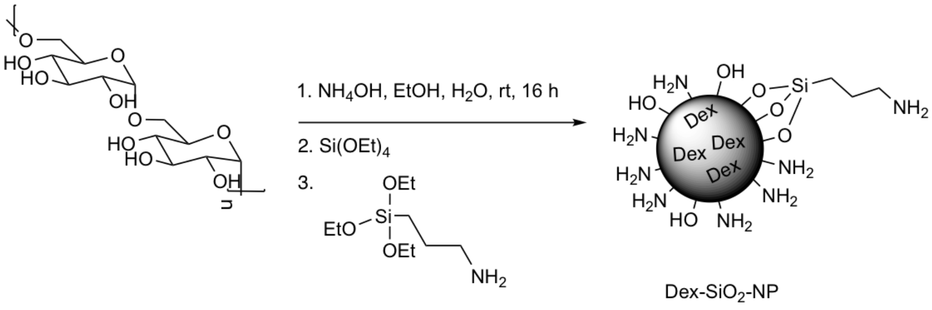

The ninhydrin reagent was used to quantify accessible amines on Dex-SiO_2-NPs according to literature precedent.[116,117] Reaction of a primary amine with ninhydrin yields a purple complex,

Scheme 4.2: *General Reaction of Primary Amine and Ninhydrin to Produce Ruhemann's Purple.*

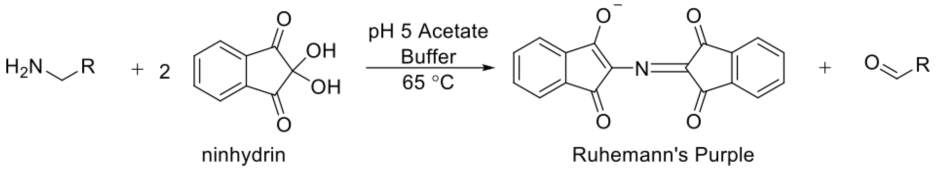

Table 4.1: *Dex-SiO$_2$-NPs Amine Quantification by Ninhydrin Assay.* Zeta potential and Ninhydrin Amine Quantification of Dex-SiO$_2$-NPs with varying amine content, synthesized using Dex-SiO$_2$-350 conditions.

APTES (mmol)	Zeta Potential in H_2O (mV)	Amine Quantity (mmol NH_2/mg NP)
1.2	+17	0.0037
0.3	+25	0.0079
0.075	+9	0.0028
0.038	-4	0.0013

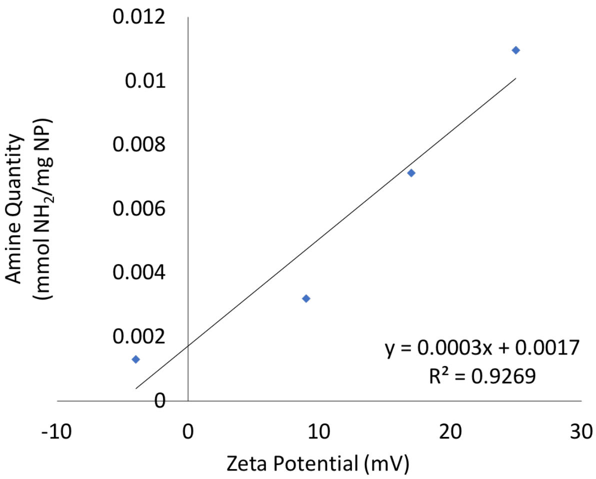

Figure 4.2: *Correlation between Dex-SiO$_2$-NP zeta potential and amount of amine (mmol/mg) detected by the ninhydrin assay for the NPs listed in Table 4.1.*

known as Ruhemann's purple, having a λ_{max} of 588 nm (Scheme 4.2). A calibration curve was constructed after reacting APTES with ninhydrin (Figure C.2). Table 4.1 summarizes the amine quantification results for a series of Dex-SiO$_2$-NPs synthesized with varying amine content.

With decreasing APTES, a decrease in zeta potential was observed (Table 4.1). With the exception of the second entry in Table 4.1, a decrease in APTES is correlated with decreased amine content measured via the ninhydrin assay. The second entry in Table 4.1 lies outside of this trend. This may result from amines "buried" within the silica structure in the Dex-SiO$_2$-NPs of the first entry, hence inaccessible by the ninhydrin reagent and resulting in a smaller detectable amount by the assay. Nonetheless, a correlation exists ($R^2 = 0.9269$) between amine quatity and zeta potential of the nanoparticles (Figure 4.2).

4.3 Nanoparticle Delivery Vehicle Performance

Dex-SiO$_2$-NPs were evaluated on their ability to silence the expression of EGFP in H1299, HEK293, and HELA cell lines. siRNA containing the complimentary sequence to the mRNA of EGFP were transfected to cells using amine-functionalized Dex-SiO$_2$-NPs as described in Chapter 6. A decrease in fluorescence is indicative of silencing. The data here are normalized against untreated cells, such that a relative fluorescence less than 1 is indicative of silencing. Silencing results for 40% amine-functionalized Dex-SiO$_2$-NPs prepared using a variety of dextrans and cyclodextrins in H1299 and HEK293 *in vitro* are presented herein.

Among the Dex-SiO$_2$-NPs prepared using different molecular weights of dextran, Dex-SiO$_2$-350 NPs synthesized using 9-11 kDa dextran elicited the most significant silencing (Figure 4.3). Of the Dex-SiO$_-$350 NPs Comiskey prepared, the 40% amine with 9-11 kDa dextran also achieved the best silencing (Figure 4.1).

The cyclodextrin-incorporated Dex-SiO$_2$-NPs did not elicit significant silencing, with performance slightly improved in HEK293 cells compared with H1299 (Figure 4.4). There was no significant difference in silencing among α-cyclodextrin NPs and β-cyclodextrin NPs. Despite the mediocre silencing results, none of the Dex-SiO$_2$-NPs were cytotoxic.

In addition to the silencing results for the various Dex-SiO$_2$-NPs described in this work, further evidence of successful *in vitro* transfection was obtained via TEM. 24 hours following transfection, H1299 and HELA cells were suspended in a resin. The resin was sectioned, and a thin film was placed on a TEM grid. The resulting micrographs depict NPs existing within cellular vesicles and surrounding cells (Figures 4.5 and B.57). Some Dex-SiO$_2$-NPs appear smaller and less

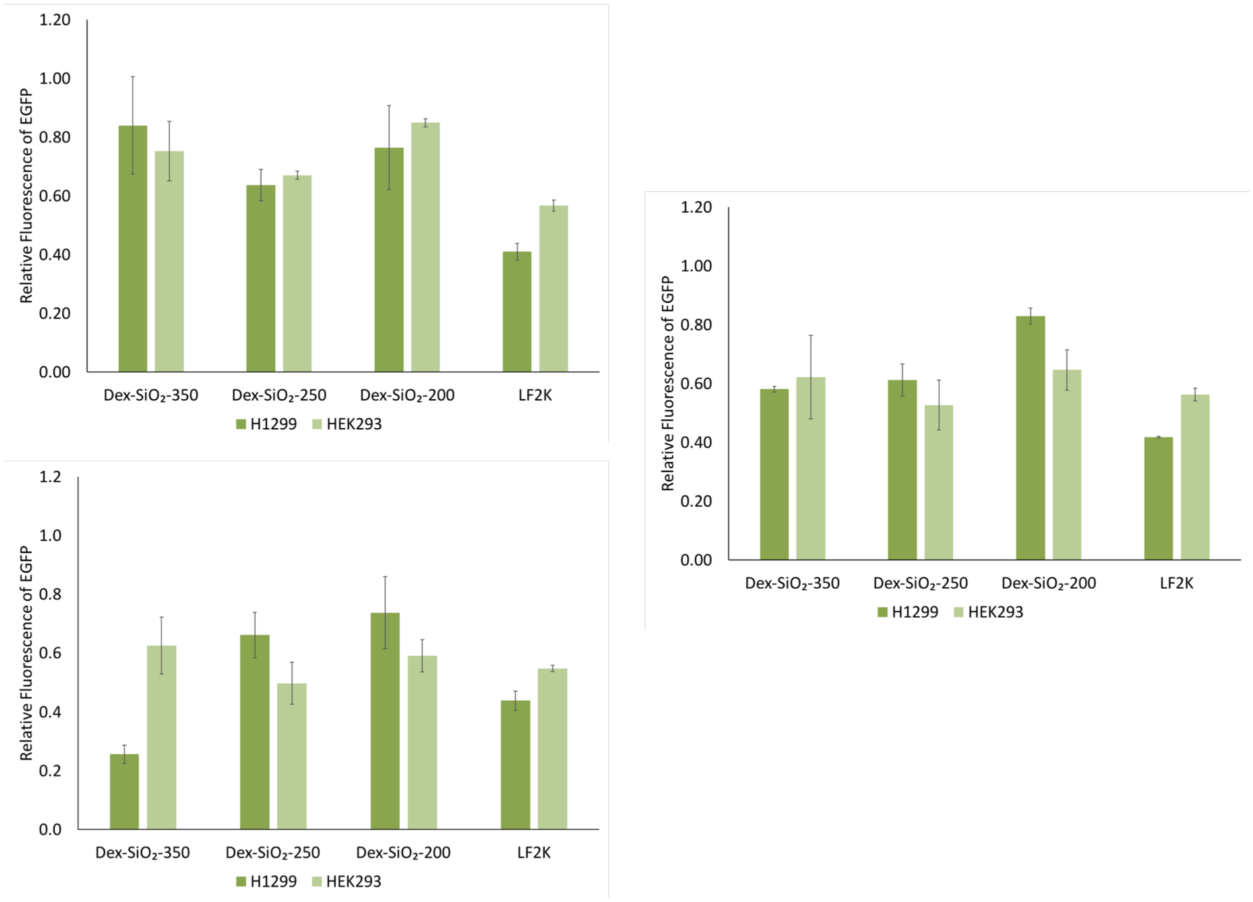

Figure 4.3: *EGFP Silencing of Dex-SiO$_2$-NPs prepared using Dextran. In vitro* silencing quantified via fluorescence of EGFP in H1299 (dark) and HEK293 (light) cell lines prepared using 6 kDa dextran (top left), 9-11 kDa dextran (bottom left), and 40 kDa dextran (right). Experiments performed using 200 μg/mL NP and 50 nM siRNA. Fluorescence measured 24 hours post-transfection. Error bars represent the standard deviation of three data points.

dense, suggesting that Dex-SiO$_2$-NPs may be degraded by the transfection process and/or cellular components. S-TEM and EDS were used to verify the presence of silicon in objects assumed to be Dex-SiO$_2$-NPs. A variety of structures were studied, ranging from large, dark NPs to smaller, more hollow NPs. As the line scans in Figure 4.6 illustrate, EDS confirmed that these structures include silicon. The decreased intensity of the smaller NPs (Figure 4.6, center) indicates a decrease in silicon abundance compared with the other structures.

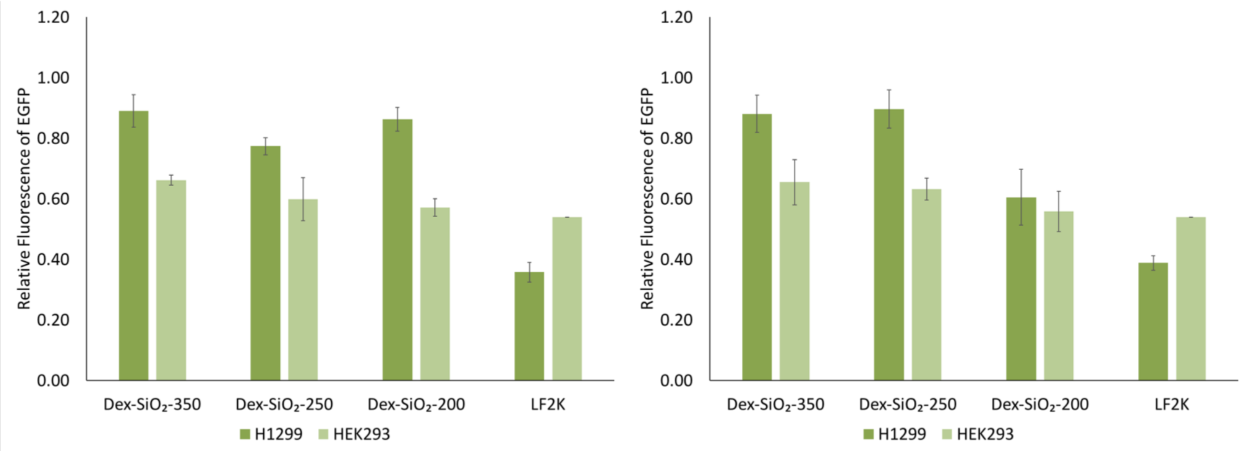

Figure 4.4: *EGFP Silencing of Dex-SiO$_2$-NPs prepared using Cyclodextrin. In vitro* silencing quantified via fluorescence of EGFP in H1299 (dark) and HEK293 (light) cell lines prepared using, from left, α-cyclodextrin and β-cyclodextrin. Experiments performed using 200 μg/mL NP and 50 nM siRNA. Fluorescence measured 24 hours post-transfection. Error bars represent the standard deviation of three data points.

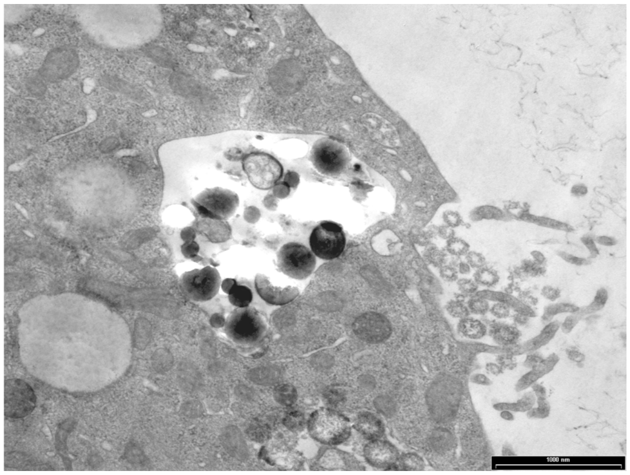

Figure 4.5: *TEM Micrograph of 40% Amine Dex-SiO$_2$-350 in H1299 Cells.* H1299 cells suspended in resin 24 hours post-transfection with siRNA-loaded Dex-SiO$_2$-NPs. Brightness enhanced by 20% to emphasize detail, scale bar 1000 nm. Image from reference 12.

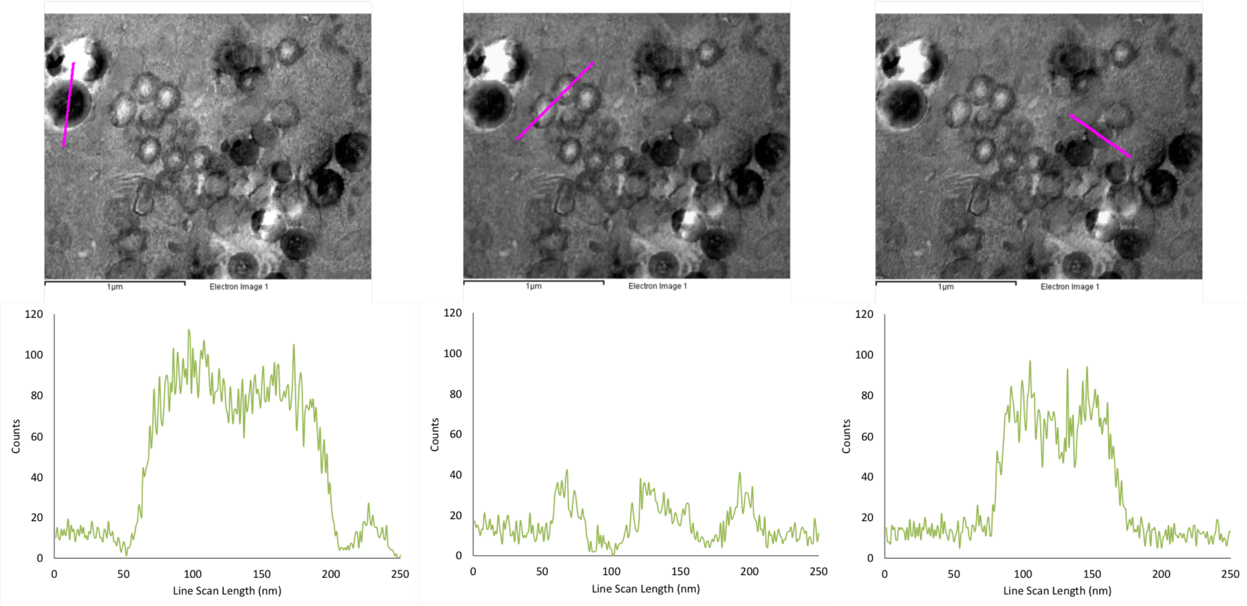

Figure 4.6: *STEM Micrograph and EDS Line Scan of 40% Amine Dex-SiO$_2$-350 in H1299 Cells*. S-TEM micrographs of H1299 cells suspended in resin 24 hours post-transfection with siRNA-loaded Dex-SiO$_2$-NPs with area scanned for EDS analysis indicated by fuschia line (top). Silicon elemental abundance profile along indicated area (bottom). Brightness enhanced by 20% to emphasize detail, scale bar 1 μm.

4.4 Endocytosis of Dex-SiO$_2$-NPs *In Vitro*

The origins of improved silencing of Dex-SiO$_2$-NPs compared to SiO$_2$-NPs were studied. Different endocytotic inhibitors were incubated with cells prior to transfection (Table 4.2). After 24 hours, the fluorescence of EGFP was measured in cells transfected with naked siRNA (control), LF2K, and Dex-SiO$_2$-350 NPs functionalized with 40% APTES (Figure 4.7). No silencing was observed when naked siRNA was used regardless of inhibitor. Inhibition of ATP-dependent processes and the scavenger receptor pathway was observed when LF2K was used for transfection. Transfection using Dex-SiO$_2$-NP was not inhibited by chloropromazine, filipin, or the two used together. Inhibition was observed when cytochalasin D, low temperatures, and dextran sulfate were used. This indicates that actin-dependent, energy-dependent, and scavenger receptor pathways are involved in the endocytosis of these delivery vehicles.

Table 4.2: *Endocytotic Inhibitors and Action Mechanism.* Table adapted from reference 12.

Inhibitor	Target
Chloropromazine	Clathrin-mediated endocytosis
Filipin	Caveolae-mediated endocytosis
Cytochalasin D	Actin dependent processes
Temperature	Energy dependent processes
Dextran Sulfate	Scavenger receptors

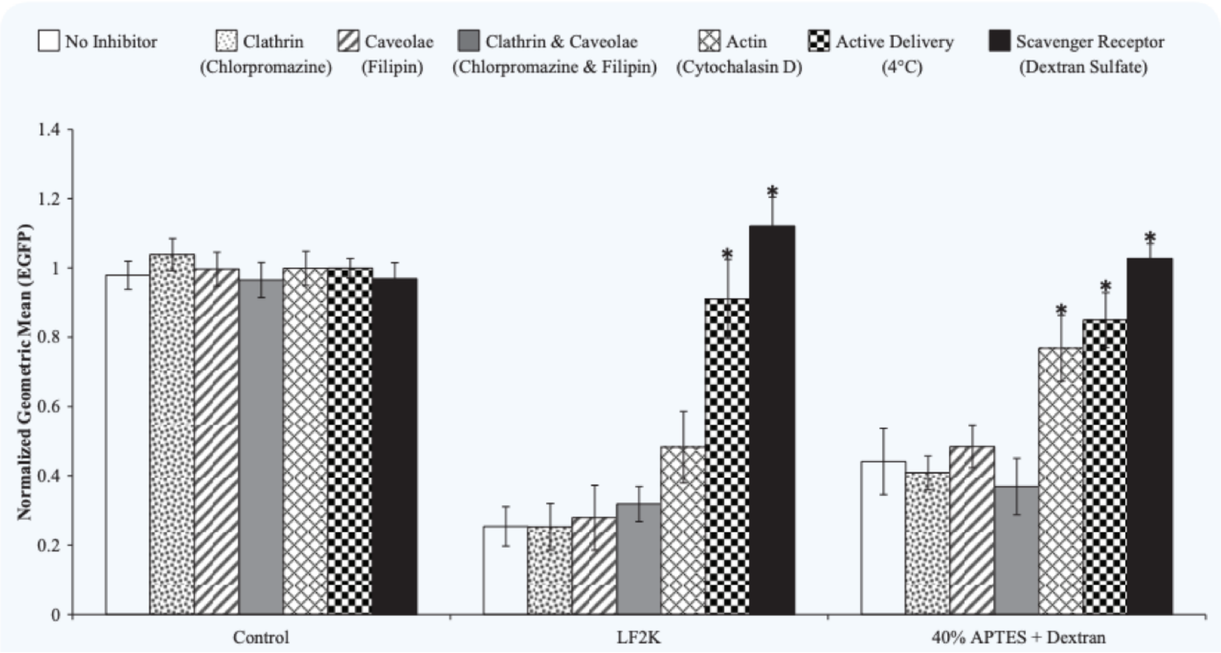

Figure 4.7: *Silencing of EGFP in the Presence of Endocytotic Inhibitors.* Silencing evaluated in H1299 cells 24 hours post-transfection. Results normalized to cells containing nanoparticles only. Error bars represent ±1 standard deviation; n = 3. *Significant difference ($p < 0.05$) as compared to conditions without inhibitors. Image reproduced from reference 12 ©World Scientific Publishing Co./Imperial College Press 2016.

4.5 Conclusions

Building on Comiskey's work preparing Dex-SiO_2-NPs with varying amine content, this work has taken the 40% amine variation containing dextran and expanded the types of carbohydrate incorporated in the NP. In addition to using 9-11 kDa dextran, studied by Comiskey, 6 kDa and 40 kDa dextran and α- and β-cyclodextrin were incorporated into NPs using Dex-SiO_2-350, Dex-SiO_2-250, and Dex-SiO_2-200 conditions. The silencing ability of this range of Dex-SiO_2-NPs were studied via EGFP knockdown in H1299 and HEK293 cells. While no significant insights were gained from the variation of delivery vehicle size and dextran content, further studies may be conducted varying amine content and synthetic conditions within these new Dex-SiO_2-NP classifications. Resin-suspended cells were inspected by TEM 24 hours post-transfection, revealing Dex-SiO_2-NPs within cellular vesicles and around the perimeter of cells. Both intact NPs and some appearing to have been degraded were present in both regions, suggesting that the Dex-SiO_2-NPs are subject to degradation within the slightly acidic cellular environment.

CHAPTER 5

FUTURE RESEARCH DIRECTIONS

5.1 Expanding Synthetic Directions

The results and experiments herein have provided insight to the synthesis of Dex-SiO_2-NPs. Nevertheless, questions remain which merit further investigation. This work has shown that monodispersed Dex-SiO_2-NPs are easily accessible when purified silicate starting materials are used. Expanding upon the knowledge that dextran aggregation gives rise to the unique morphology, the diameters of accessible Dex-SiO_2-NPs can be expanded. Further optimization of the post-synthetic treatment of Dex-SiO_2-200 and Dex-SiO_2-250 NPs should also be explored to facilitate characterization. Integration of different carbohydrates into SiO_2-NPs is another direction that can be further explored using the methods and techniques established herein.

5.2 Silencing Implications

The size variation and polydispersity of Comiskey's nanoparticles add uncertainty to the role of delivery vehicle size. While Comiskey's work showed that silencing using Dex-SiO_2-NPs was better than SiO_2-NPs, a better comparison may now be accomplished with monodispersed Dex-SiO_2-NPs and SiO_2-NPs in a comparable size range. This would provide a more robust comparison of the effect of delivery vehicle size on silencing ability. Since dextran can be removed by calcination, re-functionalization of calcined Dex-SiO_2-NPs with APTES or APTES and surface-bound dextran would provide valuable control experiments.

CHAPTER 6

EXPERIMENTAL METHODS

6.1 Materials

Tetraethyl ortho silicate (TEOS) and 3-aminopropyl triethoxy silane (APTES) were obtained from Millipore Sigma and distilled prior to use.[118] 9-11 kDa dextran was obtained from Millipore Sigma and was used without further purification. Ethanol (200 proof), ammonium hydroxide (approximately 30% as NH_3), and Milli-Q water (18MΩ) were used as received. 30 kDa molecular weight cut off regenerated cellulose membranes (47 mm diameter) were purchased from Millipore Sigma. MilliQ water was obtained from a Millipore Synergy UV water purification system, RNAase free water was purchased from Fisher Scientific. 300 mesh carbon-coated copper TEM grids and carbon-coated nickel grids were purchased from Ted Pella, Inc.

6.2 Characterization

Transmission Electron Microscopy

Nanoparticle powder was suspended in ethanol and sonicated until well dispersed. 5 μL of the suspension was pipetted onto a copper TEM grid. Images were acquired using a JEOL 100CXII transmission electron microscope operating at an accelerating voltage of 100 keV and equipped with either a GATAN Orius digital camera or an Olympus MegaView III digital camera.

Distributions of nanoparticle diameter were obtained after measuring at least 100 nanoparticles[20, 119] using CellProfiler 2.2.0. The CellProfiler pipeline first inverted the image and applied a grayscale threshold such that dark pixels below the threshold are set to zero. Objects were identified based on their intensity and their areas and diameters were measured. Object diameters were separated into 10 nm bins based on diameter (converted from pixels to nanometers based on the number of pixels comprising the scale bar) and eccentricity (< 0.4, more circular than oblong).

Histograms of object diameters were generated from no less than 100 individual measurements. TEM micrographs of NP-containing cells were prepared as described in reference 12. 24 hours post-transfection, H1299 or HELA cells were suspended in resin, allowed to solidify, and then sectioned. A sectioned film was placed on a TEM grid and studied via TEM or S-TEM.

Silver Methanamine Staining for TEM

100 mL solutions of 3% hexamethylene tetramine (methenamine), 5 mL 5% silver nitrate, 0.5% periodic acid and 5% sodium borate were prepared in MilliQ water. The silver methenamine stock solution was prepared by adding the silver nitrate solution dropwise to the methenamine solution. The solution was filtered through a 0.2 μm PTFE filter into an amber bottle. The stock solution was stored at 4 °C until immediately prior to use. The silver methenamine working solution was prepared by mixing 50 mL of silver methenamine stock with 5 mL of 5% sodium borate solution. A 5 μL sample of Dex-SiO_2-NPs was deposited onto a nickel TEM grid and air dried. Following treatment with 0.5% periodic acid solution for 30 minutes, the grid was washed three times by scooping 5 μL droplets of MQ water and absorbing it with the tip of a filter paper wedge. After rinsing, 5 μL of silver methenamine working solution was deposited on the grid and air dried in the dark. The grid was rinsed three times with MilliQ water and air dried prior to analysis.

Energy Dispersive X-Ray Spectroscopy

EDS was performed on a JEOL 2200FS scanning transmission electron microscope operating at an accelerating voltage of 200 keV. EDS results, including line scans, were collected and analyzed using INCA software.

Thermogravimetric Analysis

TGA measurements were obtained using a TA Q500 instrument under air. The sample was heated with a thermal ramp rate of 15 °C per minute to 800 °C.

Surface Area and Porosity Analysis

Dried Dex-SiO_2-NP powder was degassed at 120 °C for 12 hours prior to surface area and porosity analysis. Nitrogen adsorption/desorption isotherms were obtained using a Micromeritics ASAP 2020 instrument. Brunauer, Emmett and Teller (BET), Barrett, Joyner and Halenda (BJH), and Density Functional Theory (DFT) calculations were used to determine the surface area, porosity, and porosity distributions.

CP-MAS ^{13}C NMR

Dry Dex-SiO_2-NP powder was loaded into a 6 mm zirconia rotor. Solid State CP-MAS ^{13}C NMR was performed on a Varian Infinity Plus spectrometer operating at 400 MHz. The sample was spun at 5 kHz and was referenced to adamantane.

Dynamic Light Scattering

Hydrodynamic diameters and ζ potentials were measured using a Malvern Zetasizer NanoZS. Hydrodynamic radius measurements by dynamic light scattering were performed using disposable UV cuvettes purchased from Brandtech®and ζ potential measurements were performed using a folded capillary zeta cell purchased from Malvern Panalytical. A 500 μL stock solution of 1.0 mg/mL was measured, diluted two-fold, and measured again. The sample was measured after every dilution until the zeta potential and hydrodynamic diameter were stabilized near 0.05 mg/mL.

In vitro Gene Silencing Experiments

siRNA was bound to Dex-SiO_2-NPs suspended in MilliQ H_2O and evaluated for silencing in H1299 cells expressing EGFP as described in reference 12.

6.3 Synthetic Procedures

Synthesis of Dextran-SiO_2 Nanoparticles

Preparation of Dex-SiO_2-100

190 mL of absolute ethanol and 10 mL of MilliQ water were added to a 500 mL round bottom flask. Dextran (9-11 kDa, 2.4 x 10^{-6} mol, 24 mg) was dissolved in 10 mL of MilliQ water and added to the reaction solution, followed by 10 mL of NH_4OH. TEOS (0.024 mmol, 0.053 mL) was added dropwise by syringe and the mixture was stirred at room temperature for 16 hours. The reaction solution was purified via pressure filtration under nitrogen using a 30 kDa molecular weight cut off regenerated cellulose membrane. The solid Dex-SiO_2-NP powder was transferred to a centrifuge tube and rinsed three times with ethanol and twice with MilliQ water. Yields averaged 0.13 g.

Preparation of Dex-SiO_2-200

190 mL of absolute ethanol and 10 mL of MilliQ water were added to a 500 mL round bottom flask. Dextran (9-11 kDa, 2.4 x 10^{-6} mol, 24 mg) was dissolved in 10 mL of MilliQ water and added to the reaction solution, followed by 10 mL of NH_4OH. TEOS (2.4 mmol, 0.53 mL) was added dropwise by syringe and the mixture was stirred at room temperature for 16 hours. The reaction solution was purified via pressure filtration under nitrogen using a 30 kDa molecular weight cut off regenerated cellulose membrane. The solid Dex-SiO_2-NP powder was transferred to a centrifuge tube and rinsed three times with ethanol and twice with MilliQ water. Yields averaged 0.13 g.

Preparation of Dex-SiO_2-240

170 mL of absolute ethanol and 30 mL of MilliQ water were added to a 500 mL round bottom flask. Dextran (9-11 kDa, 2.4 x 10^{-6} mol, 24 mg) was dissolved in 10 mL of MilliQ water and added to the reaction solution, followed by 10 mL of NH_4OH. TEOS (2.4 mmol, 0.53 mL) was added dropwise by syringe and the mixture was stirred at room temperature for 16 hours. The reaction solution was purified via pressure filtration under nitrogen using a 30 kDa molecular weight cut off regenerated cellulose membrane. The solid Dex-SiO_2-NP powder was transferred to a cen-

trifuge tube and rinsed three times with ethanol and twice with MilliQ water. Yields averaged 0.13 g.

Preparation of Dex-SiO_2-350

150 mL of absolute ethanol and 50 mL of MilliQ water were added to a 500 mL round bottom flask. Dextran (9-11 kDa, 2.4 x 10^{-6} mol, 24 mg) was dissolved in 10 mL of MilliQ water and added to the reaction solution, followed by 10 mL of NH_4OH. TEOS (2.4 mmol, 0.53 mL) was added dropwise by syringe and the mixture was stirred at room temperature for 16 hours. The reaction solution was purified via pressure filtration under nitrogen using a 30 kDa molecular weight cut off regenerated cellulose membrane. The solid Dex-SiO_2-NP powder was transferred to a centrifuge tube and rinsed three times with ethanol and twice with MilliQ water. Yields averaged 0.13 g.

Preparation of Amino-Dextran-SiO_2 Nanoparticles

150 mL of absolute ethanol and 10, 30, or 50 mL of MilliQ water were added to a 500 mL round bottom Schlenk flask. Dextran (9-11 kDa, 2.4 x 10^{-6} mol, 24 mg) was dissolved in 10 mL of MilliQ water and added to the reaction solution, followed by 10 mL of NH_4OH. TEOS (2.4 mmol, 0.53 mL) was added dropwise by syringe and the mixture was stirred at room temperature for 10 minutes before the addition of APTES (40 mol%, 0.96 mmol, 0.224 mL). The reaction solution was stirred for 16 hours at room temperature and purified via pressure filtration under nitrogen using a 30 kDa molecular weight cut off regenerated cellulose membrane. The solid Dex-SiO_2-NP powder was transferred to a centrifuge tube and rinsed three times with ethanol and twice with MilliQ water. The filtered solid was resuspended in MilliQ water and sonicated until well dispersed. Yields averaged 0.13 g.

Preparation of Amine-Coated SiO_2 Nanoparticles Using Various Carbohydrates

150 mL of absolute ethanol and 10, 30, or 50 mL of MilliQ water were added to a 500 mL round bottom Schlenk flask. The selected carbohydrate (6 kDa dextran, 4 x 10^{-6} mol, 24 mg; 9-11 kDa dextran, 2.4 x 10^{-6} mol, 24 mg; 40 kDa dextran, 6 x 10^{-7} mol, 24 mg; α-cyclodextrin, 2.3 x 10^{-5}

mol, 24 mg; *β*-cyclodextrin, 2.1 x 10^{-5} mol, 24 mg) was dissolved in 10 mL of MilliQ water and added to the reaction solution, followed by 10 mL of NH_4OH. TEOS (2.4 mmol, 0.53 mL) was added dropwise by syringe and the mixture was stirred at room temperature for 10 minutes before the addition of APTES (40 mol%, 0.96 mmol, 0.224 mL). The reaction solution was stirred for 16 hours at room temperature and purified via pressure filtration under nitrogen using a 30 kDa molecular weight cut off regenerated cellulose membrane. The solid Dex-SiO_2-NP powder was transferred to a centrifuge tube and rinsed three times with ethanol and twice with MilliQ water. The filtered solid was resuspended in MilliQ water and sonicated until well dispersed. Yields averaged 0.13 g.

Preparation of SiO_2 Nanoparticles

46 mL of absolute ethanol and 10 mL of NH_4OH were added to a 100 mL round bottom flask affixed with a Schlenk adapter. In a 20 mL scintillation vial, 4 mL of absolute ethanol was mixed with TEOS (5.6 x 10-4 mol, 0.125 mL), this solution was added to the reaction flask dropwise via syringe and stirred for 2 hours under nitrogen. The mixture was purified by repeated centrifugation (30 min at 3000 rpm) and rinsing with ethanol three times. The filtered solid was suspended in ethanol and sonicated until well dispersed. Yield 18 mg.

Process for Amine Coating of Nanoparticles

50 mL of absolute ethanol, 12.5 mL of MilliQ water, and 3.3 mL of NH_4OH were added to a 250 mL Schlenk flask. SiO_2 NPs or Dex-SiO_2-NPs suspended in ethanol (0.0117 g/mL, 0.08775 g, 7.5 mL) were added to the reaction mixture, followed by APTES (concentration varied as listed in Table 2), and stirred for 3 hours under nitrogen. For smaller concentrations of APTES (the final two entries in Table 2), a 15 mM solution of APTES in ethanol was prepared and used to maintain accuracy. The amount of ethanol initially added to the reaction mixture was reduced such that the total volume remained the same. The mixture was purified by repeated centrifugation (30 min at 3000 rpm) and rinsing with ethanol three times. The filtered solid was suspended in ethanol and

sonicated until well dispersed.

Ninhydrin Amine Quantification Assay

100 mM ninhydrin solution in absolute ethanol was freshly prepared. Standard solutions of APTES were prepared in a concentration range of 0.001 mM to 0.5 mM. Functionalized silica nanoparticles were dried under vacuum at 100 °C for 4-6 hours, and then 20 mg of particle was placed in a capped vial with 0.9 mL of absolute ethanol and sonicated until well dispersed. Alternatively, ethanol-suspended nanoparticle was placed in an Eppendorf tube such that 10 mg of particle was present, and centrifuged to remove the ethanol. 0.9 mL of absolute ethanol was added, sonicated until well suspended, and transferred to a capped vial. To each vial, 0.1 mL of pH 5 sodium acetate/acetic acid buffer and 1 mL of 100 mM ninhydrin solution was added, followed by sonication for 10 minutes. Samples were incubated in an oil bath at 65 °C for 30 minutes, and then allowed to come to room temperature. Following transfer to Eppendorf tubes, the sample solutions were centrifuged for 10 minutes at 6000 rpm. The supernatant was analyzed using an ATI Unicam UV2 spectrophotometer with ethanol as blank.

Study of Dex-SiO_2-NP Assembly

0.1 mL of reaction solution was extracted at designated time points of the synthesis of Dex-SiO_2-350 NPs. After removal using a syringe, each sample was diluted, centrifuged, and washed three times with MilliQ water before suspension in ethanol for deposition upon a formvar-coated copper or nickel TEM grid and, in some cases, stained using silver methanamine for dextran detection. **Method A:** TEOS and 9-11 kDa dextran were stirred for 10 minutes, after which APTES was added and the solution was stirred overnight. **Method B:** TEOS and 9-11 kDa dextran were stirred for 20 hours, after which APTES was added and the solution was stirred for one hour.

Dextran Solubility Study

The process for synthesizing Dex-SiO_2-250 was used, varying the alcoholic solvent among methanol, ethanol, or isopropanol and alternating the inclusion of dextran and TEOS such that dextran only, TEOS only, and dextran and TEOS were included. Samples of 0.1 mL of reaction solution were extracted periodically after the addition of Dextran or TEOS and injected into a cuvette. Hydrodynamic diameter was measured by DLS. Products of experiments using TEOS or TEOS and dextran were purified according to Dex-SiO_2-250 and NPs were analyzed by TEM.

6.4 Post-Synthetic Treatment

Filtration

A 10 mL suspension of nanoparticle in water or 10% ethanol in water was prepared at 1.0, 0.1, and 0.01 mg/mL. A pressure filtration reservoir was equipped with the indicated membrane and secured in place by a Teflon O-ring. The suspension was filtered under 40 psi of N_2. The membrane was removed, agitated and rinsed thoroughly with ethanol. The resulting suspension was labeled as the retentate. Both the filtrate and the retentate were concentrated for TEM analysis.

Iterative Filtration

A 50 mL suspension of nanoparticle in ethanol was prepared at 0.01 mg/mL. A pressure filtration reservoir was equipped with a 0.2 μm polycarbonate membrane beneath a 0.45 μm mixed cellulose esters membrane, secured in place by a Teflon O-ring. The suspension was filtered under 40 psi of N_2. Both membranes were removed, agitated and rinsed thoroughly with ethanol. The resulting suspension was labeled as the retentate. The filtrate was collected and kept separate from the retentate. The pressure filtration device was reassembled with the same filters in the same order, and the retentate was filtered once again. This process was initially performed four times, although later repetitions increased that number in order to further separate the nanoparticles. Both the filtrate and the retentate were concentrated and rinsed several times with MilliQ water, ultimately being resuspended in MilliQ water in preparation for in vitro use.

Soxhlet Extraction

Dry nanoparticle powder (2 g) was weighed into a cellulose thimble (Whatman, **SIZE**). 250 mL of MilliQ water was brought to a boil in a 500 mL round bottom flask under nitrogen with stirring. The loaded thimble was placed into the Soxhlet extractor and the corresponding condenser was attached. Extraction was performed over 2 days. The solution was filtered under nitrogen pressure using a 30kDa MWCO regenerated cellulose membrane, concentrated, and lyophilized to recover dextran.

Calcination

Calcination was performed under air in a Thermo Scientific Thermolyne F48025-60 muffle furnace. Dry nanoparticle powder was pulverized, placed in a crucible, and heated at 120 °C for 2 hours in air, followed by a constant temperature between 350 °C and 900 °C for 2 - 100 hours.

APPENDICES

APPENDIX A

NMR SPECTRA

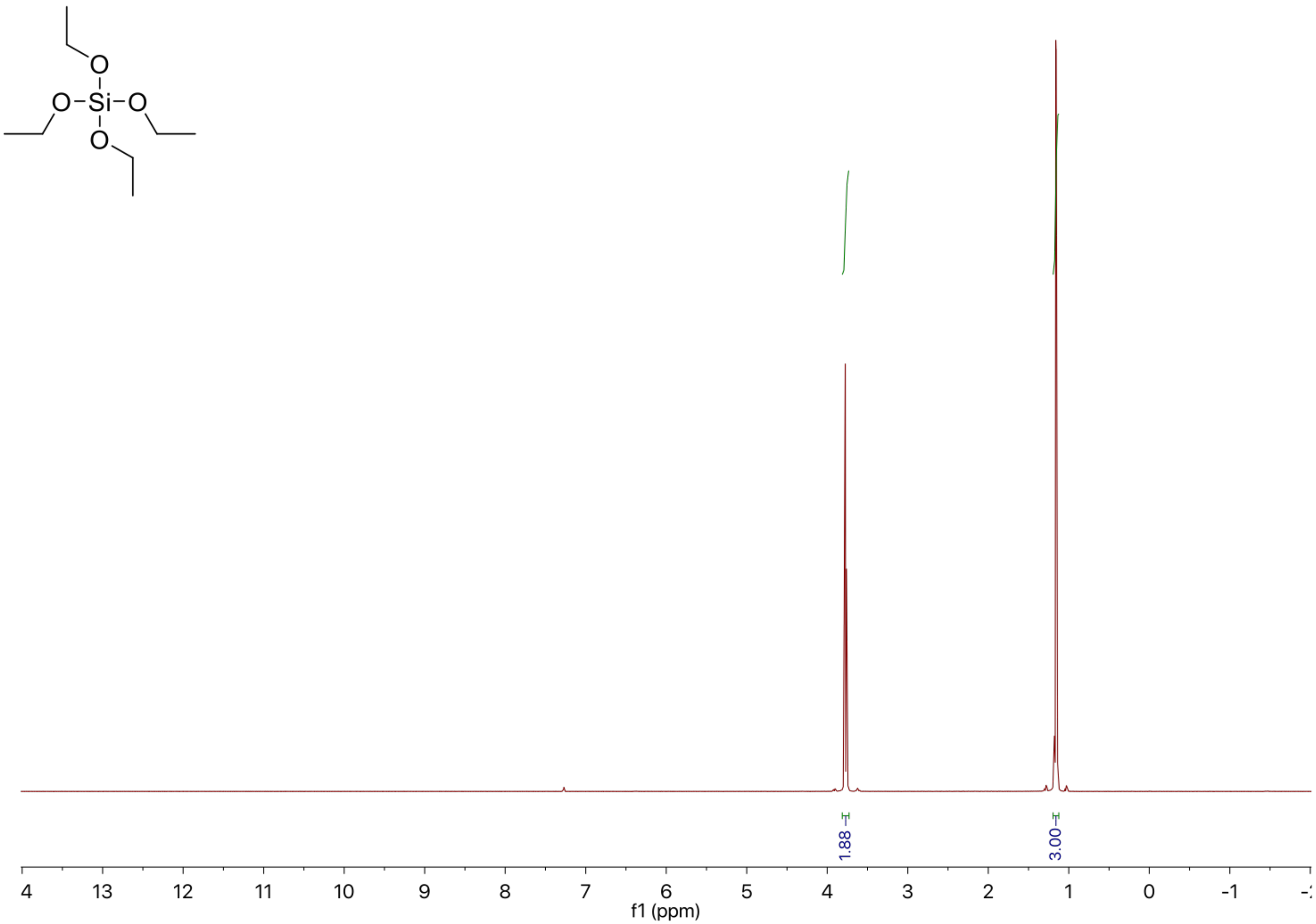

Figure A.1: *500 MHz* ^{1}*H-NMR Spectrum of TEOS in* $CDCl_3$.

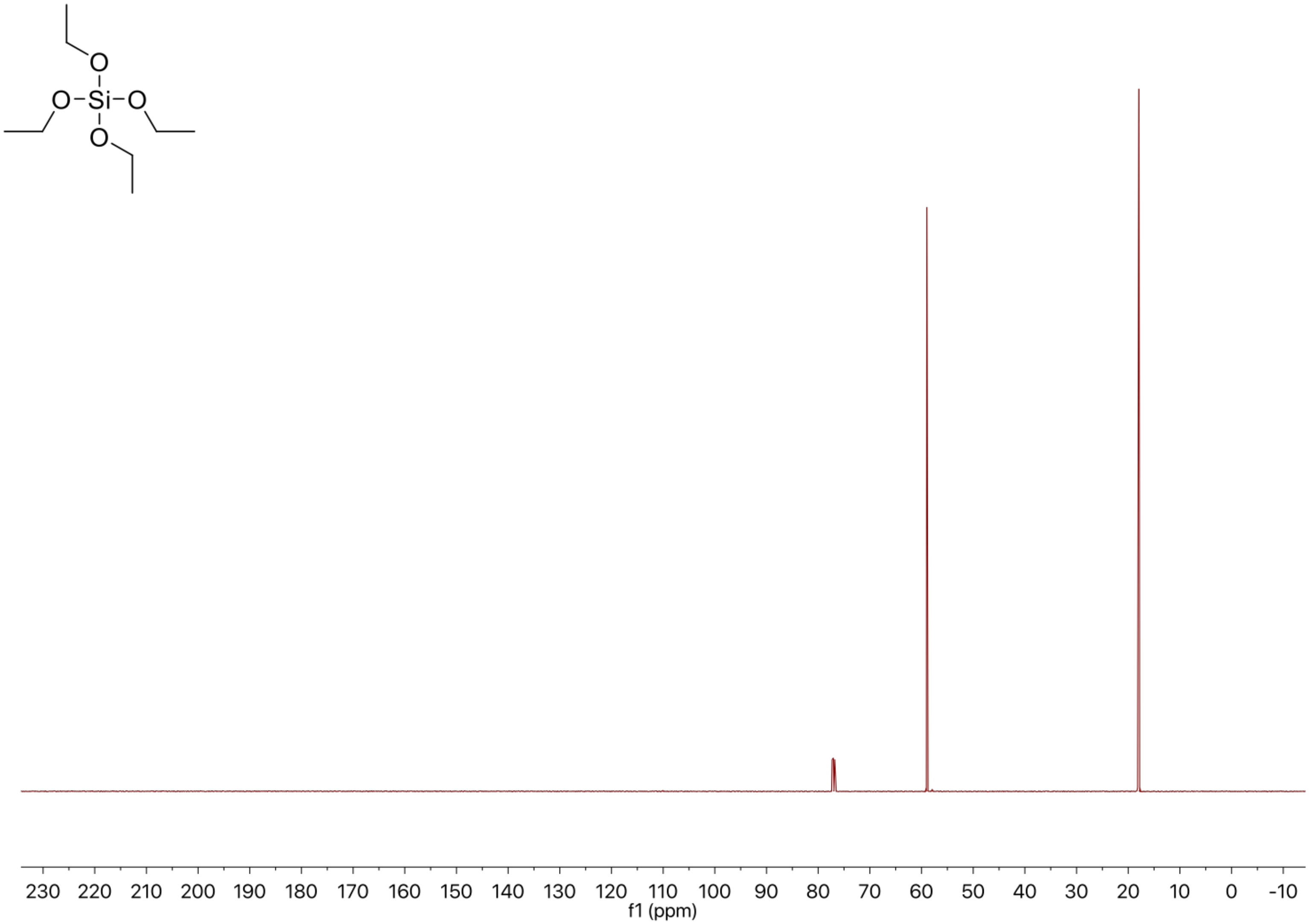

Figure A.2: *125 MHz ^{13}C-NMR Spectrum of TEOS in CDCl$_3$.*

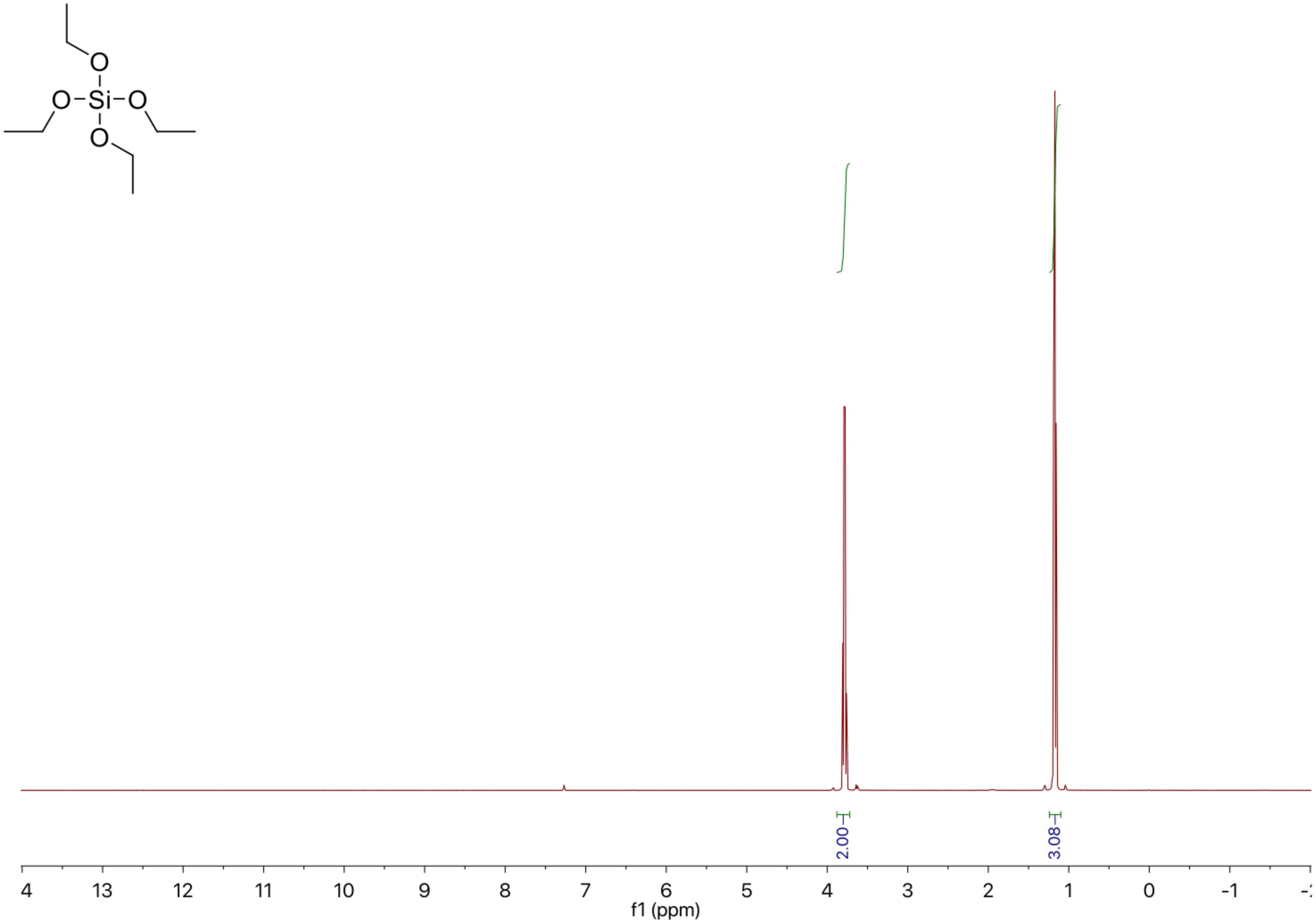

Figure A.3: *500 MHz ^{1}H-NMR Spectrum of TEOS in CDCl$_3$.* Purified by distillation.

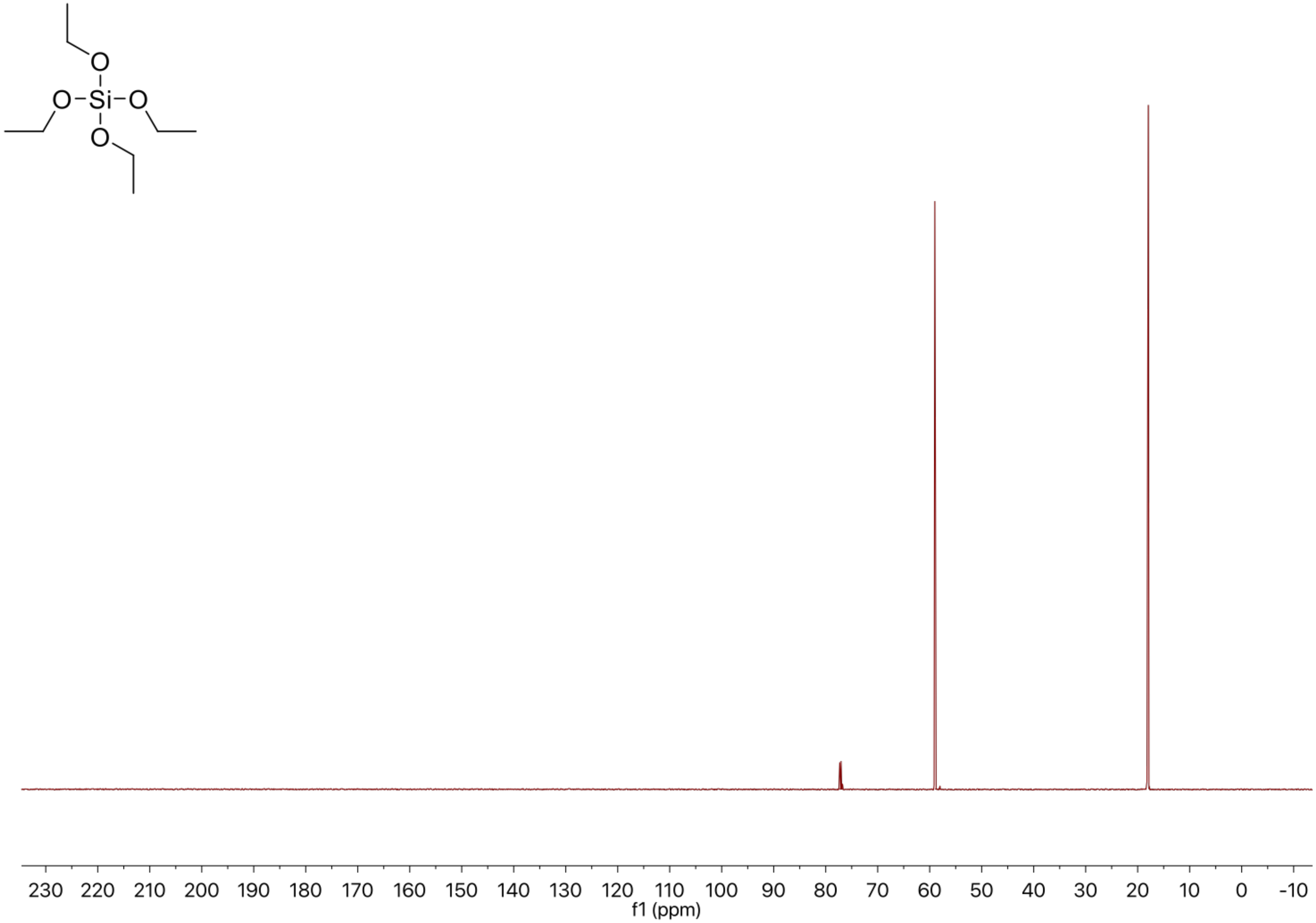

Figure A.4: *125 MHz* ^{13}*C-NMR Spectrum of TEOS in* $CDCl_3$. Purified by distillation.

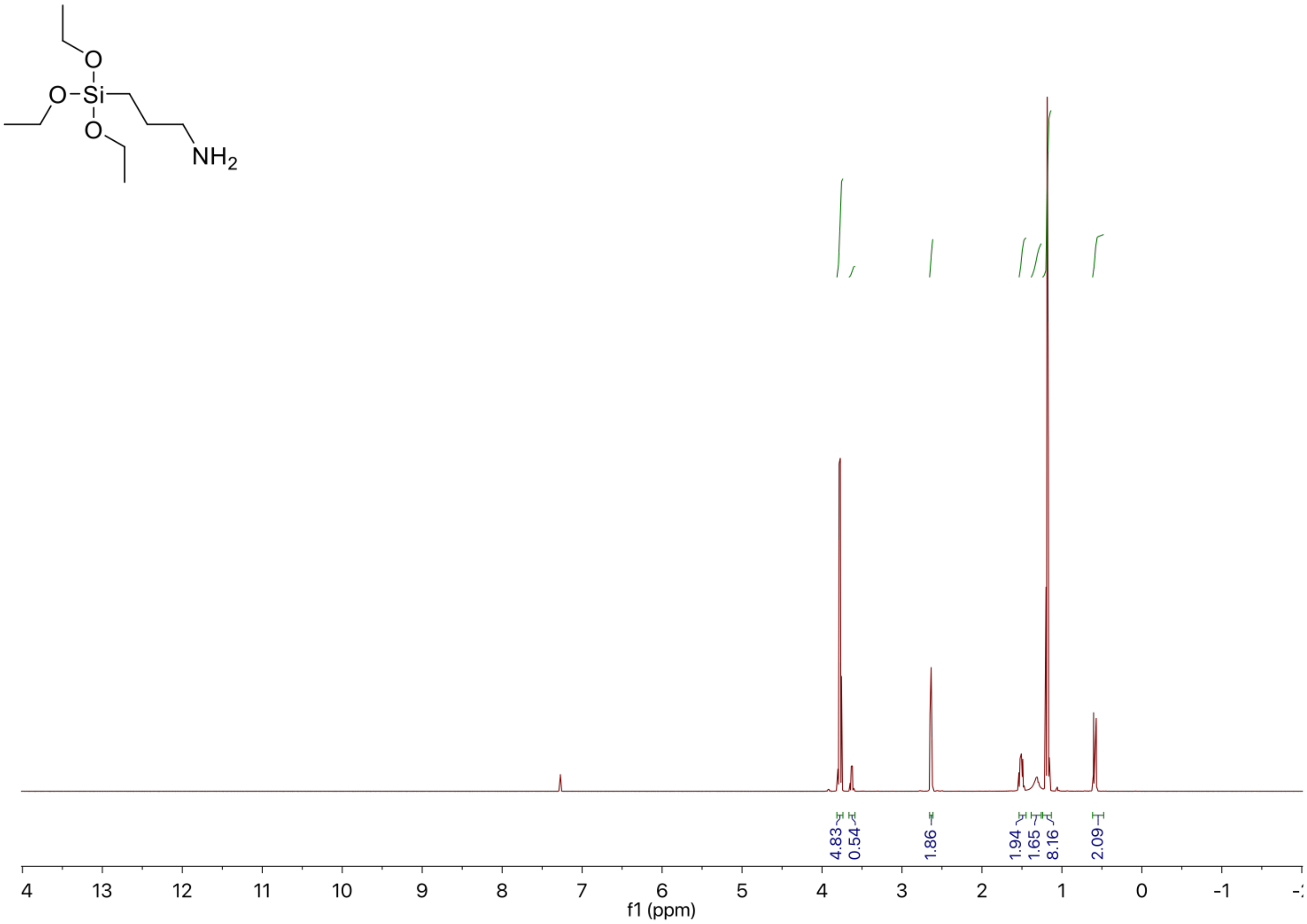

Figure A.5: *500 MHz ^{1}H-NMR Spectrum of APTES in CDCl$_3$.*

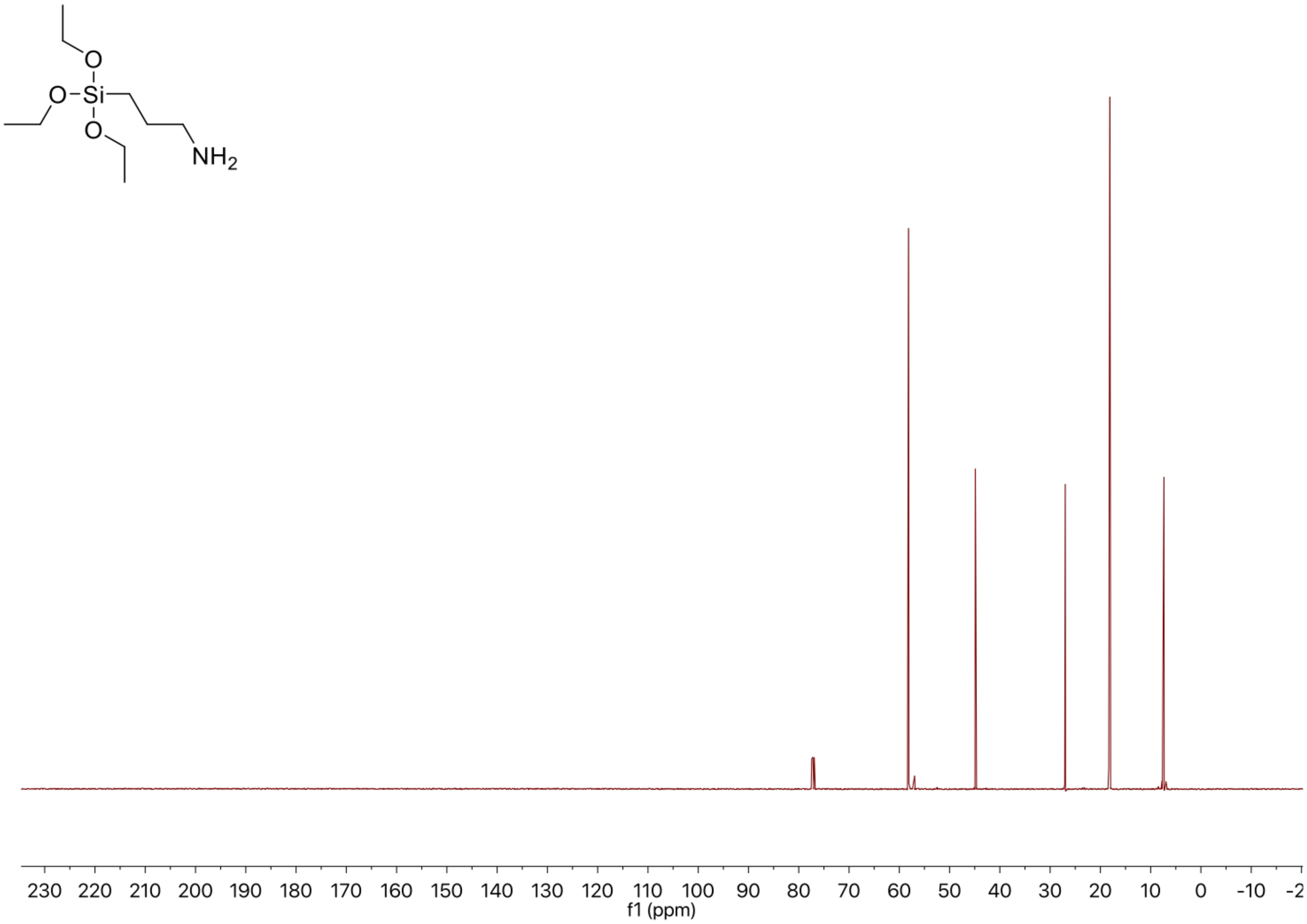

Figure A.6: *125 MHz* ^{13}*C-NMR Spectrum of APTES in* $CDCl_3$.

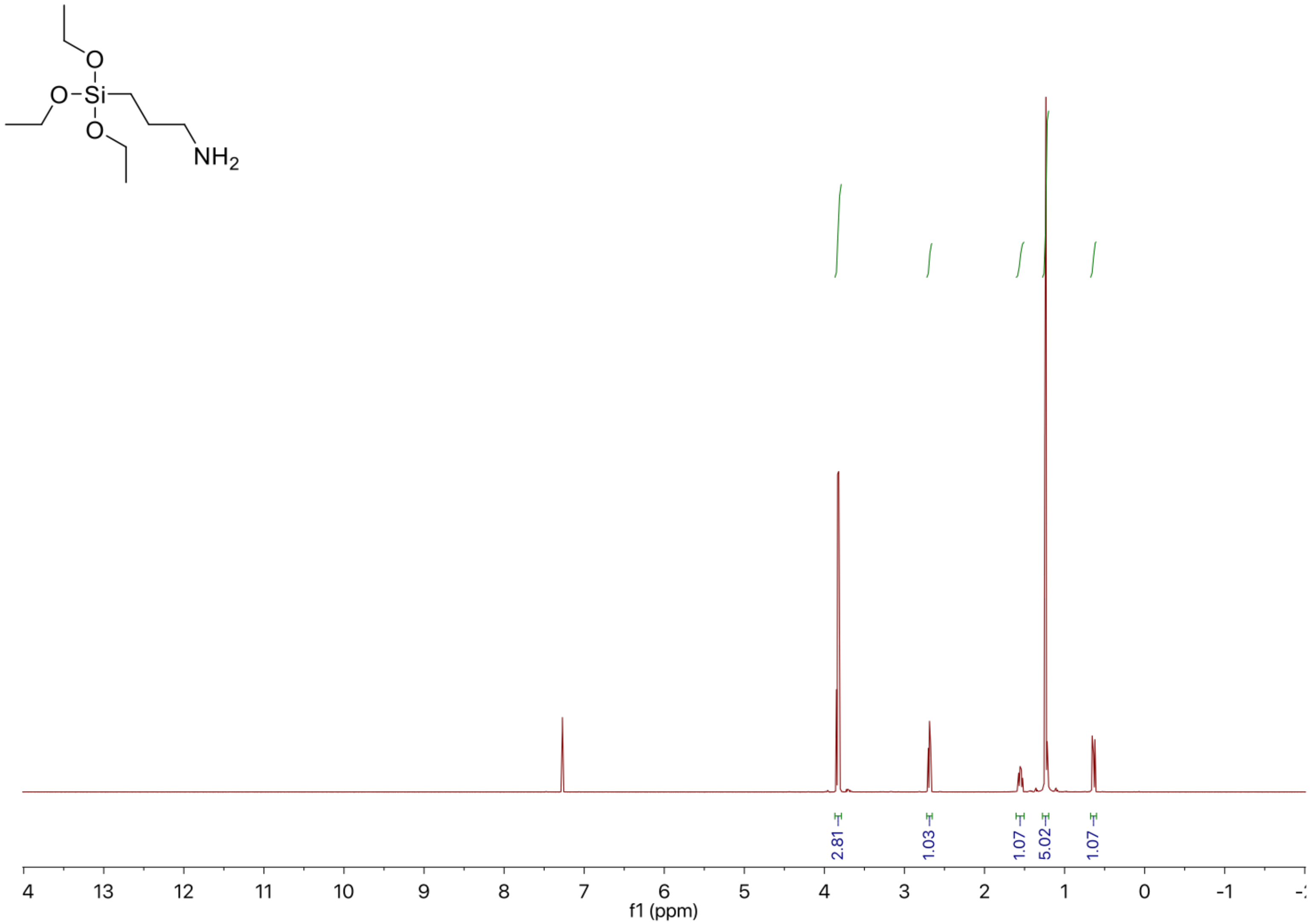

Figure A.7: *500 MHz ^{1}H-NMR Spectrum of APTES in CDCl$_3$.* Purified by distillation.

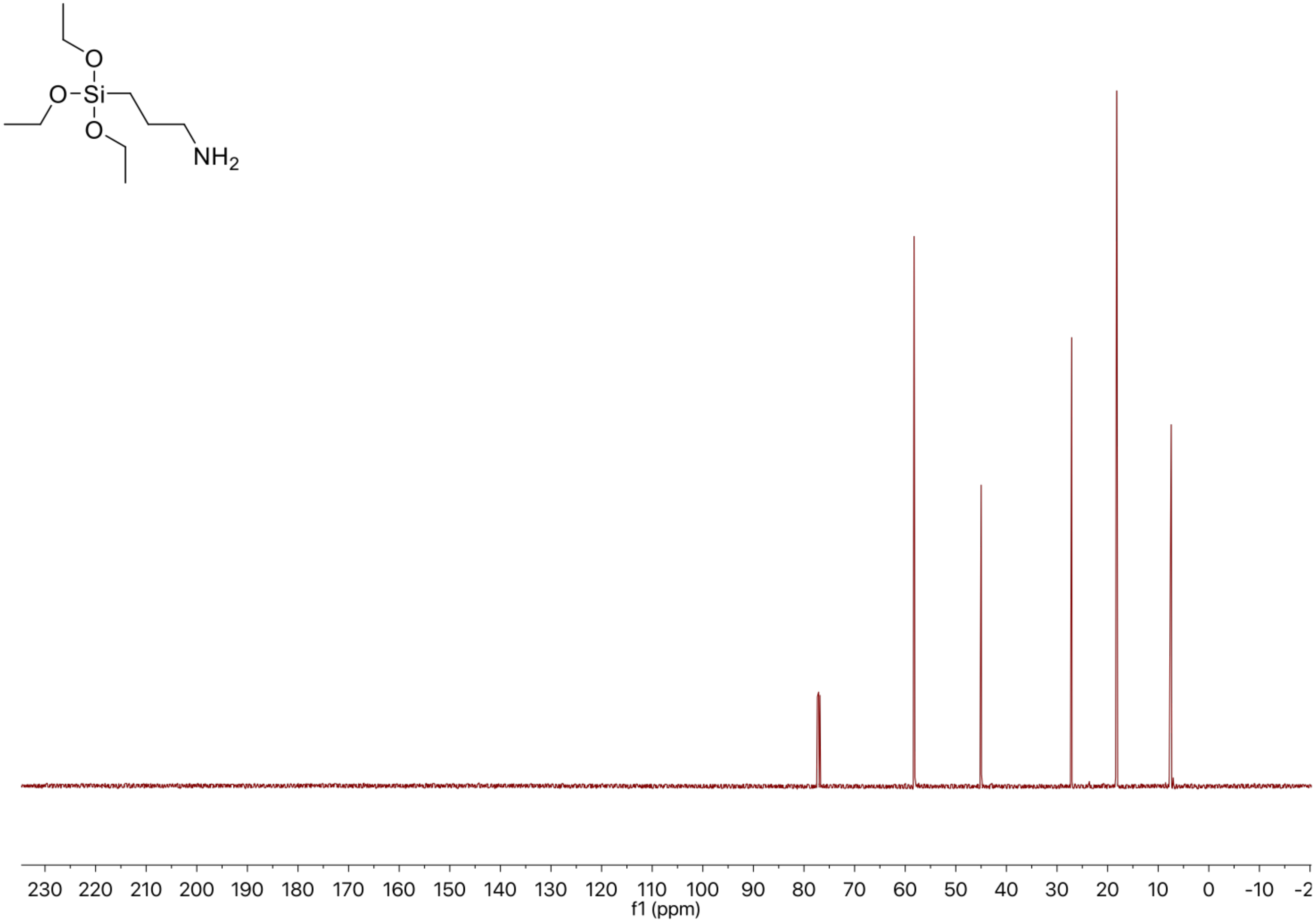

Figure A.8: *125 MHz ^{13}C-NMR Spectrum of APTES in CDCl$_3$.* Purified by distillation.

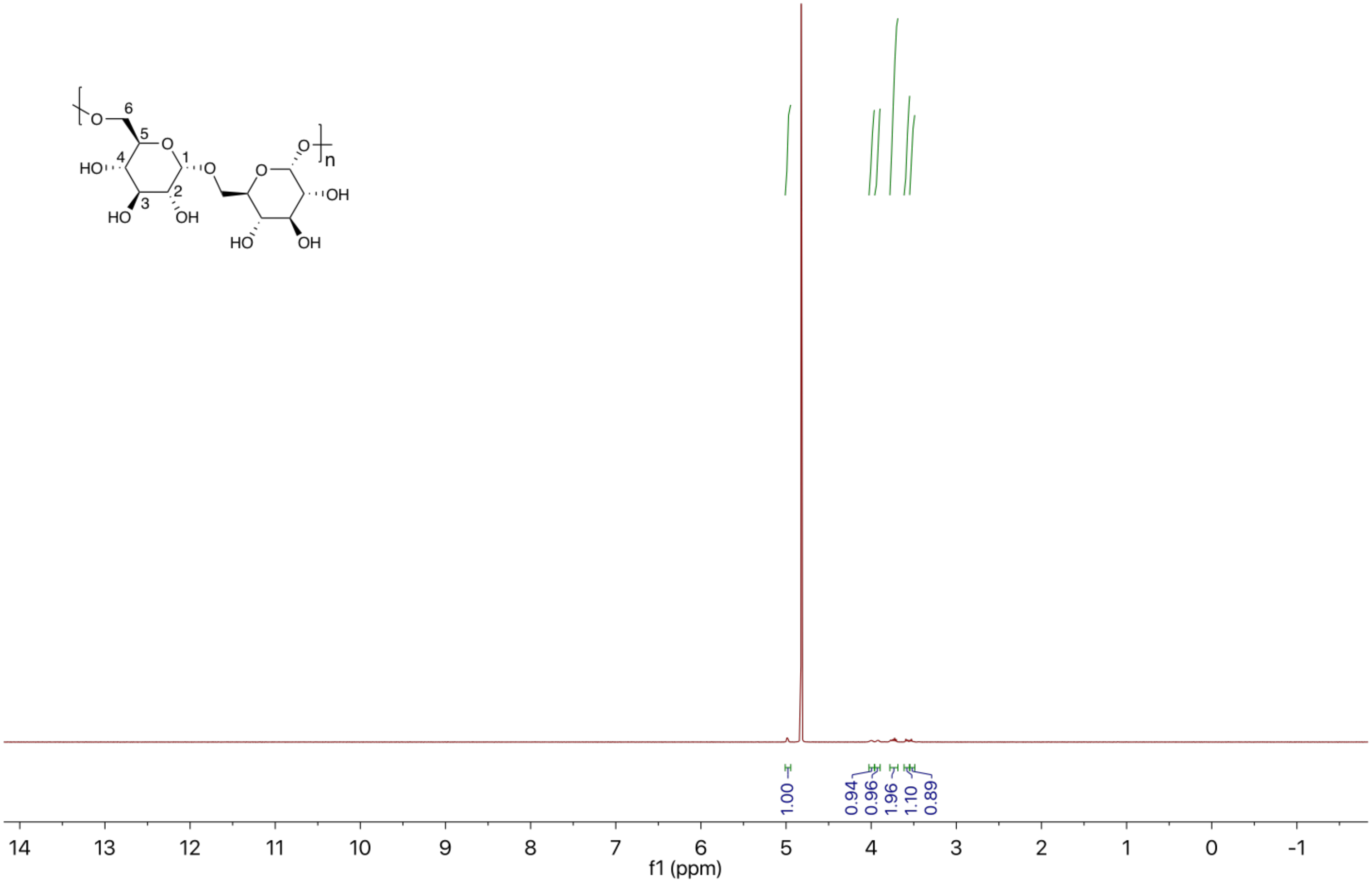

Figure A.9: *500 MHz ^{1}H-NMR Spectrum of Dextran in D_2O.*

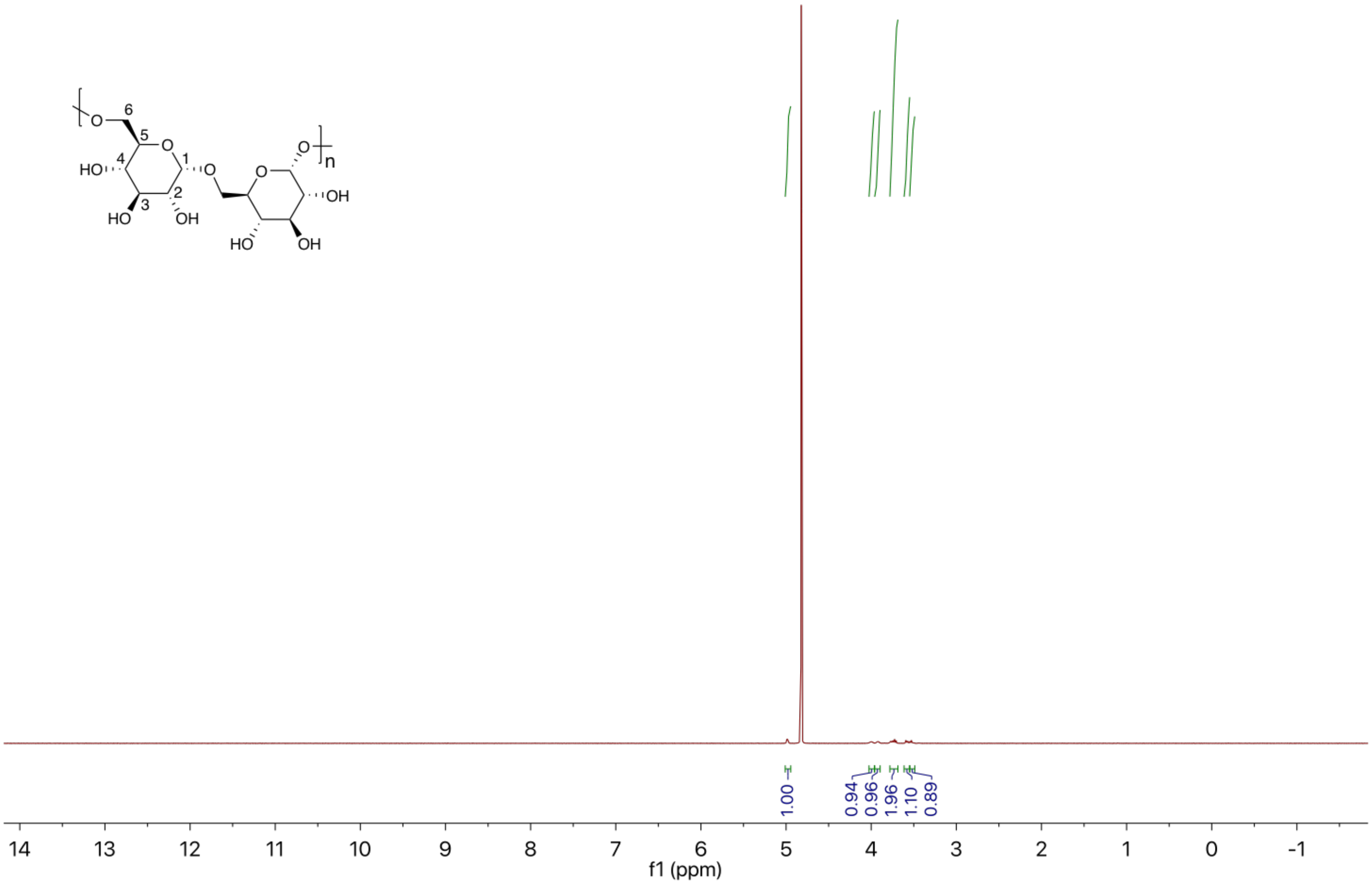

Figure A.10: *500 MHz ^{1}H-NMR Spectrum of Dextran in D_2O/DMSO-d6.*. Dextran recovered from Soxhlet Extraction.

APPENDIX B

SUPPLEMENTAL TEM MICROGRAPHS

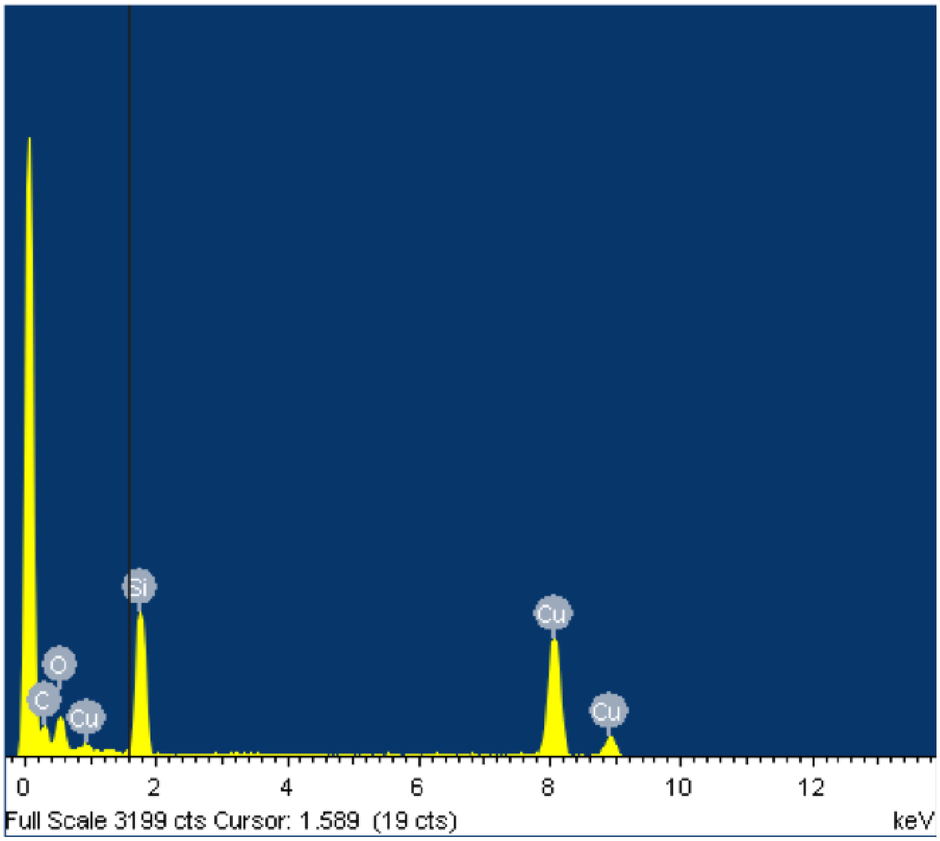

Figure B.1: *EDS Spectrum of Dex-SiO_2-NPs.*

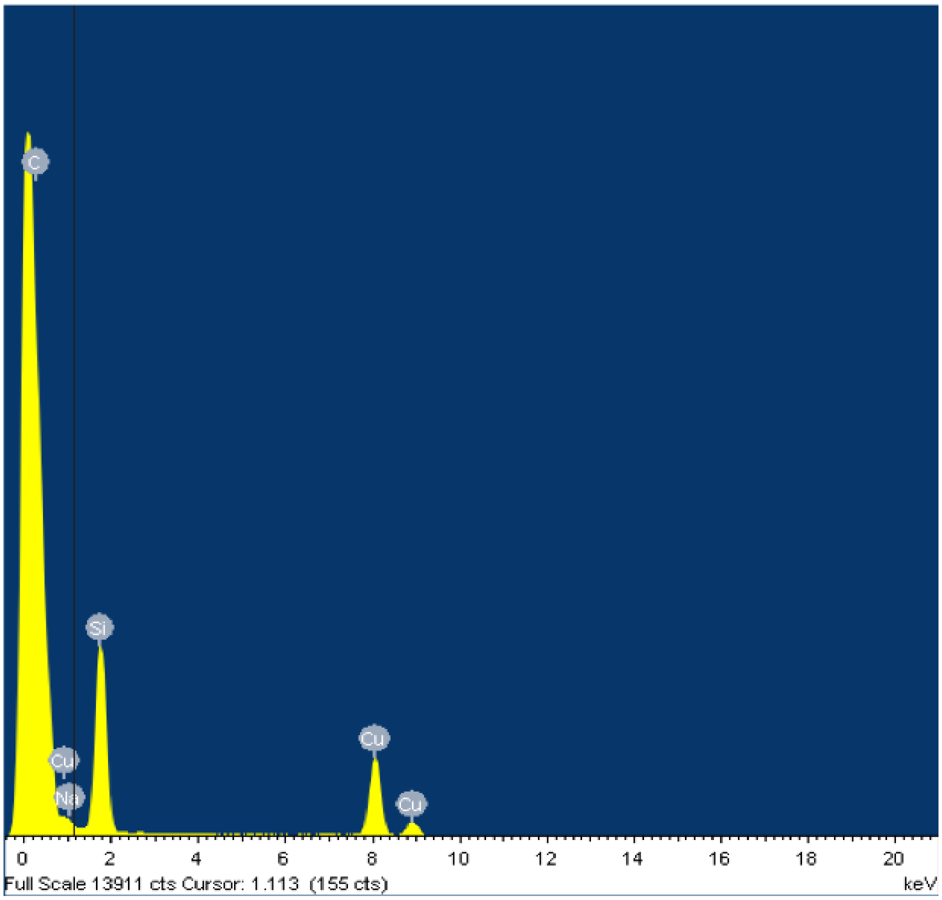

Figure B.2: *EDS Spectrum of* SiO_2*-NPs.*

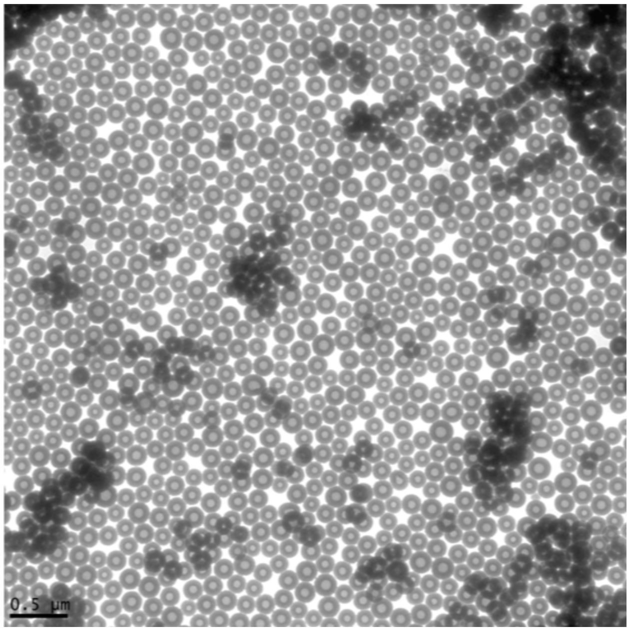

Figure B.3: *TEM Micrograph of Dex-SiO$_2$-NPs Prepared using 6 kDa Dextran and Dex-SiO$_2$-200 Conditions*. 14kx magnification, Scale bar 0.5 μm. Brightness enhanced by 20% to emphasize detail.

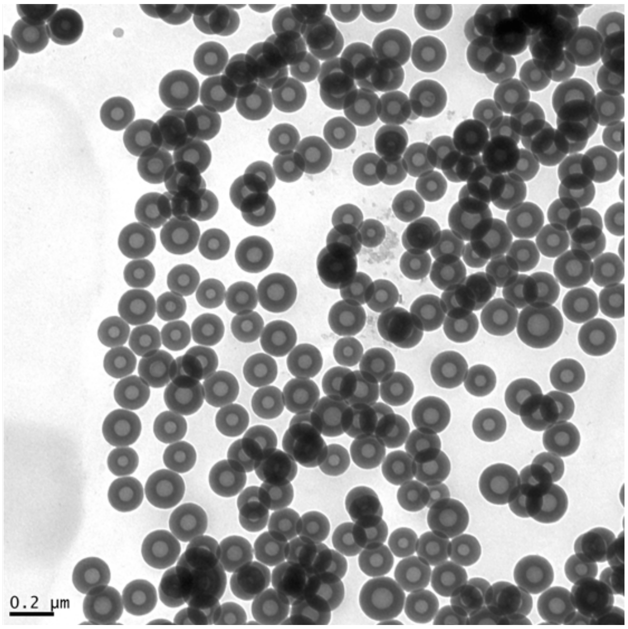

Figure B.4: *TEM Micrograph of Dex-SiO$_2$-NPs Prepared using 6 kDa Dextran and Dex-SiO$_2$-200 Conditions*. 27kx magnification, Scale bar 0.2 μm. Brightness enhanced by 20% to emphasize detail.

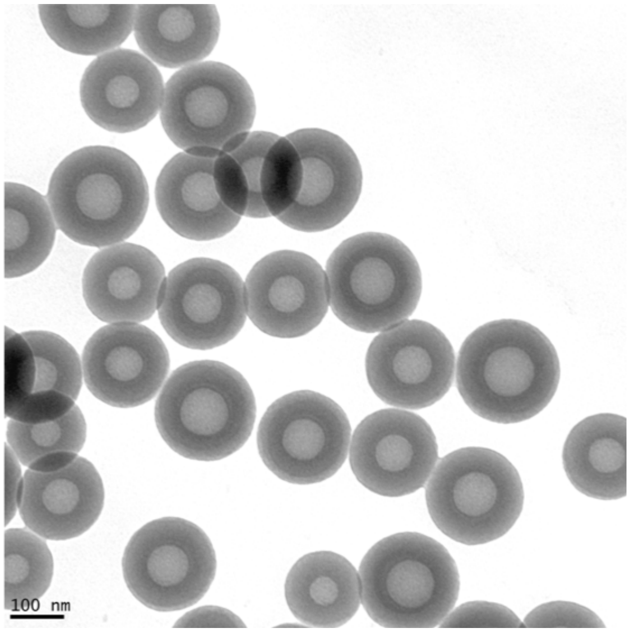

Figure B.5: *TEM Micrograph of Dex-SiO$_2$-NPs Prepared using 6 kDa Dextran and Dex-SiO$_2$-200 Conditions*. 67kx magnification, Scale bar 100 nm. Brightness enhanced by 20% to emphasize detail.

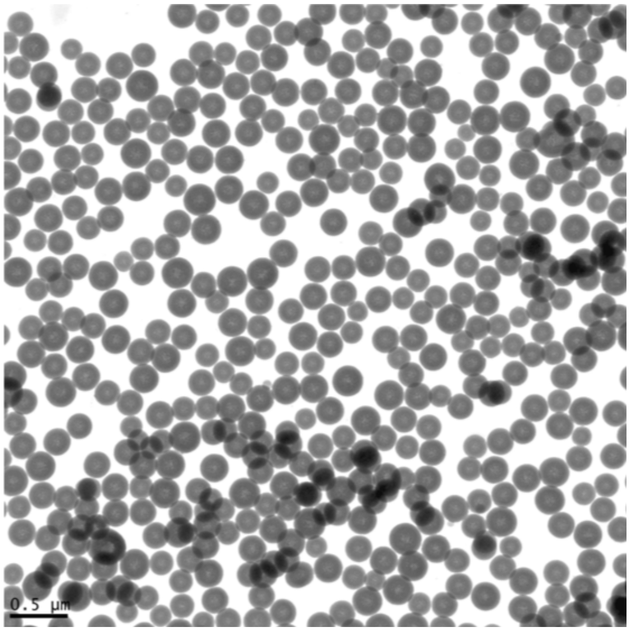

Figure B.6: *TEM Micrograph of Dex-SiO$_2$-NPs Prepared using 6 kDa Dextran and Dex-SiO$_2$-250 Conditions*. 14kx magnification, Scale bar 0.5 μm. Brightness enhanced by 20% to emphasize detail.

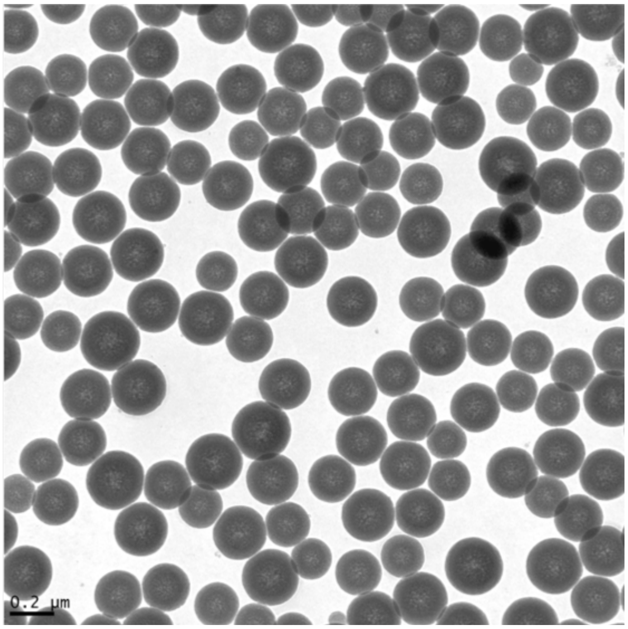

Figure B.7: *TEM Micrograph of Dex-SiO_2-NPs Prepared using 6 kDa Dextran and Dex-SiO_2-250 Conditions*. 27kx magnification, Scale bar 0.2 μm. Brightness enhanced by 20% to emphasize detail.

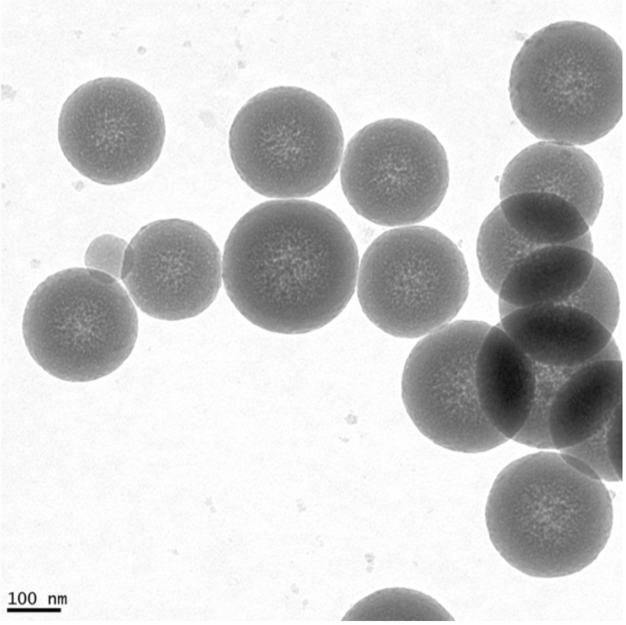

Figure B.8: *TEM Micrograph of Dex-SiO_2-NPs Prepared using 6 kDa Dextran and Dex-SiO_2-250 Conditions*. 67kx magnification, Scale bar 100 nm. Brightness enhanced by 20% to emphasize detail.

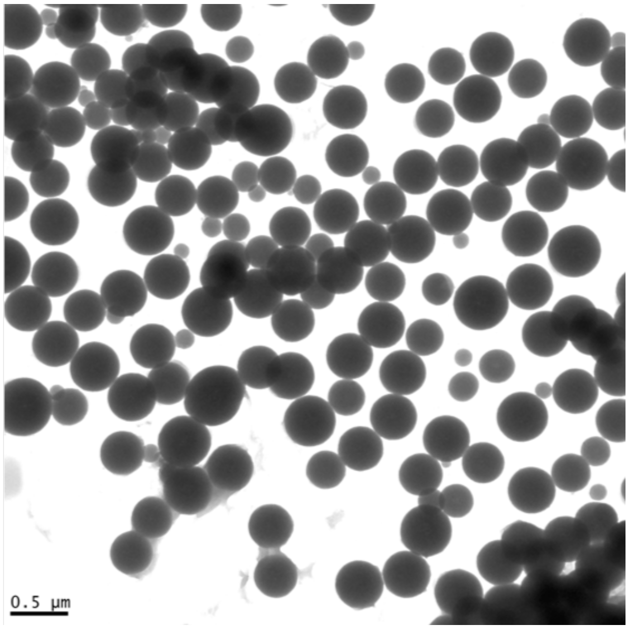

Figure B.9: *TEM Micrograph of Dex-SiO_2-NPs Prepared using 6 kDa Dextran and Dex-SiO_2-350 Conditions*. 14kx magnification, Scale bar 0.5 μm. Brightness enhanced by 20% to emphasize detail.

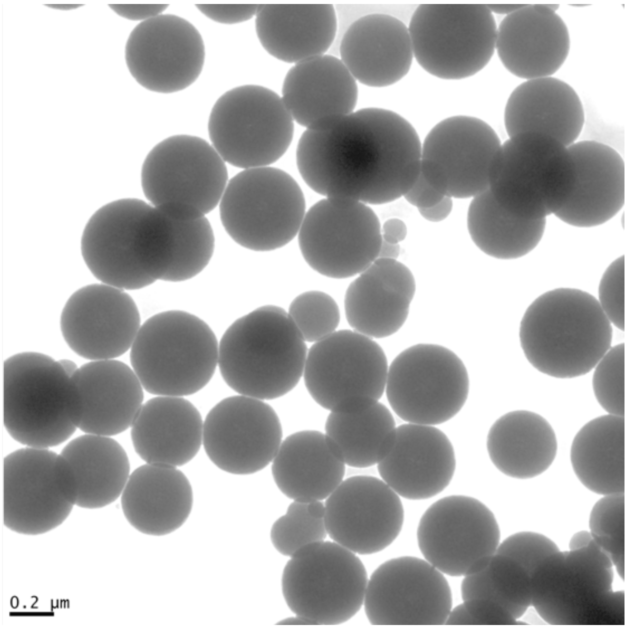

Figure B.10: *TEM Micrograph of Dex-SiO_2-NPs Prepared using 6 kDa Dextran and Dex-SiO_2-350 Conditions*. 27kx magnification, Scale bar 0.2 μm. Brightness enhanced by 20% to emphasize detail.

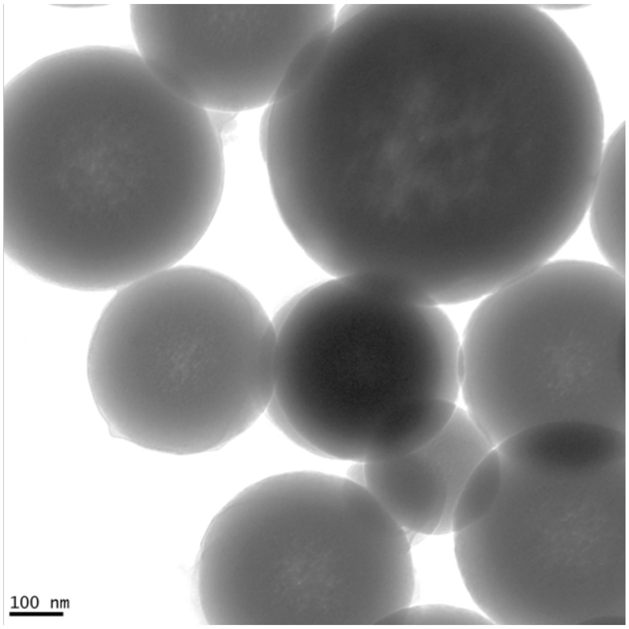

Figure B.11: *TEM Micrograph of Dex-SiO_2-NPs Prepared using 6 kDa Dextran and Dex-SiO_2-350 Conditions*. 67kx magnification, Scale bar 100 nm. Brightness enhanced by 20% to emphasize detail.

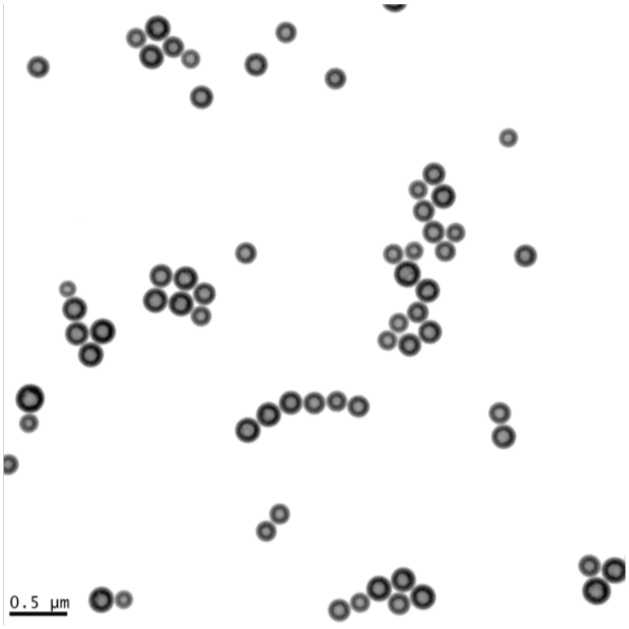

Figure B.12: *TEM Micrograph of Dex-SiO$_2$-NPs Prepared using 9-11 kDa Dextran and Dex-SiO$_2$-200 Conditions*. 14kx magnification, Scale bar 0.5 μm. Brightness enhanced by 20% to emphasize detail.

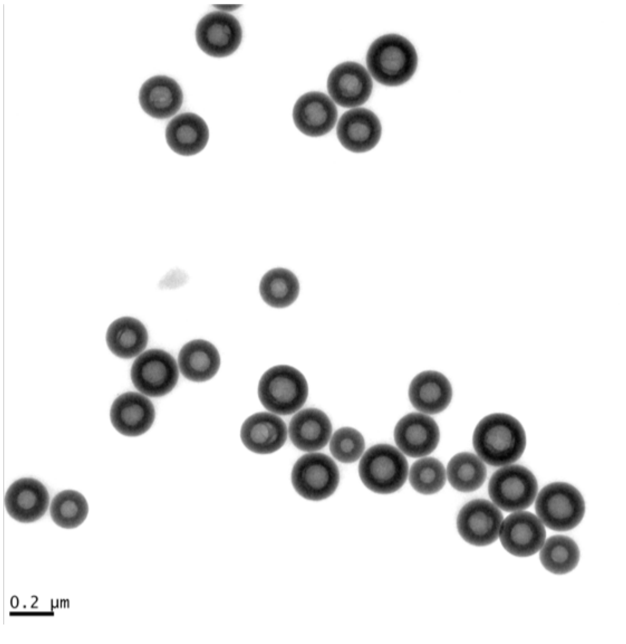

Figure B.13: *TEM Micrograph of Dex-SiO$_2$-NPs Prepared using 9-11 kDa Dextran and Dex-SiO$_2$-200 Conditions*. 27kx magnification, Scale bar 0.2 μm. Brightness enhanced by 20% to emphasize detail.

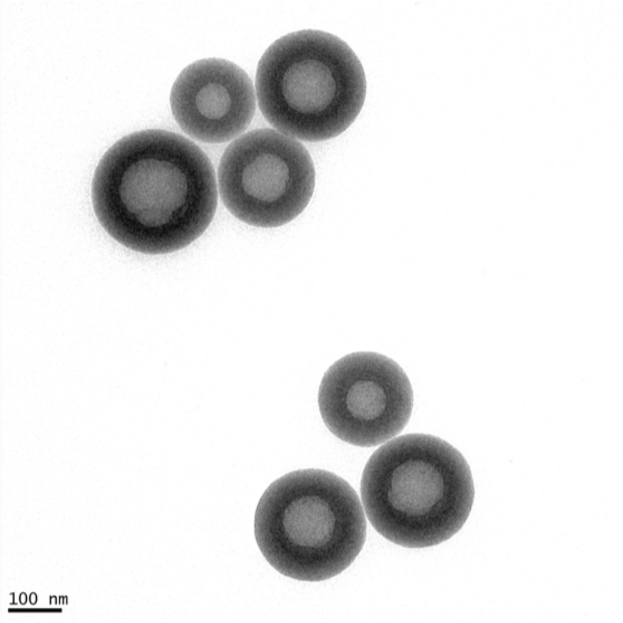

Figure B.14: *TEM Micrograph of Dex-SiO_2-NPs Prepared using 9-11 kDa Dextran and Dex-SiO_2-200 Conditions*. 67kx magnification, Scale bar 100 nm. Brightness enhanced by 20% to emphasize detail.

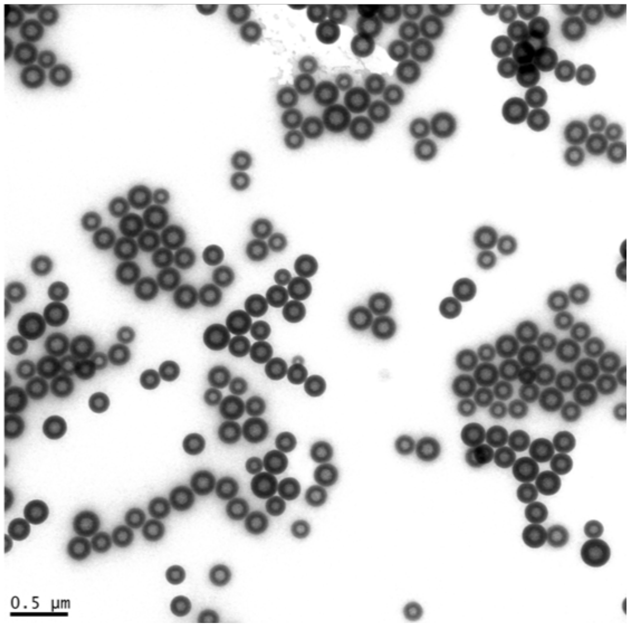

Figure B.15: *TEM Micrograph of Dex-SiO_2-NPs Prepared using 9-11 kDa Dextran and Dex-SiO_2-250 Conditions*. 14kx magnification, Scale bar 0.5 μm. Brightness enhanced by 20% to emphasize detail.

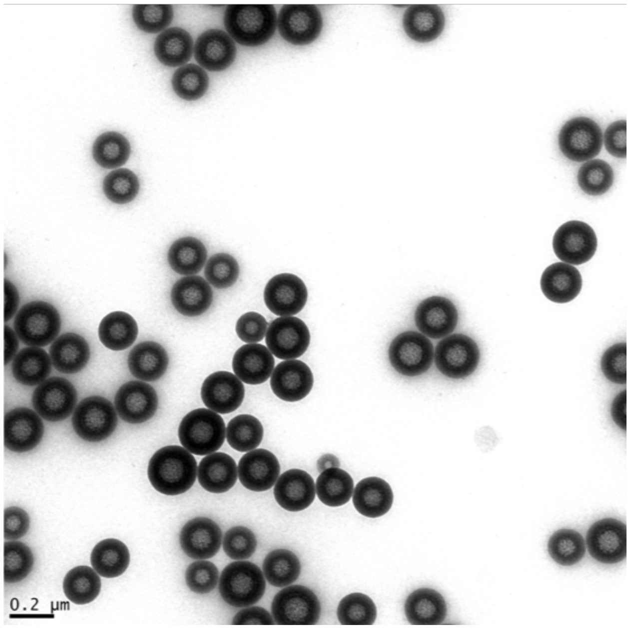

Figure B.16: *TEM Micrograph of Dex-SiO$_2$-NPs Prepared using 9-11 kDa Dextran and Dex-SiO$_2$-250 Conditions*. 27kx magnification, Scale bar 0.2 μm. Brightness enhanced by 20% to emphasize detail.

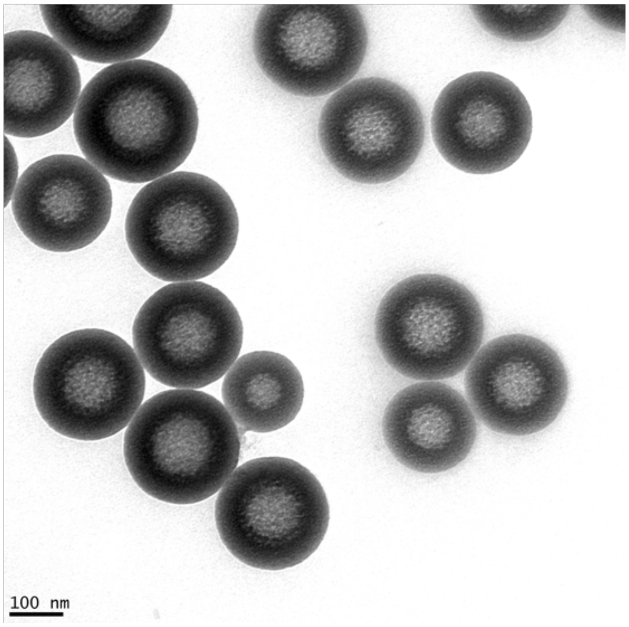

Figure B.17: *TEM Micrograph of Dex-SiO$_2$-NPs Prepared using 9-11 kDa Dextran and Dex-SiO$_2$-250 Conditions*. 67kx magnification, Scale bar 100 nm. Brightness enhanced by 20% to emphasize detail.

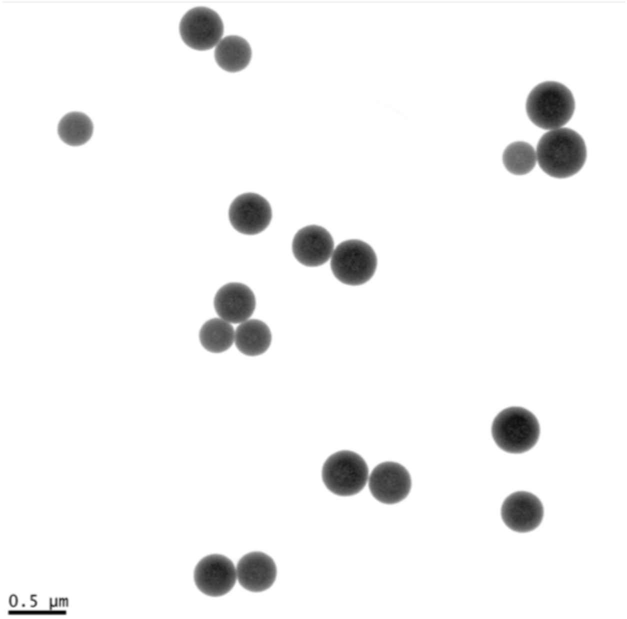

Figure B.18: *TEM Micrograph of Dex-SiO$_2$-NPs Prepared using 9-11 kDa Dextran and Dex-SiO$_2$-350 Conditions*. 14kx magnification, Scale bar 0.5 μm. Brightness enhanced by 20% to emphasize detail.

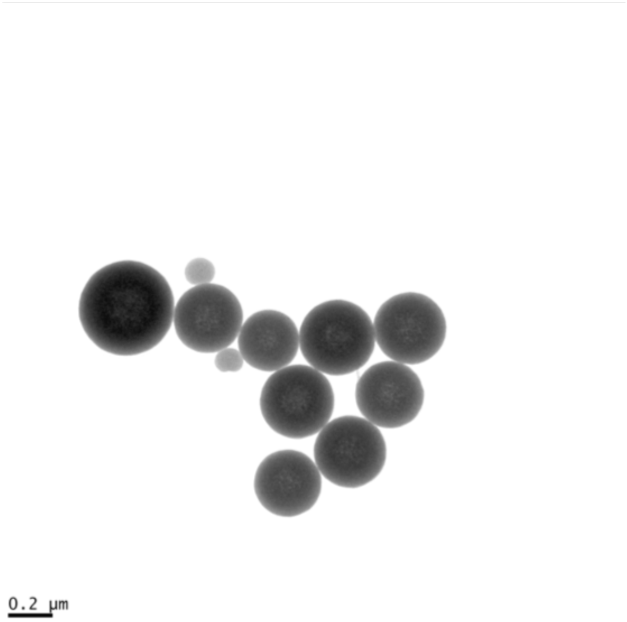

Figure B.19: *TEM Micrograph of Dex-SiO$_2$-NPs Prepared using 9-11 kDa Dextran and Dex-SiO$_2$-350 Conditions*. 27kx magnification, Scale bar 0.2 μm. Brightness enhanced by 20% to emphasize detail.

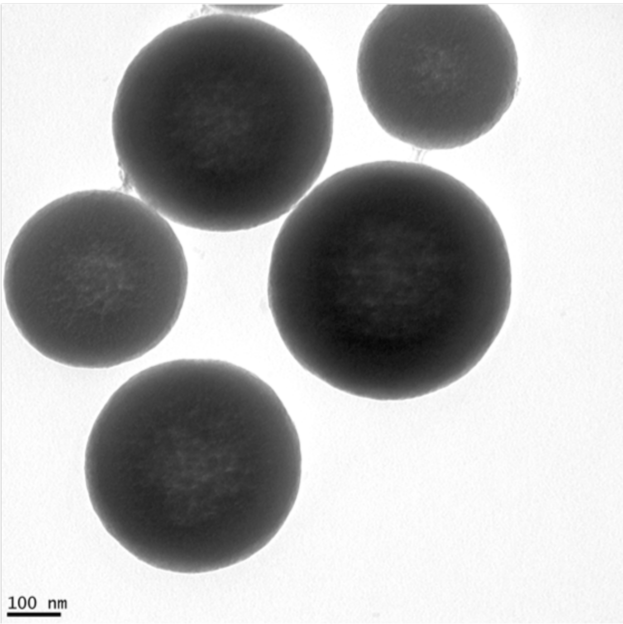

Figure B.20: *TEM Micrograph of Dex-SiO_2-NPs Prepared using 9-11 kDa Dextran and Dex-SiO_2-350 Conditions*. 67kx magnification, Scale bar 100 nm. Brightness enhanced by 20% to emphasize detail.

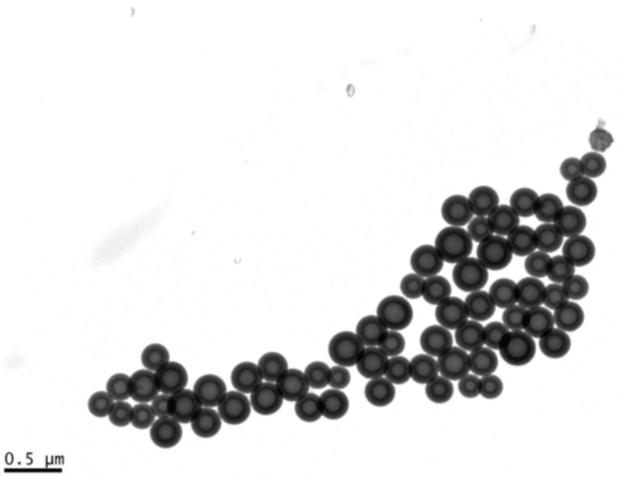

Figure B.21: *TEM Micrograph of Calcined Dex-SiO$_2$-NPs Prepared using 9-11 kDa Dextran and Dex-SiO$_2$-200 Conditions* . 14kx magnification, Scale bar 0.5 μm. Brightness enhanced by 20% to emphasize detail.

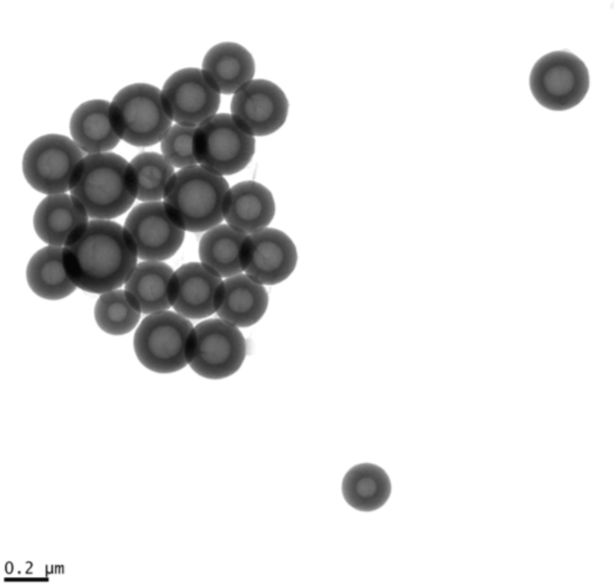

Figure B.22: *TEM Micrograph of Calcined Dex-SiO$_2$-NPs Prepared using 9-11 kDa Dextran and Dex-SiO$_2$-200 Conditions*. 27kx magnification, Scale bar 0.2 μm. Brightness enhanced by 20% to emphasize detail.

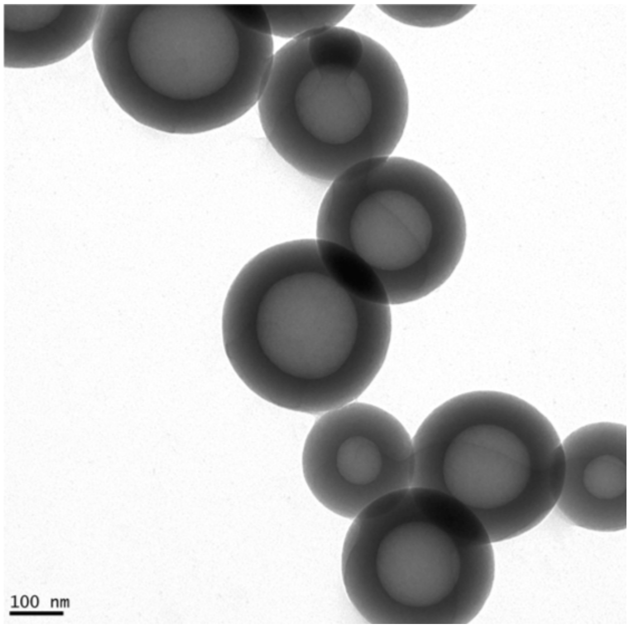

Figure B.23: *TEM Micrograph of Calcined Dex-SiO_2-NPs Prepared using 9-11 kDa Dextran and Dex-SiO_2-200 Conditions*. 67kx magnification, Scale bar 100 nm. Brightness enhanced by 20% to emphasize detail.

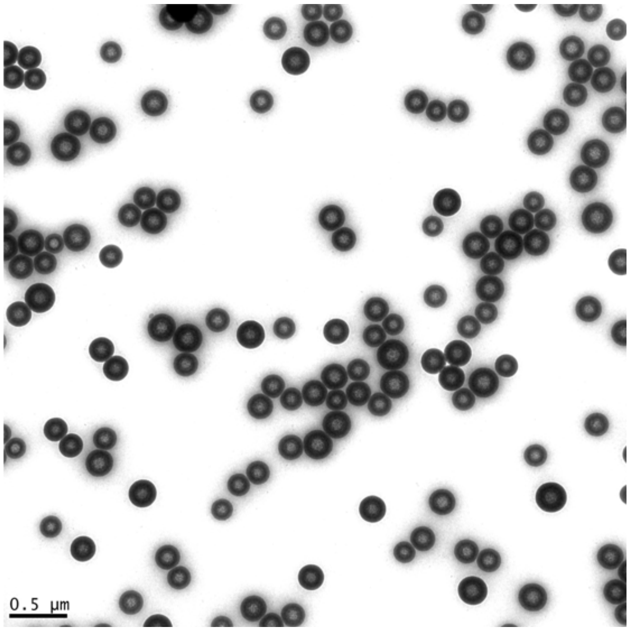

Figure B.24: *TEM Micrograph of Calcined Dex-SiO_2-NPs Prepared using 9-11 kDa Dextran and Dex-SiO_2-250 Conditions*. 14kx magnification, Scale bar 0.5 μm. Brightness enhanced by 20% to emphasize detail.

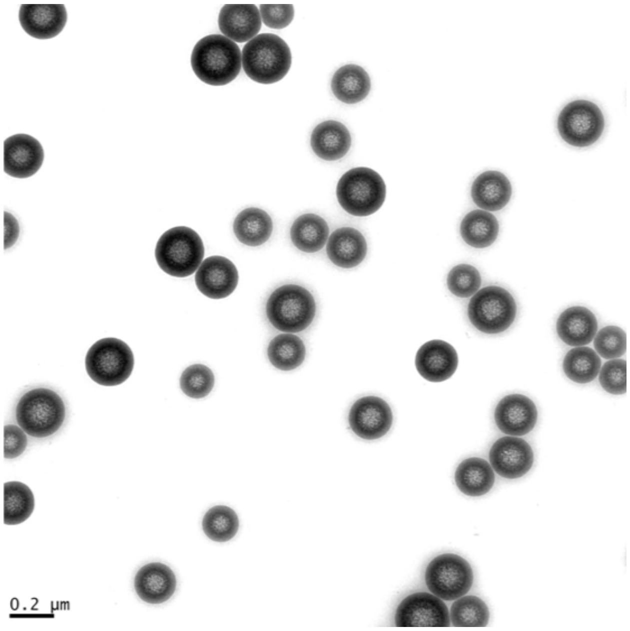

Figure B.25: *TEM Micrograph of Calcined Dex-SiO_2-NPs Prepared using 9-11 kDa Dextran and Dex-SiO_2-250 Conditions*. 27kx magnification, Scale bar 0.2 μm. Brightness enhanced by 20% to emphasize detail.

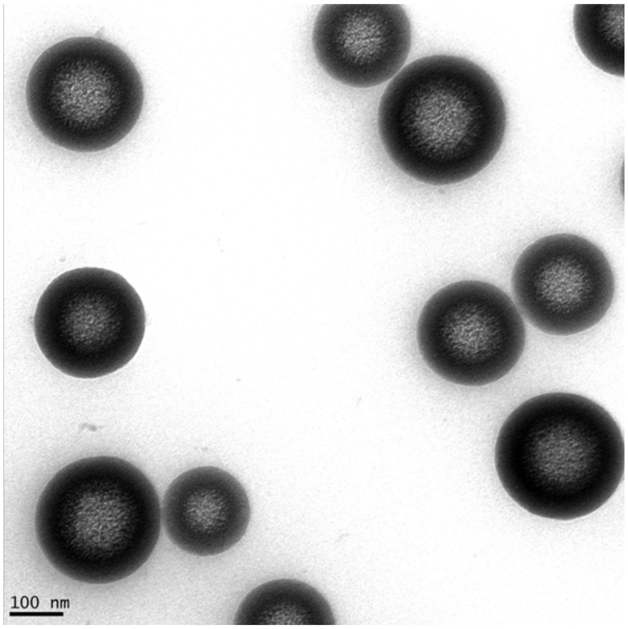

Figure B.26: *TEM Micrograph of Calcined Dex-SiO_2-NPs Prepared using 9-11 kDa Dextran and Dex-SiO_2-250 Conditions*. 67kx magnification, Scale bar 100 nm. Brightness enhanced by 20% to emphasize detail.

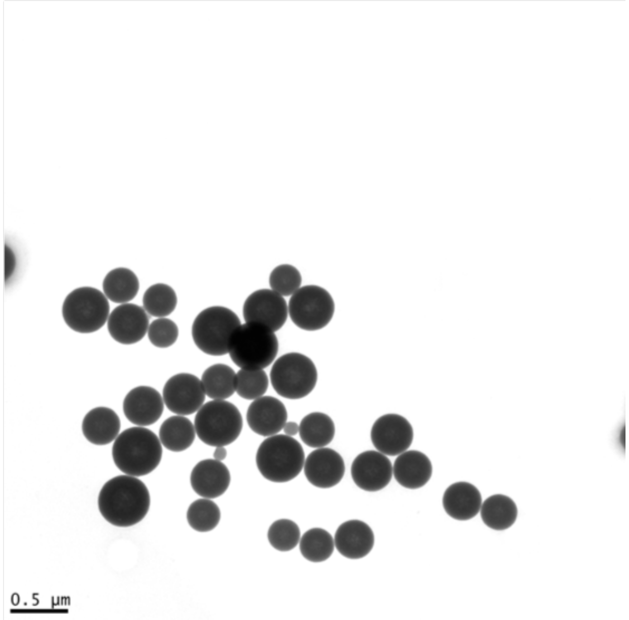

Figure B.27: *TEM Micrograph of Calcined Dex-SiO$_2$-NPs Prepared using 9-11 kDa Dextran and Dex-SiO$_2$-350 Conditions*. 14kx magnification, Scale bar 0.5 μm. Brightness enhanced by 20% to emphasize detail.

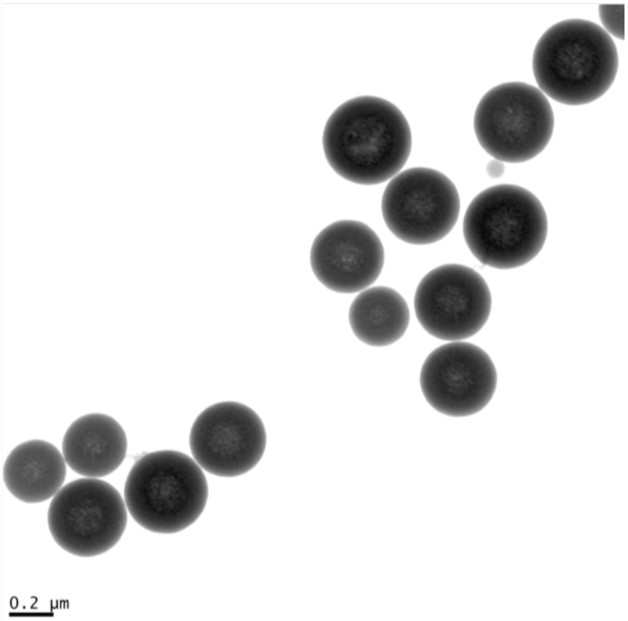

Figure B.28: *TEM Micrograph of Calcined Dex-SiO$_2$-NPs Prepared using 9-11 kDa Dextran and Dex-SiO$_2$-350 Conditions*. 27kx magnification, Scale bar 0.2 μm. Brightness enhanced by 20% to emphasize detail.

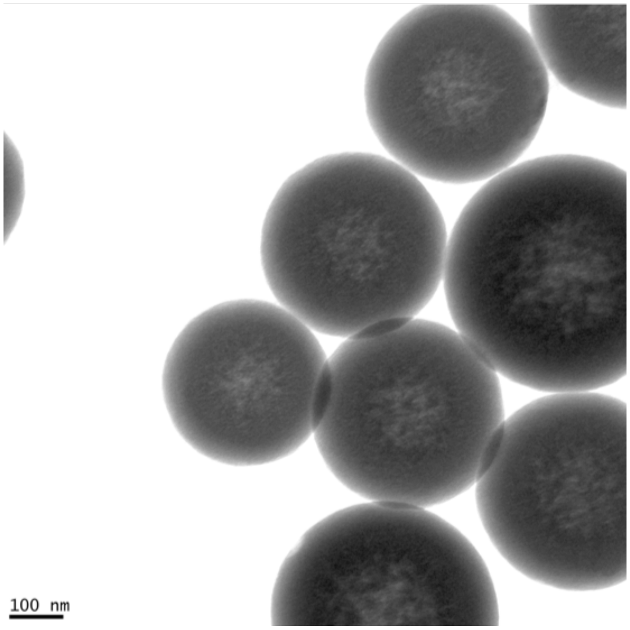

Figure B.29: *TEM Micrograph of Calcined Dex-SiO_2-NPs Prepared using 9-11 kDa Dextran and Dex-SiO_2-350 Conditions*. 67kx magnification, Scale bar 100 nm. Brightness enhanced by 20% to emphasize detail.

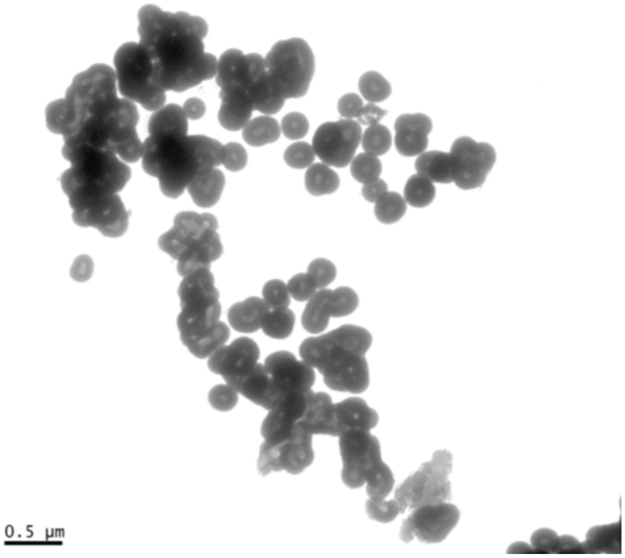

Figure B.30: *TEM Micrograph of Dex-SiO$_2$-NPs Prepared using 40 kDa Dextran and Dex-SiO$_2$-200 Conditions*. 14kx magnification, Scale bar 0.5 μm. Brightness enhanced by 20% to emphasize detail.

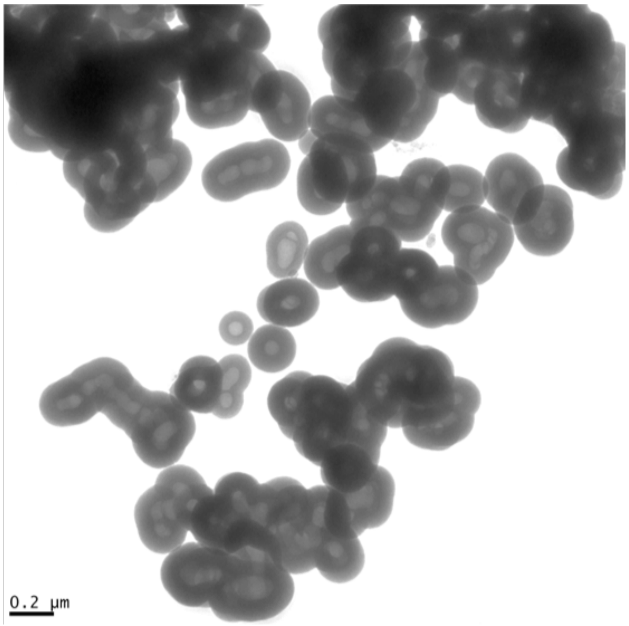

Figure B.31: *TEM Micrograph of Dex-SiO$_2$-NPs Prepared using 40 kDa Dextran and Dex-SiO$_2$-200 Conditions*. 27kx magnification, Scale bar 0.2 μm. Brightness enhanced by 20% to emphasize detail.

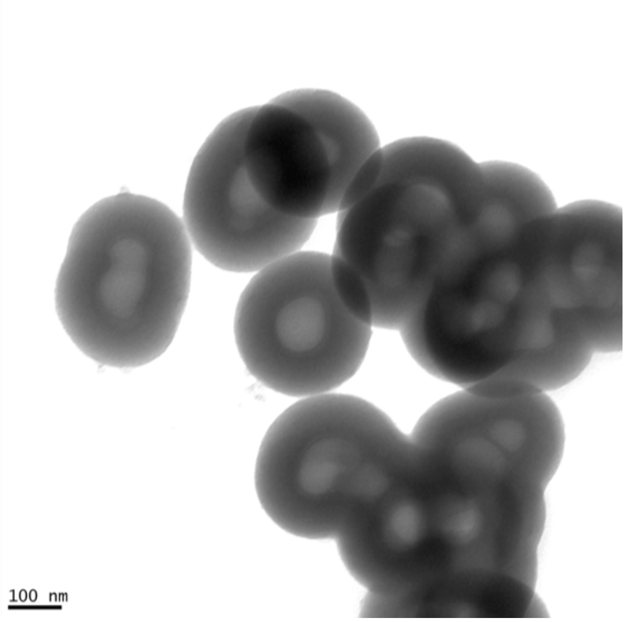

Figure B.32: *TEM Micrograph of Dex-SiO$_2$-NPs Prepared using 40 kDa Dextran and Dex-SiO$_2$-200 Conditions*. 67kx magnification, Scale bar 100 nm. Brightness enhanced by 20% to emphasize detail.

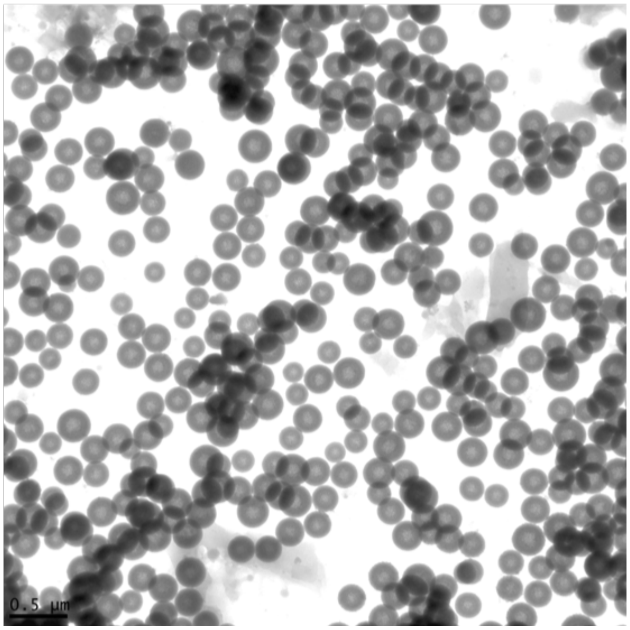

Figure B.33: *TEM Micrograph of Dex-SiO$_2$-NPs Prepared using 40 kDa Dextran and Dex-SiO$_2$-250 Conditions*. 14kx magnification, Scale bar 0.5 μm. Brightness enhanced by 20% to emphasize detail.

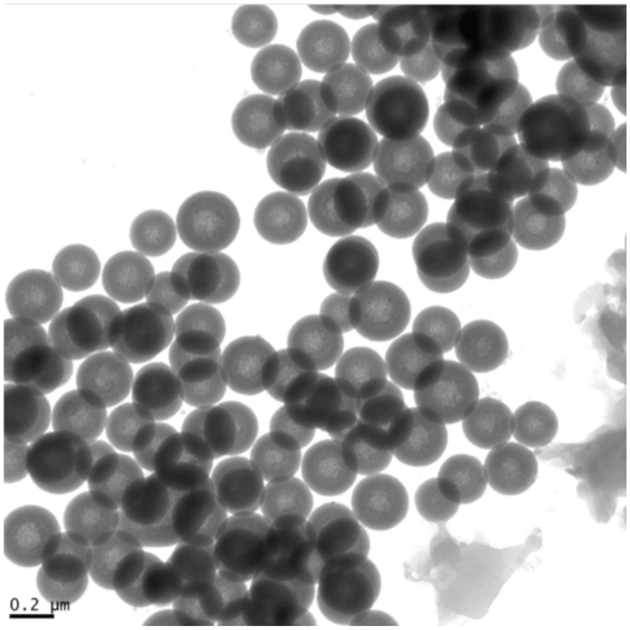

Figure B.34: *TEM Micrograph of Dex-SiO$_2$-NPs Prepared using 40 kDa Dextran and Dex-SiO$_2$-250 Conditions*. 27kx magnification, Scale bar 0.2 μm. Brightness enhanced by 20% to emphasize detail.

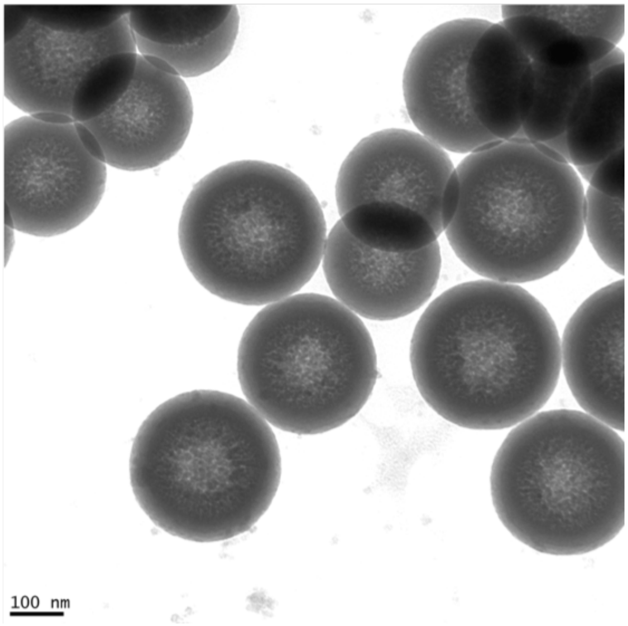

Figure B.35: *TEM Micrograph of Dex-SiO$_2$-NPs Prepared using 40 kDa Dextran and Dex-SiO$_2$-250 Conditions*. 67kx magnification, Scale bar 100 nm. Brightness enhanced by 20% to emphasize detail.

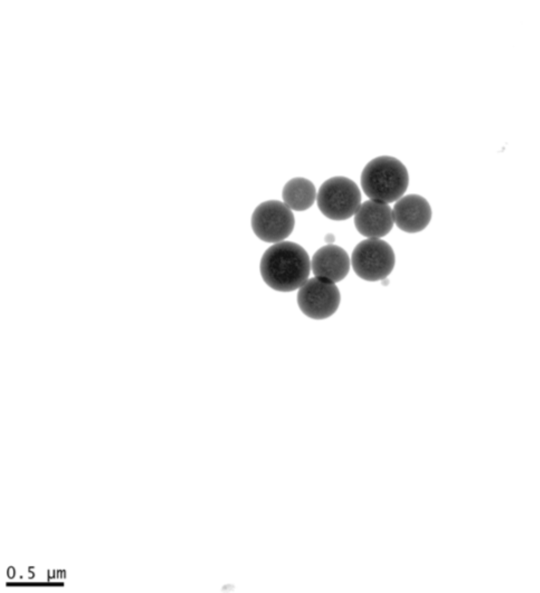

Figure B.36: *TEM Micrograph of Dex-SiO$_2$-NPs Prepared using 40 kDa Dextran and Dex-SiO$_2$-350 Conditions*. 14kx magnification, Scale bar 0.5 μm. Brightness enhanced by 20% to emphasize detail.

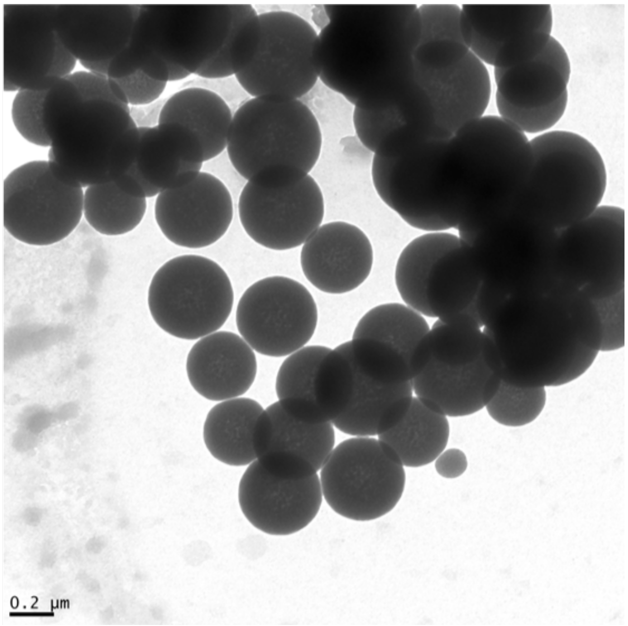

Figure B.37: *TEM Micrograph of Dex-SiO$_2$-NPs Prepared using 40 kDa Dextran and Dex-SiO$_2$-350 Conditions*. 27kx magnification, Scale bar 0.2 μm. Brightness enhanced by 20% to emphasize detail.

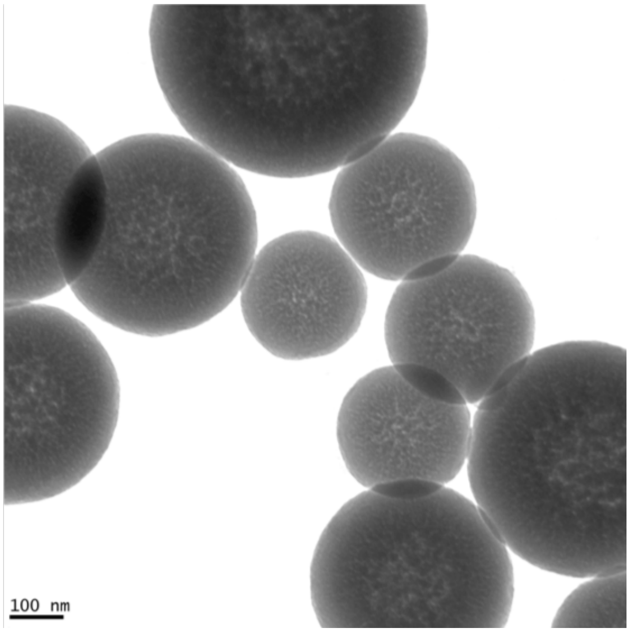

Figure B.38: *TEM Micrograph of Dex-SiO_2-NPs Prepared using 40 kDa Dextran and Dex-SiO_2-350 Conditions*. 67kx magnification, Scale bar 100 nm. Brightness enhanced by 20% to emphasize detail.

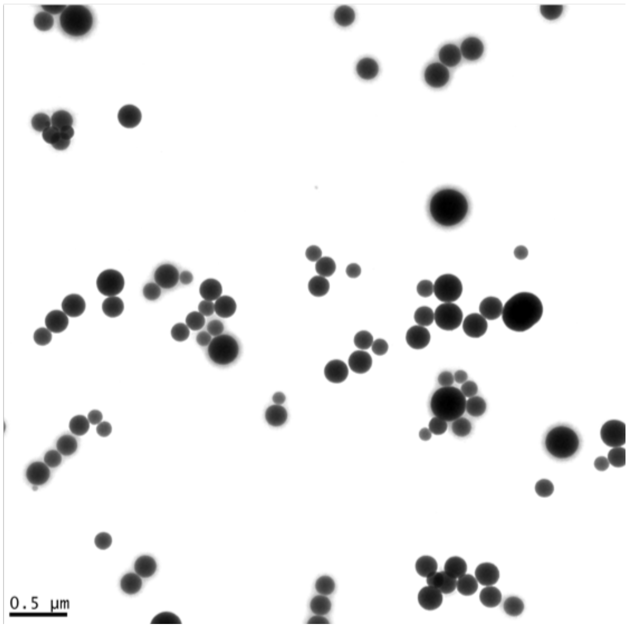

Figure B.39: *TEM Micrograph of Dex-SiO$_2$-NPs Prepared using α-cyclodextrin and Dex-SiO$_2$-200 Conditions*. 14kx magnification, Scale bar 0.5 μm. Brightness enhanced by 20% to emphasize detail.

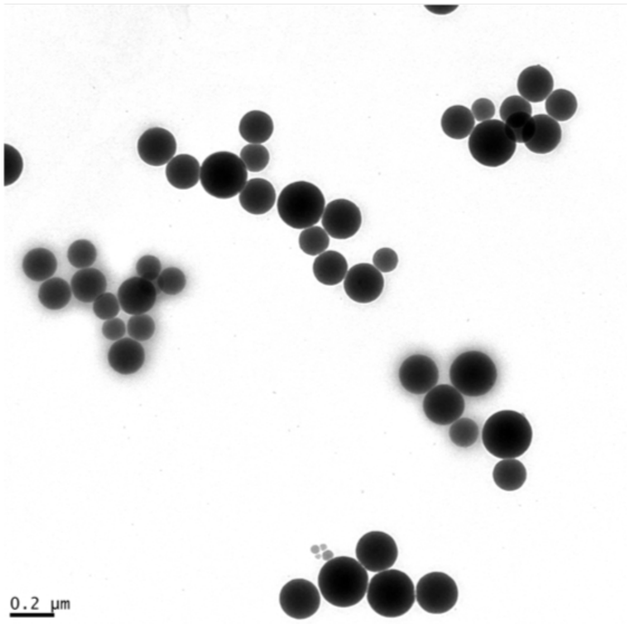

Figure B.40: *TEM Micrograph of Dex-SiO$_2$-NPs Prepared using α-cyclodextrin and Dex-SiO$_2$-200 Conditions*. 27kx magnification, Scale bar 0.2 μm. Brightness enhanced by 20% to emphasize detail.

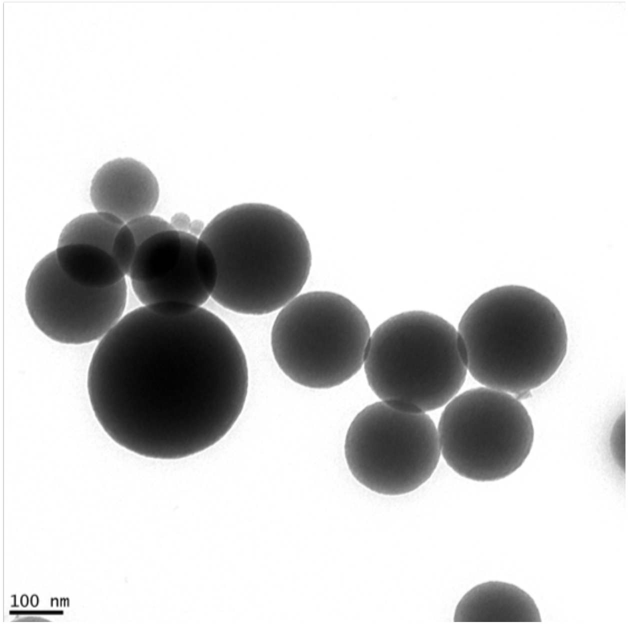

Figure B.41: *TEM Micrograph of Dex-SiO$_2$-NPs Prepared using α-cyclodextrin and Dex-SiO$_2$-200 Conditions*. 67kx magnification, Scale bar 100 nm. Brightness enhanced by 20% to emphasize detail.

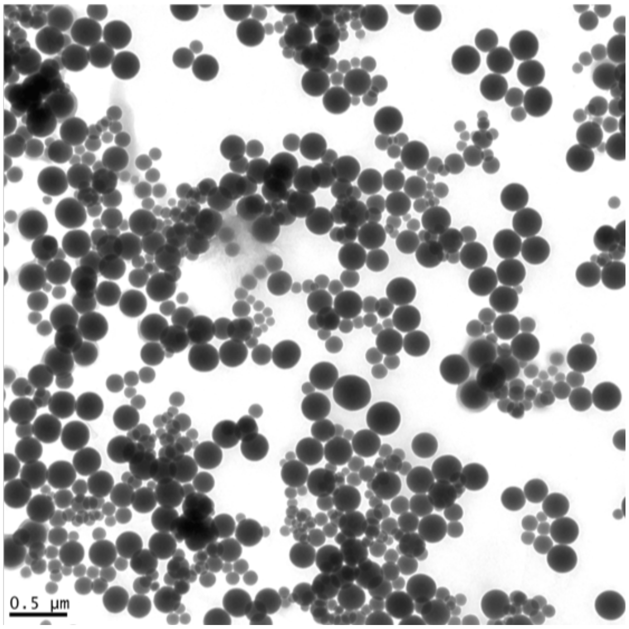

Figure B.42: *TEM Micrograph of Dex-SiO$_2$-NPs Prepared using α-cyclodextrin and Dex-SiO$_2$-250 Conditions*. 14kx magnification, Scale bar 0.5 μm. Brightness enhanced by 20% to emphasize detail.

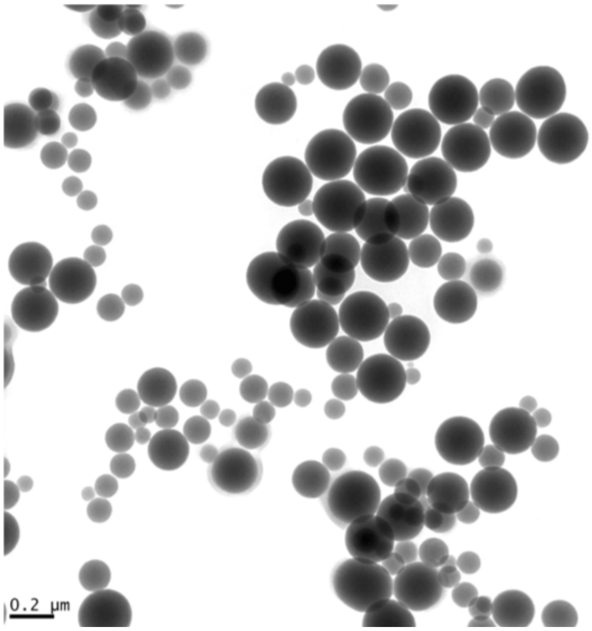

Figure B.43: *TEM Micrograph of Dex-SiO$_2$-NPs Prepared using α-cyclodextrin and Dex-SiO$_2$-250 Conditions*. 27kx magnification, Scale bar 0.2 μm. Brightness enhanced by 20% to emphasize detail.

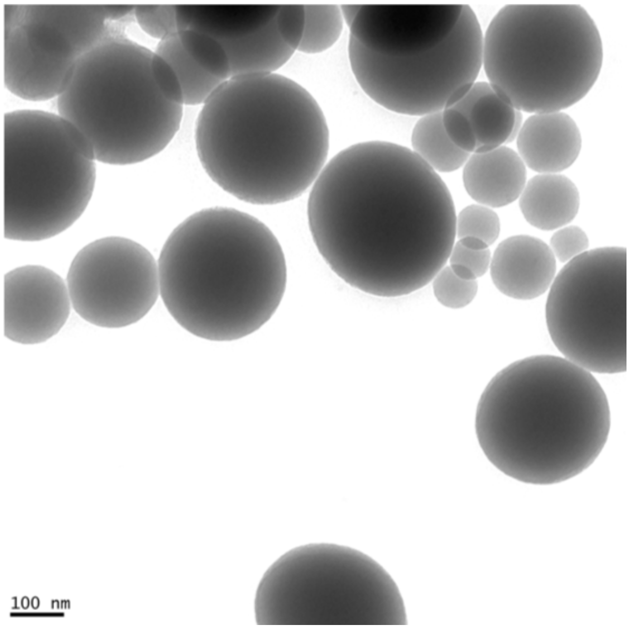

Figure B.44: *TEM Micrograph of Dex-SiO$_2$-NPs Prepared using α-cyclodextrin and Dex-SiO$_2$-250 Conditions*. 67kx magnification, Scale bar 100 nm. Brightness enhanced by 20% to emphasize detail.

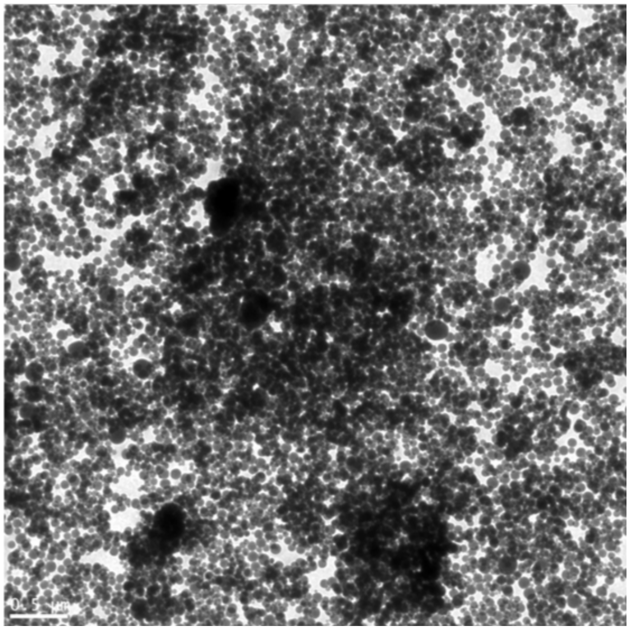

Figure B.45: *TEM Micrograph of Dex-SiO$_2$-NPs Prepared using α-cyclodextrin and Dex-SiO$_2$-350 Conditions*. 14kx magnification, Scale bar 0.5 μm. Brightness enhanced by 20% to emphasize detail.

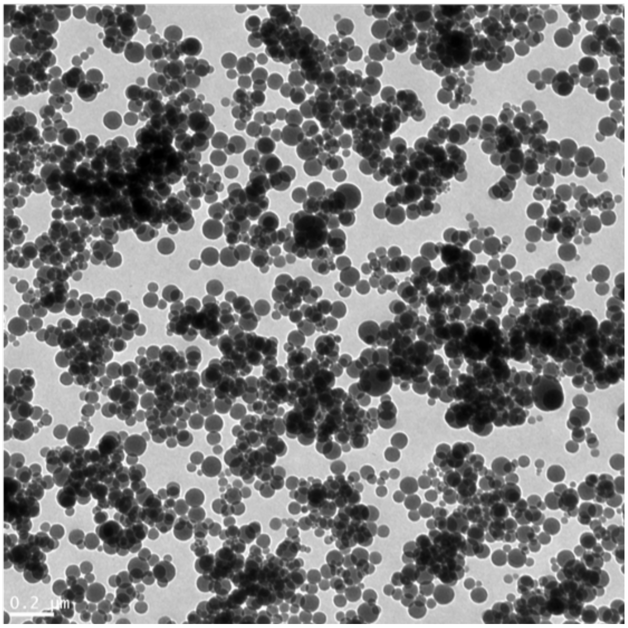

Figure B.46: *TEM Micrograph of Dex-SiO$_2$-NPs Prepared using α-cyclodextrin and Dex-SiO$_2$-350 Conditions*. 27kx magnification, Scale bar 0.2 μm. Brightness enhanced by 20% to emphasize detail.

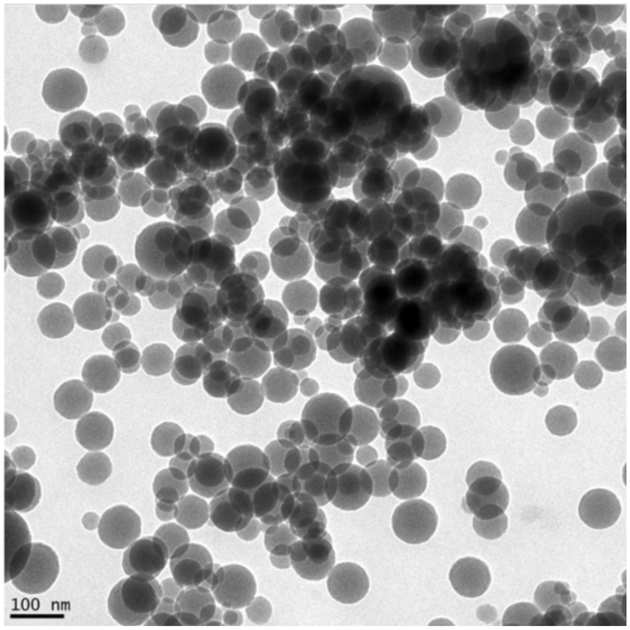

Figure B.47: *TEM Micrograph of Dex-SiO$_2$-NPs Prepared using α-cyclodextrin and Dex-SiO$_2$-350 Conditions*. 67kx magnification, Scale bar 100 nm. Brightness enhanced by 20% to emphasize detail.

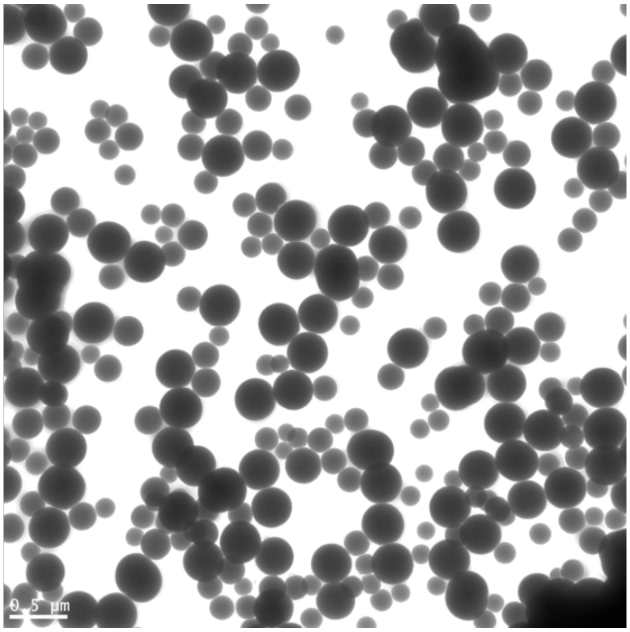

Figure B.48: *TEM Micrograph of Dex-SiO$_2$-NPs Prepared using β-cyclodextrin and Dex-SiO$_2$-200 Conditions*. 14kx magnification, Scale bar 0.5 μm. Brightness enhanced by 20% to emphasize detail.

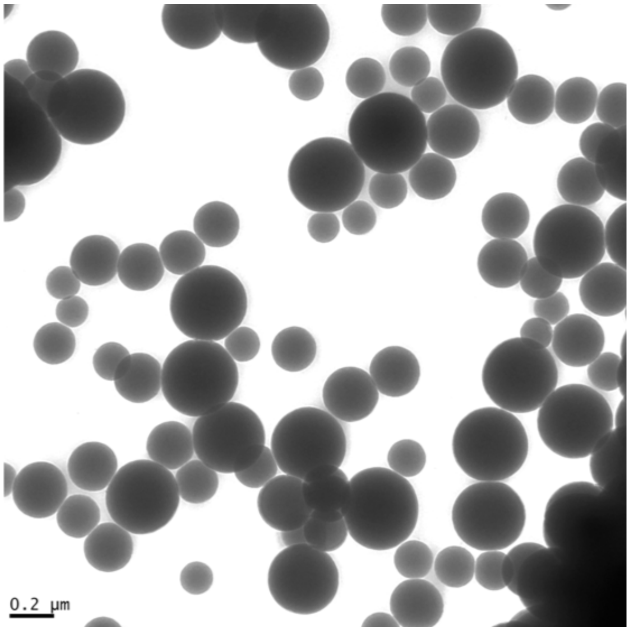

Figure B.49: *TEM Micrograph of Dex-SiO$_2$-NPs Prepared using β-cyclodextrin and Dex-SiO$_2$-200 Conditions*. 27kx magnification, Scale bar 0.2 μm. Brightness enhanced by 20% to emphasize detail.

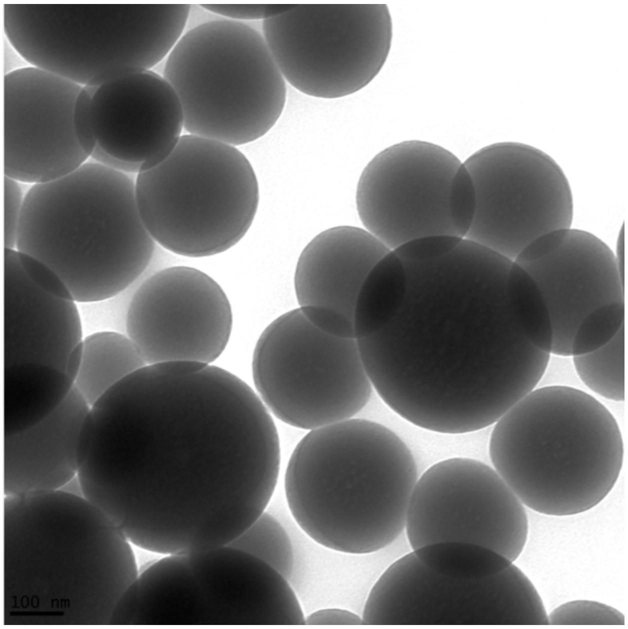

Figure B.50: *TEM Micrograph of Dex-SiO_2-NPs Prepared using β-cyclodextrin and Dex-SiO_2-200 Conditions*. 67kx magnification, Scale bar 100 nm. Brightness enhanced by 20% to emphasize detail.

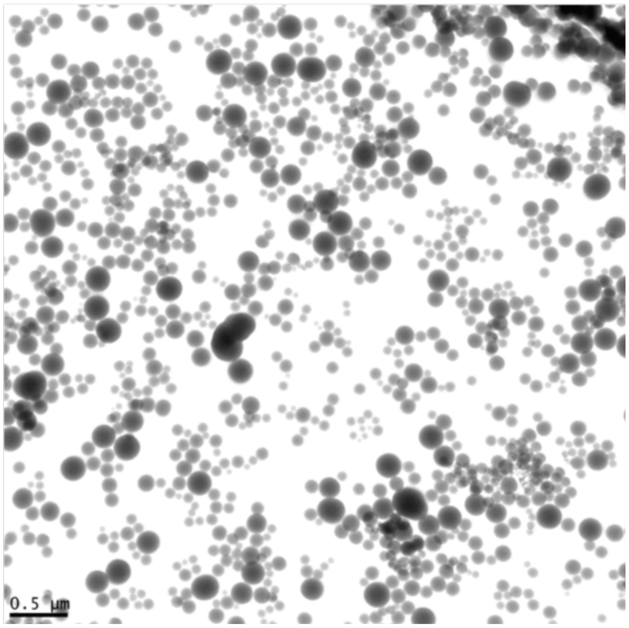

Figure B.51: *TEM Micrograph of Dex-SiO_2-NPs Prepared using β-cyclodextrin and Dex-SiO_2-250 Conditions*. 14kx magnification, Scale bar 0.5 μm. Brightness enhanced by 20% to emphasize detail.

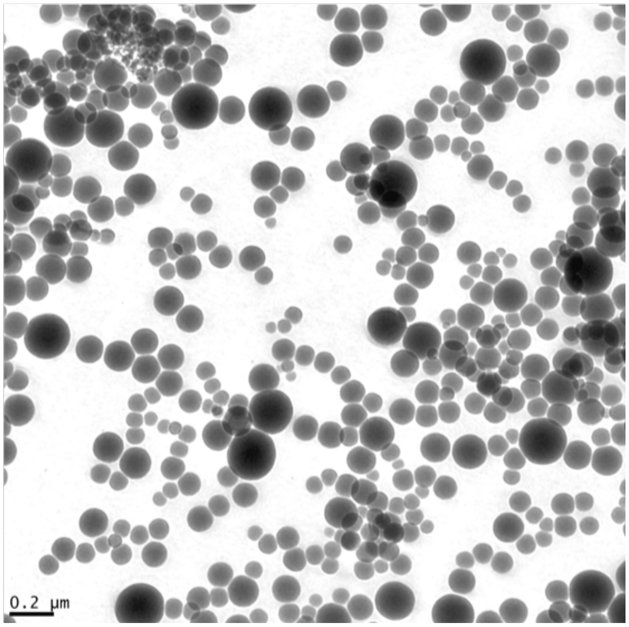

Figure B.52: *TEM Micrograph of Dex-SiO$_2$-NPs Prepared using β-cyclodextrin and Dex-SiO$_2$-250 Conditions*. 27kx magnification, Scale bar 0.2 μm. Brightness enhanced by 20% to emphasize detail.

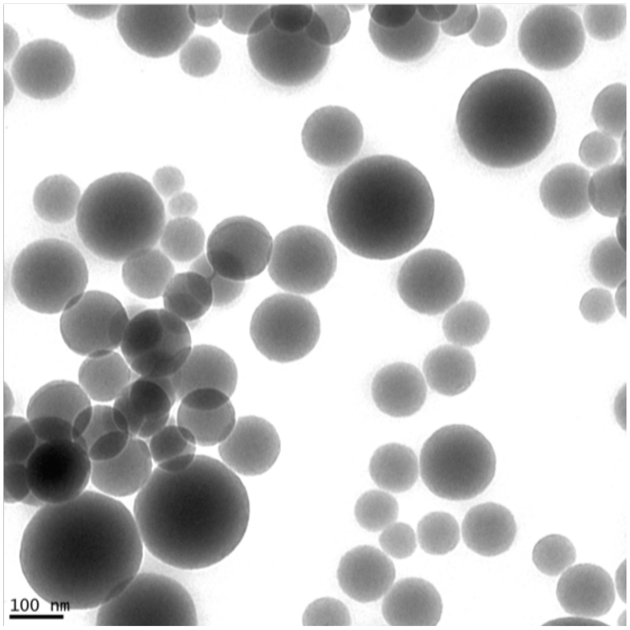

Figure B.53: *TEM Micrograph of Dex-SiO$_2$-NPs Prepared using β-cyclodextrin and Dex-SiO$_2$-250 Conditions*. 67kx magnification, Scale bar 100 nm. Brightness enhanced by 20% to emphasize detail.

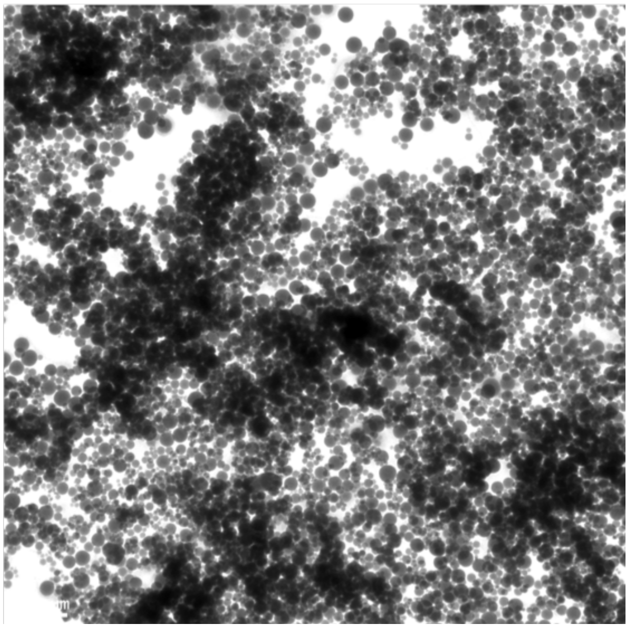

Figure B.54: *TEM Micrograph of Dex-SiO$_2$-NPs Prepared using β-cyclodextrin and Dex-SiO$_2$-350 Conditions*. 14kx magnification, Scale bar 0.5 μm. Brightness enhanced by 20% to emphasize detail.

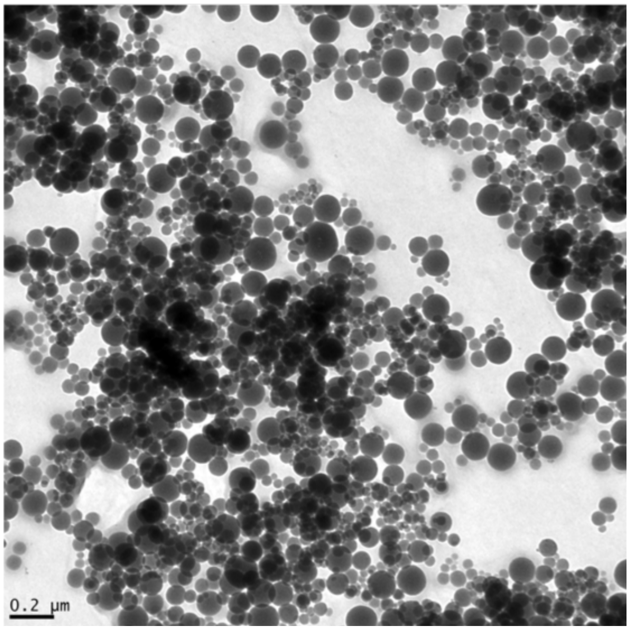

Figure B.55: *TEM Micrograph of Dex-SiO$_2$-NPs Prepared using β-cyclodextrin and Dex-SiO$_2$-350 Conditions*. 27kx magnification, Scale bar 0.2 μm. Brightness enhanced by 20% to emphasize detail.

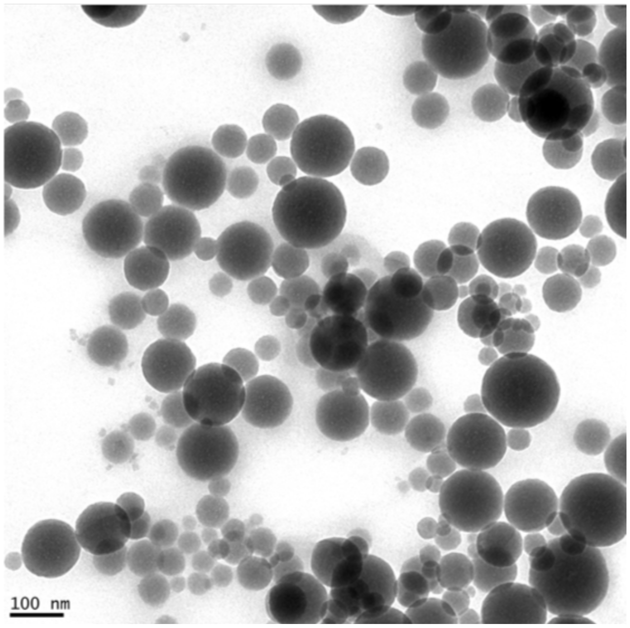

Figure B.56: *TEM Micrograph of Dex-SiO$_2$-NPs Prepared using β-cyclodextrin and Dex-SiO$_2$-350 Conditions*. 67kx magnification, Scale bar 100 nm. Brightness enhanced by 20% to emphasize detail.

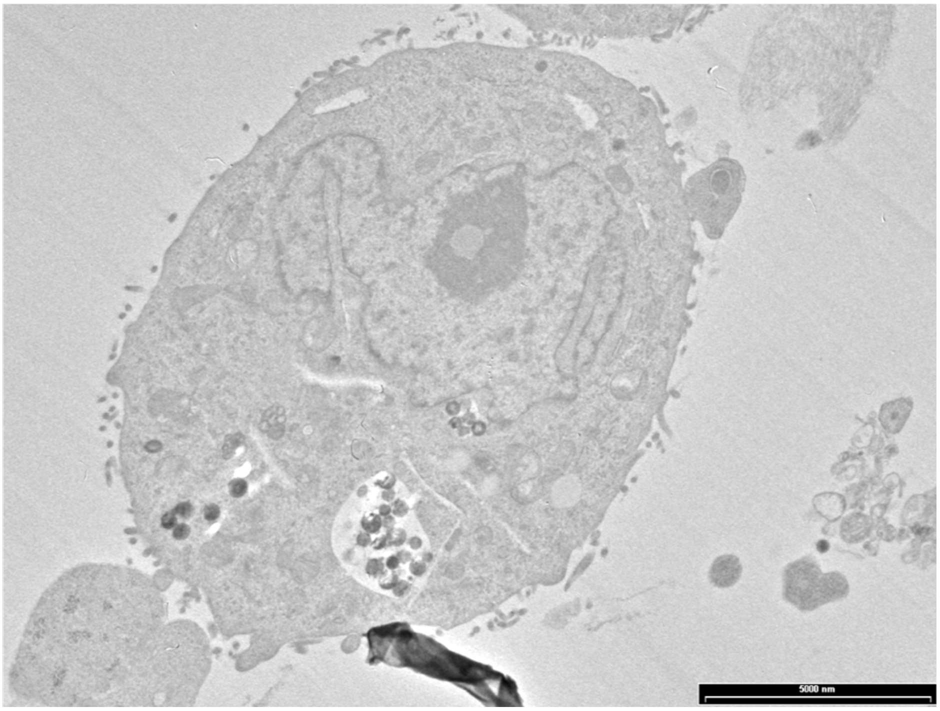

Figure B.57: *TEM Micrograph of 40% Amine Dex-SiO$_2$-350 in HELA Cells*. HELA cells suspended in resin 24 hours post-transfection with siRNA-loaded Dex-SiO$_2$-NPs. Brightness enhanced by 20% to emphasize detail, scale bar 5000 nm.

APPENDIX C

SUPPLEMENTAL FIGURES

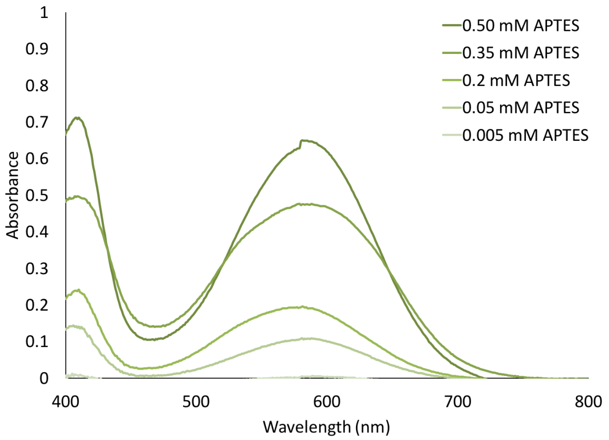

Figure C.1: *UV-Visible Spectrum of Rheumann's Purple at Variable Concentrations.* APTES reacted with ninhydrin reagent, ethanol used as blank

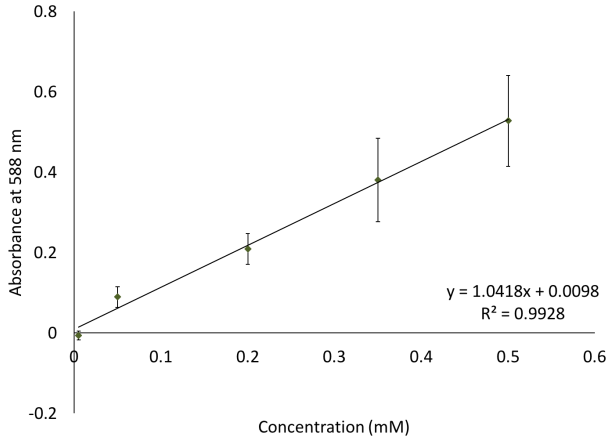

Figure C.2: *Calibration Curve of Rheumann's Purple*. Generated from the absorbance at 588 nm in the UV-Visible spectrum of APTES reacted with ninhydrin reagent, ethanol used as blank. Error bars represent the standard deviation over 5 independent measurements.

Table C.1: *Zeta Potentials of Dex-SiO_2-NPs.*

Carboyhdrate	Synthesis Conditions	Zeta Potential in H_2O (mV)
6 kDa Dextran	Dex-SiO_2-350	11.2
6 kDa Dextran	Dex-SiO_2-250	11.7
6 kDa Dextran	Dex-SiO_2-200	7.0
9-11 kDa Dextran	Dex-SiO_2-350	30.2
9-11 kDa Dextran	Dex-SiO_2-250	4.5
9-11 kDa Dextran	Dex-SiO_2-200	4.2
40 kDa Dextran	Dex-SiO_2-350	14.9
40 kDa Dextran	Dex-SiO_2-250	5.6
40 kDa Dextran	Dex-SiO_2-200	0.3
α-cyclodextrin	Dex-SiO_2-350	19.4
α-cyclodextrin	Dex-SiO_2-250	8.3
α-cyclodextrin	Dex-SiO_2-200	2.3
β-cyclodextrin	Dex-SiO_2-350	8.6
β-cyclodextrin	Dex-SiO_2-250	6.5
β-cyclodextrin	Dex-SiO_2-200	4.7

REFERENCES

REFERENCES

[1] Fire, A.; Xu, S. Q.; Montgomery, M. K.; Kostas, S. A.; Driver, S. E.; Mello, C. C. *Nature*, **1998**, *391*, 806–811.

[2] Elbashir, S. M.; Harborth, J.; Lendeckel, W.; Yalcin, A.; Weber, K.; Tuschl, T. *Nature*, May 2001, *411*(6836), 494–498.

[3] Cavallaro, G.; Sardo, C.; Craparo, E. F.; Porsio, B.; Giammona, G. *Int. J. Pharm.*, June 2017, *525*(2), 313–333.

[4] Adesina, S. K.; Akala, E. O. *Mol. Pharm.*, December 2015, *12*(12), 4175–4187.

[5] Wittrup, A.; Lieberman, J. *Nat. Rev. Genet.*, August 2015, *16*(9), 543–552.

[6] Bobbin, M. L.; Rossi, J. J. *Annu. Rev. Pharmacol. Toxicol.*, **2016**, *56*(1), 103–122.

[7] Angart, P.; Vocelle, D.; Chan, C.; Walton, S. *Pharmaceuticals*, March 2013, *6*(4), 440–468.

[8] Cooper, B. M.; Putnam, D. *ACS Biomaterials Science & Engineering*, **2016**, *2*(11), 1837–1850.

[9] Office of the Commissioner. Press announcements - FDA approves first-of-its kind targeted RNA-based therapy to treat a rare disease. `https://www.fda.gov/NewsEvents/Newsroom/PressAnnouncements/ucm616518.htm`. Accessed: 2018-8-15.

[10] Search of: siRNA | recruiting, not yet recruiting, active, not recruiting, enrolling by invitation studies | united states - list results - ClinicalTrials.gov. `https://www.clinicaltrials.gov/ct2/results?term=siRNA&cntry=US&Search=Apply&recrs=b&recrs=a&recrs=f&recrs=d&age_v=&gndr=&type=&rslt=`. Accessed: 2019-1-20.

[11] Comiskey, G. *SYNTHESIS AND CHARACTERIZATION OF POLYMERIC AND INORGANIC MATERIALS FOR BIOMEDICAL APPLICATIONS*. PhD thesis, Michigan State University, East Lansing, MI, 2013.

[12] Vocelle, D.; Chesniak, O. M.; Malefyt, A. P.; Comiskey, G.; Adu-Berchie, K.; Smith, M. R.; Chan, C.; Walton, S. P. *Technology*, **2016**, *04*(01), 42–54.

[13] ALOthman, Z. *Materials*, December 2012, *5*(12), 2874–2902.

[14] Gorrepati, E. A.; Wongthahan, P.; Raha, S.; Fogler, H. S. *Langmuir*, **2010**, *26*(13), 10467–10474.

[15] Silva, C.; Airoldi, C. *J. Colloid Interface Sci.*, November 1997, *195*(2), 381–387.

[16] Zhang, J. H.; Zhan, P.; Wang, Z. L.; Zhang, W. Y.; Ming, N. B. *J. Mater. Res.*, **2003**, *18*(3), 649–653.

[17] Kolbe, G. *Friedrich-Schiller-Universitat Jena*, **1956**.

[18] Stöber, W.; Fink, A.; Bohn, E. *J. Colloid Interface Sci.*, **1968**, *69*, 62–69.

[19] Van Blaaderen, A.; Van Geest, J.; Vrij, A. *J. Colloid Interface Sci.*, **1992**, *154*(2).

[20] Han, Y.; Lu, Z.; Teng, Z.; Liang, J.; Guo, Z.; Wang, D.; Han, M.-Y.; Yang, W. *Langmuir*, June 2017, *33*(23), 5879–5890.

[21] Brinker, C. J.; Scherer, G. W. in *Sol-Gel Science*, Brinker, C. J.; Scherer, G. W., Eds., pp 96–233. Academic Press, San Diego, 1990.

[22] Bogush, G. H.; Tracy, M. A.; Iv, C. F. Z. *J. Non-Cryst. Solids*, **1988**, *104*, 95–106.

[23] Hartlen, K. D.; Athanasopoulos, A. P. T.; Kitaev, V. *Langmuir*, March 2008, *24*(5), 1714–1720.

[24] LaMer, V. K.; Dinegar, R. H. *J. Am. Chem. Soc.*, November 1950, *72*(11), 4847–4854.

[25] Lee, K.; Sathyagal, A. N.; McCormick, A. V. *Colloids and Surfaces A: Physicochemical and Engineering Aspects*, **1998**, *144*, 115–125.

[26] Bogush, G. H.; Zukoski, C. F. *J. Colloid Interface Sci.*, **1991**, *142*(1).

[27] Owens, G. J.; Singh, R. K.; Foroutan, F.; Alqaysi, M.; others. *Prog. Mater Sci.*, **2016**.

[28] Cha, W.; Fan, R.; Miao, Y.; Zhou, Y.; Qin, C.; Shan, X.; Wan, X.; Li, J. *Molecules*, May 2017, *22*(5).

[29] Vallet-Regí, M.; Colilla, M.; Izquierdo-Barba, I.; Manzano, M. *Molecules*, December 2017, *23*(1).

[30] Liberman, A.; Mendez, N.; Trogler, W. C.; Kummel, A. C. *Surf. Sci. Rep.*, September 2014, *69*(2-3), 132–158.

[31] Cheng, K.; Blumen, S. R.; MacPherson, M. B.; Steinbacher, J. L.; Mossman, B. T.; Landry, C. C. *ACS Appl. Mater. Interfaces*, **2010**, *2*(9), 2489–2495.

[32] Steinbacher, J. L.; Landry, C. C. *Langmuir*, April 2014, *30*(15), 4396–4405.

[33] Nampi, P. P.; Mohan, V. S.; Sinha, A. K.; Varma, H. *Mater. Res. Bull.*, **2012**, *47*(6), 1379–1384.

[34] Li, L.; Liu, T.; Fu, C.; Meng, X.; Liu, H. *J. Nanosci. Nanotechnol.*, **2016**, *16*, 6766–6772.

[35] Bobo, D.; Robinson, K. J.; Islam, J.; Thurecht, K. J.; Corrie, S. R. *Pharm. Res.*, **2016**.

[36] Li, J.-L.; Cheng, Y.-J.; Zhang, C.; Cheng, H.; Feng, J.; Zhuo, R.-X.; Zeng, X.; Zhang, X.-Z. *ACS Appl. Mater. Interfaces*, February 2018, *10*(6), 5287–5295.

[37] Solberg, S. M.; Landry, C. C. *J. Phys. Chem. B*, August 2006, *110*(31), 15261–15268.

[38] Naessens, M.; Cerdobbel, A.; Soetaert, W.; Vandamme, E. J. *J. Chem. Technol. Biotechnol.*, August 2005, *80*(8), 845–860.

[39] Dextran and related polysaccharides. https://www.sigmaaldrich.com/technical-documents/articles/biofiles/dextran-and-related.html. Accessed: 2019-1-23.

[40] Mehvar, R. *J. Control. Release*, **2000**, *69*(1), 1–25.

[41] Larsen, C. *Adv. Drug Deliv. Rev.*, **1989**, *3*(1), 103–154.

[42] Gil, E. C.; Colarte, A. I.; El Ghzaoui, A.; Durand, D.; Delarbre, J. L.; Bataille, B. *Eur. J. Pharm. Biopharm.*, **2008**, *68*(2), 319–329.

[43] Posocco, B.; Dreussi, E.; De Santa, J.; Toffoli, G.; Abrami, M.; Musiani, F.; Grassi, M.; Farra, R.; Tonon, F.; Grassi, G.; Dapas, B. *Materials*, May 2015, *8*(5), 2569–2615.

[44] Chen, X.; Yao, X.; Chen, L. *Polym. Int.*, **2015**, *64*(3), 430–436.

[45] Zafar, R.; Zia, K. M.; Tabasum, S.; Jabeen, F.; Noreen, A.; Zuber, M. *Int. J. Biol. Macromol.*, **2016**, *92*, 1012–1024.

[46] Davis, M. E.; Brewster, M. E. *Nat. Rev. Drug Discov.*, December 2004, *3*(12), 1023–1035.

[47] Zhang, J.; Ma, P. X. *Adv. Drug Deliv. Rev.*, **2013**, *65*(9), 1215–1233.

[48] O'Mahony, A. M.; O'Driscoll, C. M.; Caitriona, M.; O'Neill, M. J.; Godinho, B.; Darcy, R.; Cryan, J. F. *Pharmaceutical Nanotechnology*, **2013**, *1*(1), 6–14.

[49] Lacatusu, I.; Badea, N.; Bojin, D.; Iosub, I.; Meghea, A. *Mol. Cryst. Liq. Cryst.*, **2010**, *521*(October), 272–278.

[50] Numata, M.; Li, C.; Bae, A.-H.; Kaneko, K.; Sakurai, K.; Shinkai, S. *Chem. Commun.*, **2005**, (37), 4655–4657.

[51] Coradin, T.; Lopez, P. J. *Chembiochem*, **2003**, *4*(4), 251–259.

[52] Hao, N.; Chen, X.; Jeon, S.; Yan, M. *Adv. Healthc. Mater.*, **2015**, *4*(18), 2797–2801.

[53] Xie, M.; Lei, H.; Zhang, Y.; Xu, Y.; Shen, S.; Ge, Y.; Li, H.; Xie, J. *RSC Adv.*, **2016**, *6*, 9328–9337.

[54] Lin, Z.; Li, J.; He, H.; Kuang, H.; Chen, X.; Xie, Z.; Jing, X.; Huang, Y. *RSC Adv.*, **2015**, *5*(13), 9546–9555.

[55] Sinha, A.; Chakraborty, A.; Jana, N. R. *ACS Appl. Mater. Interfaces*, **2014**, *6*(24), 22183–22191.

[56] Guo, M.; Jiang, M.; Pispas, S.; Yu, W.; Zhou, C. *Macromolecules*, **2008**, *41*(24), 9744–9749.

[57] Zafar, N.; Fessi, H.; Elaissari, A. *Int. J. Pharm.*, **2014**, *472*(1-2), 118–129.

[58] Mansfield, E. D. H.; Pandya, Y.; Mun, E. A.; Rogers, S. E.; Abutbul-Ionita, I.; Danino, D.; Williams, A. C.; Khutoryanskiy, V. V. *RSC Adv.*, **2018**, *8*(12), 6471–6478.

[59] Salis, A.; Fanti, M.; Medda, L.; Nairi, V.; Cugia, F.; Piludu, M.; Sogos, V.; Monduzzi, M. *ACS Biomater. Sci. Eng.*, May 2016, *2*(5), 741–751.

[60] Silvestri, B.; Pezzella, A.; Luciani, G.; Costantini, A.; Tescione, F.; Branda, F. *Materials Science and Engineering C*, **2012**, *32*(7), 2037–2041.

[61] Krasucka, P.; Stefaniak, W.; Kierys, A.; Goworek, J. *Microporous Mesoporous Mater.*, **2016**, *221*, 14–22.

[62] Krasucka, P.; Goworek, J.; Kierys, A. *Adsorption*, **2016**, *22*(4-6), 663–671.

[63] Wang, X.; Zhang, Y.; Luo, W.; Elzatahry, A. A.; Cheng, X.; Alghamdi, A.; Abdullah, A. M.; Deng, Y.; Zhao, D. *Chem. Mater.*, **2016**, *28*(7), 2356–2362.

[64] Gao, Z.; Zharov, I. *Chem. Mater.*, March 2014, *26*(6), 2030–2037.

[65] Xing, Z.; Tay, S.-W.; Ng, Y. H.; Hong, L. *ACS Appl. Mater. Interfaces*, May 2017, *9*(17), 15103–15113.

[66] Wang, Y.; Wang, J.; Yang, Y.; Sun, Y.; Yuan, Y.; Li, Y.; Liu, C. *Colloids Surf. B Biointerfaces*, May 2017, *153*, 272–279.

[67] van Bommel, K. J. C.; Friggeri, A.; Shinkai, S. *Angew. Chem. Int. Ed Engl.*, March 2003, *42*(9), 980–999.

[68] van Bommel, K.; Jung, J. H.; Shinkai, S. *Adv. Mater.*, **2001**, *13*(19), 1472–1476.

[69] Ruckdeschel, P.; Dulle, M.; Honold, T.; Förster, S.; Karg, M.; Retsch, M. *Nano Res.*, **2016**, *9*(5), 1366–1376.

[70] Liberman, A.; Martinez, H. P.; Ta, C. N.; Barback, C. V.; Mattrey, R. F.; Kono, Y.; Blair, S. L.; Trogler, W. C.; Kummel, A. C.; Wu, Z. *Biomaterials*, July 2012, *33*(20), 5124–5129.

[71] Zhou, H.; Luo, J.; Gao, Q.; Yang, T. *J. Appl. Polym. Sci.*, **2016**, *44200*, 1–8.

[72] Hu, J.; Chen, M.; Fang, X.; Wu, L. *Chem. Soc. Rev.*, **2011**, *40*(40), 5472–5491.

[73] Park, S.-J.; Kim, Y.-J.; Park, S.-J. *Langmuir*, November 2008, *24*(21), 12134–12137.

[74] Faulkner, R.; DiVerdi, J.; Yang, Y.; Kobayashi, T.; Maciel, G. *Materials*, December 2012, *6*(1), 18–46.

[75] Alia, A.; Ganapathy, S.; de Groot, H. J. M. *Photosynth. Res.*, November 2009, *102*(2-3), 415–425.

[76] Polenova, T.; Gupta, R.; Goldbourt, A. *Anal. Chem.*, June 2015, *87*(11), 5458–5469.

[77] Inkson, B. J. in *Materials Characterization Using Nondestructive Evaluation (NDE) Methods*, Hübschen, G.; Altpeter, I.; Tschuncky, R.; Herrmann, H.-G., Eds., pp 17–43. Woodhead Publishing, January 2016.

[78] Ayache, J.; Beaunier, L.; Boumendil, J.; Ehret, G.; Laub, D. in *Sample Preparation Handbook for Transmission Electron Microscopy: Methodology*, Ayache, J.; Beaunier, L.; Boumendil, J.; Ehret, G.; Laub, D., Eds., pp 33–55. Springer New York, New York, NY, 2010.

[79] Li, S.; Wan, Q.; Qin, Z.; Fu, Y.; Gu, Y. *Langmuir*, September 2016, *32*(36), 9180–9187.

[80] Li, W.; Xu, Y.; Zhou, Y.; Ma, W.; Wang, S.; Dai, Y. *Nanoscale Res. Lett.*, August 2012, *7*(1), 485.

[81] Park, K.; Kittelson, D. B.; Zachariah, M. R.; McMurry, P. H. *J. Nanopart. Res.*, June 2004, *6*(2), 267–272.

[82] Yang, F.; Yang, W.; Zhu, L.; Chen, Y.; Ye, Z. *Prog. Org. Coat.*, **2016**, *95*, 1–7.

[83] Zhong, G.; Guo, W.; Liu, Y.; Wei, Y.; Meng, X.; Hu, Z.; Liu, F. *Colloids Surf. A Physicochem. Eng. Asp.*, **2015**, *485*, 63–72.

[84] Chen, W.; Takai, C.; Khosroshahi, H. R.; Fuji, M.; Shirai, T. *Colloids Surf. A Physicochem. Eng. Asp.*, **2015**, *481*, 375–383.

[85] Malvern Panalytical Ltd. *Zetasizer User Manual*, January 2007.

[86] Hunter, R. J. *Zeta Potential in Colloid Science: Principles and Applications*. Academic Press, September 2013.

[87] Moayedi, H.; Kazemian, S.; Kassim, K. A.; Nazir, R.; Raftari, M. *J. Dispersion Sci. Technol.*, September 2013, *34*(9), 1273–1279.

[88] Stetefeld, J.; McKenna, S. A.; Patel, T. R. *Biophys. Rev.*, December 2016, *8*(4), 409–427.

[89] Branda, F.; Silvestri, B.; Costantini, A.; Luciani, G. *J. Sol-Gel Sci. Technol.*, January 2015, *73*(1), 54–61.

[90] Sing, K. S. W.; Williams, R. T. *Adsorpt. Sci. Technol.*, December 2004, *22*(10), 773–782.

[91] Matthias Thommes, Katsumi Kaneko, Alexander V. Neimark, James P. Olivier, Francisco Rodriguez-Reinoso, Jean Rouquerol and Kenneth S. W. Sing. *Pure and Applied Chemistry*, **2015**, *87*(9-10), 1051–1069.

[92] Kruk, M.; Jaroniec, M. *Chem. Mater.*, October 2001, *13*(10), 3169–3183.

[93] Gregg, S. J.; Sing, K. S. W. *Adsorption, surface area, and porosity*. Academic Press, 1991.

[94] Sing, K. S. W.; Williams, R. T. *Adsorpt. Sci. Technol.*, **2005**, *23*(10), 839–853.

[95] Sing, K. *Colloids Surf. A Physicochem. Eng. Asp.*, **2001**, *187-188*, 3–9.

[96] Olivier, J. P. *J. Porous Mater.*, July 1995, *2*(1), 9–17.

[97] Lastoskie, C. M.; Gubbins, K. E. *Stud. Surf. Sci. Catal.*, **2000**, *128*, 41–50.

[98] Li, S.; Wan, Q.; Qin, Z.; Fu, Y.; Gu, Y. *Langmuir*, January 2015, *31*(2), 824–832.

[99] Li, S.; Wan, Q.; Qin, Z.; Fu, Y.; Gu, Y. *J. Therm. Anal. Calorim.*, November 2018.

[100] Li, Z.-J.; Liu, C.-R.; Zhao, Q.-S. *J. Non-Cryst. Solids*, March 2000, *265*(1), 189–192.

[101] Kuang, Y.; Song, S.; Huang, J.; Sun, X. *J. Solid State Chem.*, **2015**, *224*, 120–126.

[102] Xiong, B.; Cheng, J.; Qiao, Y.; Zhou, R.; He, Y.; Yeung, E. S. *J. Chromatogr. A*, June 2011, *1218*(25), 3823–3829.

[103] Microfiltration membranes | chromatography sample prep - life science research | EMD millipore. `http://www.emdmillipore.com/US/en/life-science-research/chromatography-sample-preparation/microfiltration-membranes/FqCb.qB.7ZkAAAFBDQZlvzJE,nav`. Accessed: 2018-12-31.

[104] Chen, S.-L.; Dong, P.; Yang, G.-H.; Yang, J.-J. *Ind. Eng. Chem. Res.*, January 1996, *35*(12), 4487–4493.

[105] Van Blaaderen, A.; Vrij, A. *J. Colloid Interface Sci.*, **1993**, *156*, 1–18.

[106] Su, W.-F. in *Principles of Polymer Design and Synthesis*, Su, W.-F., Ed., pp 9–26. Springer Berlin Heidelberg, Berlin, Heidelberg, 2013.

[107] Antoniou, E.; Tsianou, M. *J. Appl. Polym. Sci.*, August 2012, *125*(3), 1681–1692.

[108] de Belder, a. N. *Amersham Bioscience*, **2003**, p 60.

[109] Granath, K. A. *J. Colloid Sci.*, **1958**, *13*(4), 308–328.

[110] Kasaai, M. R. *Carbohydr. Polym.*, **2012**, *88*(1), 373–381.

[111] Erickson, H. P. *Biol. Proced. Online*, **2009**, *11*(1), 32–51.

[112] Bao, Y.; Shi, C.; Wang, T.; Li, X.; Ma, J. *Microporous Mesoporous Mater.*, June 2016, *227*, 121–136.

[113] Guo, Y.; Andrew Davidson, R.; Peck, K. A.; Guo, T. *J. Colloid Interface Sci.*, May 2015, *445*, 112–118.

[114] Hu, J.; Chen, M.; Fang, X.; Wu, L. *Chem. Soc. Rev.*, **2011**, *40*(40), 5472–5491.

[115] Li, Z.-J.; Liu, C.-R.; Zhao, Q.-S. *J. Non-Cryst. Solids*, March 2000, *265*(1), 189–192.

[116] Soto-Cantu, E.; Cueto, R.; Koch, J.; Russo, P. S. *Langmuir*, April 2012, *28*(13), 5562–5569.

[117] Szegedi, A.; Popova, M.; Goshev, I.; Klébert, S.; Mihály, J. *J. Solid State Chem.*, **2012**, *194*, 257–263.

[118] Shlyakhtenko, L. S.; Gall, A. A.; Lyubchenko, Y. L. in *Cell Imaging Techniques: Methods and Protocols*, Taatjes, D. J.; Roth, J., Eds., Methods in Molecular Biology, pp 295–312. Humana Press, Totowa, NJ, 2 edition, 2013.

[119] Nagao, D.; Satoh, T.; Konno, M. *J. Colloid Interface Sci.*, December 2000, *232*(1), 102–110.